Spin-motion dynamics with ultracold polar molecules

by

Calder Miller

A.B., Harvard University, 2020

S.M., Harvard University, 2020

A thesis submitted to the

Faculty of the Graduate School of the

University of Colorado in partial fulfillment

of the requirements for the degree of

Doctor of Philosophy

Department of Physics

2025

Committee Members:

Jun Ye, Chair

Ana Maria Rey

John L. Bohn

Adam M. Kaufman

Joel D. Eaves

Miller, Calder (Ph.D., Physics)

Spin-motion dynamics with ultracold polar molecules

Thesis directed by Prof. Jun Ye

Optically trapped ultracold polar molecules offer a rapidly maturing platform for quantum science. Due to their strong, long-range, and tunable dipolar interactions, these systems are particularly suitable for realizing spin-motion models with rich many-body physics. However, the additional complexity of molecules compared with single atoms makes production of ultracold gases and control of interactions challenging.

In this thesis, I discuss our efforts to improve production and control of ultracold molecules and to explore the many-body physics arising from their interactions. Using a spin encoded in rotational states of fermionic $^{40}K^{87}Rb$ molecules, we demonstrated tuning of Heisenberg XXZ models with electric fields and Floquet engineering of XYZ models with microwave pulse sequences. By additionally regulating motion with optical lattices, we realized highly tunable generalized t-J models, relevant to quantum simulation of strongly correlated materials. We used Ramsey spectroscopy to explore the out-of-equilibrium dynamics of these systems, observing one- and two-axis twisting at short times, and dephasing due to dipolar interactions and their coupling to motion at longer times. These methods could be used to generate spin-squeezed states relevant to precision metrology.

In addition to controlling interactions, observing new dynamics and phases predicted for these models requires preparing low-entropy initial states in bulk or lattice systems. I present progress towards producing a deeply degenerate Fermi gas in an isolated 2D layer, enabling control of the anisotropy of the dipolar interactions. Using a tunable-spacing optical lattice, we compressed a K-Rb mixture into a quasi-2D geometry, producing 2D molecular gases below the Fermi temperature. I discuss prospects for improving molecule production and evaporative cooling into deep degeneracy.

Acknowledgements

Thank you, Jun, for your patience, scientific vision, technical expertise, and positive attitude. It has been inspiring to see how you operate a thriving lab, and I hope to apply what I learned to my life and career.

The results presented in this thesis were a team effort by the whole JILA KRb group, Luigi De Marco, Giacomo Valtolina, Jun-Ru Li, Kyle Matsuda, Will Tobias, Annie Carroll, Jake Higgins, Henrik Hirzler, Junyu Lin, Krzysztof Zamarski, Phil Martin, and Tim de Jongh. The greater Ye lab has been an exciting place to work, in the company of interesting people shining interesting lasers on all sorts of interesting things.

We had the opportunity to collaborate with a number of theorists, including Thomas Bilitewski, Sean Muleady, David Wellnitz, Ana Maria Rey, Reuben Wang, John Bohn, Haoyang Gao, Hengyun Zhao, Mikhail Lukin, and Norm Yao. I am grateful for their patience during long technical meetings and their essential physics insights.

The excellent administrative and technical staff make JILA a productive and enjoyable place to work. In particular, Krista Beck, George Kavadas, Terry Brown, James Fung-A-Fat, Ivan Rýger, Felix Vietmeyer, Adam Ellzey, Hans Green, Calvin Schwadron, James Uhrich, Kyle Thatcher, J. R. Raith, and Agnieszka Lynch made important contributions to the KRb lab's work.

Thank you to my friends from Boulder, including Seth "Boss" Chew, Jack Doyle, Max Frankel, Yu Hyun Lee, Prof.(!) Lee Liu, Chitose "お頭" Maruko, Kameron Mehling, Maya Miklos, Will Milner, Tian Ooi, Emil Pellett, Aruku Senoo, Eric "老板" Song, Suxuen Yew, and Aaron Young, and elsewhere, including Sabrina Chern, Jacquelyn Ho, Eunice Lee, Malia Moore, Simon

Shen, Garrett Tanzer, Kai Trepka, Cathy Wang, and Alex Wei. It's been fun doing common Colorado activities, such as biking/climbing/hiking/running/skiing, and uncommon ones, like eating good food, with you all.

Finally, I want to thank my family, especially my parents Brad and Lindsay and my brother Nico, for their continued company and support.

Contents

Chapter

Figures

Figure

Chapter 1

Introduction

"[Magnets], how do they work?"

Miracles – Insane Clown Posse

Advances in quantum science depend on improved control of increasingly complex systems. Over the last century, scientists have learned to probe and manipulate internal degrees of freedom of atoms and molecules using electromagnetic radiation [1, 2]. This understanding led to the development of the laser [3], which enabled the cooling and trapping of neutral atoms at ultracold temperatures [4]. These trapped atoms provided suitable starting conditions for evaporative cooling [5], leading to the creation of quantum degenerate gases of bosonic [6, 7] and fermionic [8] atoms. Tools for local control have also been developed, allowing preparation and detection of single atoms in optical lattices [9, 10], tweezers [11] and cavities [12]. Currently, atomic, molecular, and optical (AMO) physicists are working towards scaling to larger systems [13] and lower entropies [14] and quantum control of more complex particles, including even polyatomic molecules [15].

Two major themes in quantum science that are enabled by enhanced control are application of AMO platforms to the study of the many-body physics of interacting quantum systems, and to precision spectroscopy with applications to metrology or fundamental physics. The many-body physics direction is motivated by the rich phenomena of solid-state systems, like magnetism [16], high-temperature superconductivity [17], and quantum Hall physics [18]. Direct observation and manipulation of electrons in solids is difficult, and precise measurements can be hindered by defects in materials, often limiting microscopic understanding of phenomena. A complementary approach

to studying condensed matter phenomena, known as quantum simulation [19, 20], is engineering quantum systems that have the same essential physics as a material of interest, but are assembled from constituent particles that are easier to control and detect. Atoms in optical lattices or tweezers, representing the electrons in a material, are a powerful platform for quantum simulation. Ultracold atoms can strongly interact at micron distances, so standard optical microscopy techniques can resolve single particles. This is impossible at the angstrom scales of lattices in a solid. A variety of representative Hamiltonian terms, including hopping between sites and short and long-range interactions, can be generated [21] and tuned into regimes where materials exhibit interesting phases. Notably, the system parameters are widely tunable by changing the applied potentials or electromagnetic control fields, as opposed to condensed matter systems, where different samples or materials are required to access different regimes. Using feedback control [11] or evaporative cooling [5], thermal states, including low-temperature phases [22], or interesting out-of-equilibrium initial states can be prepared. In addition to condensed matter systems, quantum simulation can also be applied to study of phenomena from high energy physics [23, 24]. I briefly introduce the most relevant models for quantum simulation in Sec. 1.2.

Another exciting direction within AMO physics is metrology and precision measurement. Because their spectra and response to perturbations are well-understood to a high degree of precision, cold atoms and molecules can be used as sensors for a variety of phenomena. The possibility to prepare large numbers of identical particles gives these sensors excellent statistical uncertainty and helps with rejection of systematic errors. Atomic spectroscopy underpins the definition of the second and the development of the most accurate clocks [25], along with sensors for motion [26] and electromagnetic fields [27, 28]. In addition, spectra depend, sometimes sensitively, on fundamental constants and symmetries [29]. Spectroscopy can therefore measure these quantities, and test or constrain fundamental theories or potentially enable discovery of new particles.

1.1 Quantum science with ultracold molecules

Optically-trapped polar molecules may enhance the capabilities of the next generation of quantum simulators [30, 31]. In addition to the features of ultracold atoms, molecules possess rich internal structure, allowing selection of states with desired properties or for multiple levels to be used for realizing more complex models. Their electric dipole moments both provide a handle for control with external fields and lead to long-range dipolar interactions between molecules. As in other platforms used for quantum simulation such as Rydberg atoms [11, 32], these dipolar interactions allow the study of quantum magnetism in spin systems. Unique to molecules, the dipole-dipole interactions are between long-lived states and can reach energy scales comparable to the molecules' kinetic energy. This allows realization of a rich space of models incorporating both spin and motion, which are important for simulating materials like high-temperature superconductors [17].

Molecular level structure is also beneficial for precision measurement [33]. Notably, because of strong internal electric fields, molecules are orders of magnitude more sensitive to charge-parity violating effects like an electron electric dipole moment (eEDM) than atoms. Experiments using neutral molecules [34] and molecular ions [35] have set constraints on the eEDM, with prospects for improvement using trapped molecules [36]. In addition, certain dark matter models predict time variation of fundamental constants, which could result in detectable variations of molecular energy levels. Entanglement between molecules could enhance the sensitivity of precision measurements [33].

The additional complexity of molecules as compared to atoms imposes challenges for both areas of application [30]. Both rely on initialization of molecules in a well-defined internal state out of the dozens that are often present even in the ground electronic and vibrational manifolds, and high-fidelity detection of the molecules, which are generally difficult to directly image. Exquisite control of the molecules' position and motion is additionally required for many-body physics applications, which often require a deeply degenerate bulk gas or ordered states in optical lattices or tweezers. Preparing large, ultracold samples and preventing collisional loss due to chemical

reactions is essential for these applications.

In the past two decades, the ultracold molecule community has overcome many of these challenges and made extensive progress towards production and control of ultracold molecules. Two leading approaches to molecule production are direct laser cooling and assembly from ultracold atoms. Direct laser cooling [37, 30] has produced magneto-optical traps (MOTs) of molecules with alkali-like (SrF [38], CaF [39], CaOH [40], ...) or alkaline-earth-like (YO [41], AlF [42]) electronic structure from cold molecular beams [43]. This approach requires species with diagonal Franck-Condon factors[1] to suppress decay into excited vibrational states and design of laser-cooling schemes to ensure rotational closure [44]. Sub-Doppler cooling enabling loading of optical tweezer arrays [45, 11] and production of gases at relatively high phase-space densities (PSDs) [46]. Optical pumping [36, 47] can prepare samples in a single quantum state and the same cycling transitions used for laser cooling allow fluorescence imaging.

An alternative approach is assembly of molecules from ultracold atoms. Well-established methods enable preparation of deeply degenerate atomic gases [48, 49]. These can be associated into vibrationally excited molecules using a Feshbach resonance [50], then optically transferred to the rovibrational ground state. So far, most homonuclear (Li_2 [51], K_2 [52], ...) and bosonic and fermionic heteronuclear (KRb [53], NaK [54], RbCs [55], NaRb [56], NaLi [57], NaCs [58], KCs [59], ...) bialkali and a few alkali-alkaline-earth (RbSr [60]) or alkali-transition metal (LiCr [61]) species have been created. The coherent nature of the process ensures that the resulting molecules are in a single internal state. Because their association is relatively efficient, the molecules inherit a high PSD from their precursor atoms. This is the primary advantage of associated molecules – the resulting PSDs of approximately 1 are orders of magnitude higher than the highest yet attained with direct laser cooling. For detection, the molecules, which do not typically have closed cycling transitions, can be dissociated and the atoms imaged.

[1] The Franck-Condon factor between two vibrational levels is the degree of overlap between the electronic wavefunctions in the two levels. The rate of decay from an excited electronic state into different vibrational ground states is proportional to each state's Franck-Condon factor.

1.2 Quantum simulation of spin-motion models

The rich physics of materials emerges from the motion of electrons through a potential landscape defined by ion cores and other electrons [16]. Some key ingredients for quantum simulation of condensed matter systems are apparent from this brief description: a general quantum simulator should include spinful particles with fermionic statistics and tunable interactions, mobile within a controllable potential landscape[2] .

Atoms in optical lattices naturally satisfy many of these desiderata. One can choose atoms with fermionic or bosonic statistics, and hyperfine levels of the atoms can encode a spin. The potential can be designed to represent different crystalline [62, 63] or quasicrystalline [64] lattices or disordered potentials [65][3] . The degree of itinerance is tunable by varying the lattice depth (Sec. 3.3.1) and the strength of short-range interactions can be tuned using Feshbach resonances [50]. A minimal but extremely rich model capturing these elements is the Fermi-Hubbard model [16]

$$H_{\text{Fermi-Hubbard}} = -t \sum_{\langle ij \rangle, \sigma} \left(\hat{c}^\dagger_{i\sigma} \hat{c}_{j\sigma} + \hat{c}_{i\sigma} \hat{c}^\dagger_{j\sigma} \right) + U \sum_i \hat{n}_{i\uparrow} \hat{n}_{i\downarrow} \tag{1.1}$$

where $\sigma \in \{\uparrow, \downarrow\}$ indexes the spin states, i and j index lattice sites, with $\langle ij \rangle$ denoting neighboring sites, $\hat{c}^\dagger$ and $\hat{c}$ represent creation and annihilation operators, and $\hat{n} = \hat{c}^\dagger \hat{c}$ is the number operator. In cuprate materials, $U \approx 10t$ [17] and temperatures $T \lessapprox 0.05t$ [14] are believed to be required to reach superconducting phases.

When $U \gg t$, double occupancy is energetically suppressed. In this regime, the combination of motion and onsite interactions results in superexchange, resonant spin-exchange between neighboring sites with rate $J = 4t^2/U$ [22, 67], giving rise to the t-J model [17]

[2] Depending on the particular model being studied, some of these requirements can be relaxed or a model dual to the target Hamiltonian can be realized with different physical requirements.

[3] One notable feature of materials that is challenging to realize in optical lattices is phonons, although recent progress has been made in that direction [66].

$$H_{tJ} = \hat{P}\left(-\sum_{\langle ij\rangle,\sigma} t_{ij}\left(\hat{c}^{\dagger}_{i\sigma}\hat{c}_{j\sigma} + \text{h.c.}\right) + J\sum_{\langle ij\rangle}\left(\hat{\mathbf{s}}_i \cdot \hat{\mathbf{s}}_j - \frac{1}{4}\hat{n}_i\hat{n}_j\right)\right)\hat{P} \tag{1.2}$$

where J is the strength of spin exchange, $\hat{P}$ is a projection operator to the subspace of singly occupied site and $\hat{\mathbf{s}} = \{\hat{s}_x, \hat{s}_y, \hat{s}_z\}$ is the spin operator on each site. At half filling, a Mott insulator [68] is formed, with one atom occupying each lattice site. Because of superexchange, rich physics emerges in the spin sector, described by the Heisenberg model [67]

$$H_{\text{Heisenberg}} = J\sum_{\langle ij\rangle}\left(\hat{\mathbf{s}}_i \cdot \hat{\mathbf{s}}_j\right) \tag{1.3}$$

For $J > 0$, the ground state is an antiferromagnet, which has been realized using ultracold atoms [69, 22]. If additional particles or holes are introduced, itinerance becomes relevant beyond allowing superexchange, and pseudogap [70, 71] and stripe [72, 73] phases can emerge. In this regime, the interplay between spin and motion makes the system challenging to study numerically and is expected to lead to superconducting phases in the Hubbard model and its variants [17].

The long-range interactions of polar molecules (and magnetic atoms [74, 75]) enable extensions of Hubbard models [76] (described in Sec. 5.4.1) that may feature qualitatively different physics or facilitate observation of superconducting physics. Tunneling beyond nearest neighbors, which can be represented by long-range dipolar interactions, may be important for superconducting phases [72]. The dipolar interactions also enable tuning of J across a wide range, including to $J \gtrapprox t$, in contrast to the $J \ll t$ accessible with superexchange, and can realize more general Heisenberg XXZ and XYZ spin Hamiltonians (Ch. 4 and 5), which may lead to relaxed temperature requirements for superfluid phases [76]. The anisotropy of dipolar interactions can be tuned with applied fields, leading to new kinds of spatial order [75]. Because they combine the features of ultracold atoms with richly tunable interactions, ultracold molecules will be an exciting platform for the next generation of quantum simulators for many-body physics.

1.3 Summary

In this thesis, I discuss work conducted with associated fermionic $^{40}K^{87}Rb$ molecules, primarily focusing on the many-body physics direction. After introducing the experimental apparatus and sequence (Ch. 2) and methods we use for controlling the molecules (Ch. 3), I discuss our realization and study of tunable spin and spin-motion models in optical lattices (Ch. 4 and 5). I discuss recent progress towards and methods for preparing low entropy states for quantum simulation (Ch. 6). Finally (Ch. 7), I discuss prospects for applying the demonstrated methods for preparing entangled states for precision metrology.

Chapter 2

The JILA KRb apparatus

"Welcome my son
Welcome to the machine
What did you dream?"

Welcome to the Machine – Pink Floyd

The production of ultracold KRb molecules on the first [77, 78, 79, 80, 81, 82] and second generation [82, 83, 84] JILA KRb machines have been extensively discussed in previous theses. In this chapter, I give a brief overview of the experimental sequence and discuss upgrades and modifications to the apparatus made during my PhD.

2.1 Experimental sequence

Preparation of high phase space density samples of bialkali molecules relies on preparation of large, ultracold atomic mixtures. With association of sufficiently degenerate atoms, degenerate Fermi gases of polar molecules can be directly produced [85, 86, 87]. The majority of the experimental complexity (seven out of the experiment's nine laser systems) and runtime (often all but a few milliseconds of the experiment's 45-second cycle) are dedicated to preparing these atomic mixtures, and improvements in the atom cooling typically translate to improvements in molecule phase space density.

In brief, we laser cool ^{40}K and ^{87}Rb atoms and load them into a magnetic quadrupole trap. Following transport, and evaporative cooling in the magnetic trap and an optical dipole trap, we

obtain a Bose-Einstein condensate (BEC) of Rb and a degenerate Fermi gas (DFG) of K. We then associate the atoms into KRb Feshbach molecules with a magnetic field ramp, and use stimulated Raman adiabatic passage (STIRAP) to transfer the molecules into the rovibrational ground state (shown schematically in Fig. 2.1). The sequence, along with improvements to the atom cooling, is described in more detail in the following sections.

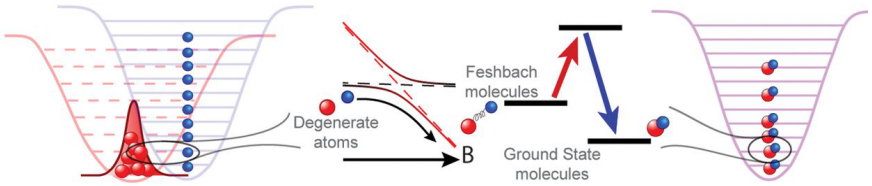

Figure 2.1: Molecule production, beginning with a Rb (red) BEC and a K (blue) DFG, consists of association using a Feshbach resonance and STIRAP to the ground state, here producing a KRb DFG. From [85].

2.1.1 Magneto-optical trapping and laser cooling

We first load overlapped MOTs of K and Rb in a glass vapor cell for approximately 10 s. The cooling and repumping light for each species are generated from distributed Bragg reflector (DBR) lasers from Photodigm, then combined and amplified by a Toptica Eagleyard tapered amplifier (TA), yielding roughly 1 W of total power for each species. Both species are loaded into the MOTs from dispensers, with the potassium dispenser enriched to 14% ^{40}K [1] [88]. The loading of both species is enhanced by light-induced atomic desorption (LIAD) [89] using UV LEDs illuminating the MOT cell. LIAD increases the atom number of both species in the MOT by a factor of roughly three, with the number increase saturating with 500 mW of 400 nm light.

K numbers are ultimately limited by light-assisted collisions with Rb, which make up a large majority of the atoms in the MOT. We suppress the loss by overlapping light near the K D1

[1] We have been unable to purchase more ^{40}K at this level of enrichment in the last few years. It is a good idea to occasionally check whether vendors like Trace Sciences International or the National Isotope Development Center have any stock.

transition with the D2 MOT beams[2] . This light, added in 2024 and sourced from the existing K D1 laser system, likely optically pumps the K to dark states, as demonstrated in [92]. When optimized to a D1 detuning of $\approx -1\Gamma$ and a power of $\approx 3I_{\text{sat}}$, where $\Gamma \approx 2\pi \times 5.96$ MHz and $I_{\text{sat}} = 1.75$ mW/cm are the linewidth and saturation intensity of the K D1 transition respectively [90], the number of K cotrapped with Rb increases by a factor of 2 to 3.

After about ten seconds of loading time, more than 10^9 Rb and around 3×10^7 K atoms are trapped in the MOT. The magnetic field is turned off and K and Rb are further cooled to around $10\,\mu$K using gray molasses (described in detail in [83]).

2.1.2 Transport and evaporative cooling

After gray molasses cooling, the atoms are optically pumped into the low-field-seeking stretched states $|F = 2, m_F = 2\rangle$ for Rb and $|9/2, 9/2\rangle$ for K. The atoms are loaded into a magnetic quadrupole trap generated by the same coils used for the MOT magnetic field. The typical temperature in the quadrupole trap is around $40\,\mu$K.

The coils, which are mounted to a Parker 406XR series motorized linear stage, are translated 40 cm in around 3 s, transporting the atoms through a differential pumping tube to an octagonal glass cell where the rest of the experiment is conducted. After transport, which is roughly 30% efficient, the atoms are heated to around $100\,\mu$K. An optical plug beam[3] to repel atoms from the magnetic field zero and suppress loss via spin flips, is ramped on [93]. We use microwaves near the Rb $|2, 2\rangle \leftrightarrow |1, 1\rangle$ transition to remove Rb near the edges of the cloud, evaporatively cooling the Rb and sympathetically cooling the K. After microwave evaporation, we typically have 3 to $4{\times}10^6$ K and 6 to $10{\times}10^6$ Rb at a temperature of $4\,\mu$K in the magnetic trap[4] .

The atoms are then loaded into a crossed optical dipole trap (xODT) made from two perpendicular horizontal beams generated from a Nufern fiber amplifier at 1064 nm. The xODT beams

[2] The level structure of K and Rb atoms are discussed in [90] and [91] respectively. See Fig. 3.2 in [84] for a schematic of the transitions addressed by our laser systems.

[3] Around 400 mW of 763 nm light focused to a $30\,\mu$m waist, generated using a DBR seeding a TA

[4] For improved efficiency and cycle time, it could be beneficial to replace magnetic evaporation with all-optical cooling and compression. For instance, a version of the gray molasses cooling and box trap compression demonstrated with CaF molecules in [94] may work well for atoms.

are elliptical with waists of approximately 180 and 40 μm in the horizontal and vertical directions, respectively. Nearly all the Rb and around 2/3 of the K are loaded into the xODT[5] . The atoms are further evaporatively cooled by reducing the power of the xODT beams[6] , until a Rb BEC and K DFG are created. Midway through evaporation, the K and Rb are transferred to the lowest energy states $|9/2, -9/2\rangle$ and $|1, 1\rangle$ respectively using adiabatic rapid passage (ARP) at a magnetic field of 30 G. The magnetic field is then ramped to 560 G, above the K-Rb Feshbach resonance[7] . After further evaporation and recompression to a trap frequency of $\omega = 2\pi \times (30, 200, 30)$ Hz for Rb[8] , typically 7×10^4 Rb, roughly 80% condensed, and 4×10^5 K at $T/T_F \lessapprox 0.2$ are trapped at a temperature of around 50 nK.

2.1.3 Molecule production

Molecules can be produced directly in the xODT, or the atoms can first be loaded into different combinations of the optical lattices discussed below. In any trap geometry, Feshbach molecules are produced by ramping the magnetic field down across an interspecies Feshbach resonance at 546.76(5) G [95]. The Feshbach molecules are coherently transferred to the rovibrational ground state by STIRAP (Sec. 2.2.2). The remaining atoms are then removed, using resonant light for the K and an ARP to $|2, 2\rangle$ followed by a pulse of resonant light for Rb[9] .

2.1.4 Molecule detection

Following experiments with the molecules, we transfer them back to the Feshbach state using STIRAP. We typically photodissociate the Feshbach molecules and detect the potassium atoms[10]

[5] The loading efficiency could likely be improved with larger beams or higher power, should more K be needed in the future.

[6] One of the biggest causes of atom and molecule number fluctuations in our experiment is drifts of the alignment of the two xODT beams, which changes the trap depth, thus the number and temperature after evaporative cooling. Either improved monitoring and feedback of the alignment, for instance with cameras in the vicinity of the cell, or switching to a single beam light sheet trap could improve stability.

[7] The magnetic field was previously ramped after evaporative cooling, but we found that the ramp caused less heating if done before final evaporation.

[8] In an optical trap made with 1064 nm light, $\omega_{\mathrm{K}} = 1.39\omega_{\mathrm{Rb}} = 1.27\omega_{\mathrm{KRb}}$ [85]

[9] The Rb ARP is currently only around 50% efficient, so we repeat the ARP and cleaning pulse 4-6 times. Improving the speed or efficiency of the atom cleaning may lead to improved molecule conditions, since collisions with Rb atoms lead to rapid loss of the Feshbach molecules [96] and collisions with K atoms rapidly deplete ground state molecules [97]

via absorption imaging with resonant light (discussed in detail in Sec. 7.1.3.2). We measured the detection efficiency to be 87(4)% by comparing the number of detected atoms with photodissociation against a sequence in which the Feshbach molecules are magnetodissociated before imaging. We believe that the Feshbach molecules that are not detected are optically pumped into more deeply bound molecular states by the imaging light. The apparatus supports absorption imaging from three orthogonal directions, including vertically through an NA=0.53 objective with sub-micron resolution.

The STIRAP is only resonant with the ground rovibrational state, so leaves the molecules in the excited rotational states largely unaffected. At zero electric field, we measure that roughly 90% of the molecules in $|N = 1, m_N = 0\rangle$ survive STIRAP[11] . We take advantage of this for state-resolved imaging of the molecules by first detecting molecules in $|0, 0\rangle$, then applying a microwave π pulse to transfer the molecules in $|N = 1\rangle$ to $|0, 0\rangle$ before dissociating them and detecting them on another frame.

2.1.5 Electric field control

We use six in-vacuum electrodes to generate stable d.c. electric fields up to roughly 15 kV/cm with controllable angle, gradient, and curvature. Microwaves to drive rotational transitions of the molecules are coupled to the electrodes using a bias tee. The construction of the electrodes [82] and control and stabilization of the electric field [83, 84] are described in detail in previous theses. In brief, six electrodes comprising four tungsten rods and two indium tin oxide (ITO)-coated glass plates (Fig. 2.2a) are installed in our cell, surrounding the position of the atoms. A setpoint voltage for each electrode is provided by a precision digital-to-analog converter (DAC), with endpoints set by a stable voltage reference. Control of the DACs using a field-programmable gate array (FPGA) allows ramps of the electrode voltage synchronized with the experimental sequence. Each electrode's voltage is divided by a factor of 2000, and subtracted from the reference voltage using a low-noise

[10] It is also possible to detect the rubidium atoms after RF or magnetodissociation. This may be useful for alternative state-resolved imaging schemes or quantum gas microscopy of the Rb atoms, as discussed in [98]

[11] At 1 kV/cm, the STIRAP severely depletes molecules in $|N = 1\rangle$. There, we perform state resolved imaging by shelving $|N = 1\rangle$ in $|N = 2\rangle$ during the $|0, 0\rangle$ STIRAP.

op-amp. The resulting error signal is sent through a loop filter then a high-voltage amplifier which drives the electrode through a low-pass filter. The control system is shown schematically in Fig. 2.2b. By picking appropriate voltages for each electrode, estimated from a COMSOL simulation of the electrode fields and optimized by spectroscopy of the molecules, the target field and geometry can be realized with high precision.

(a)

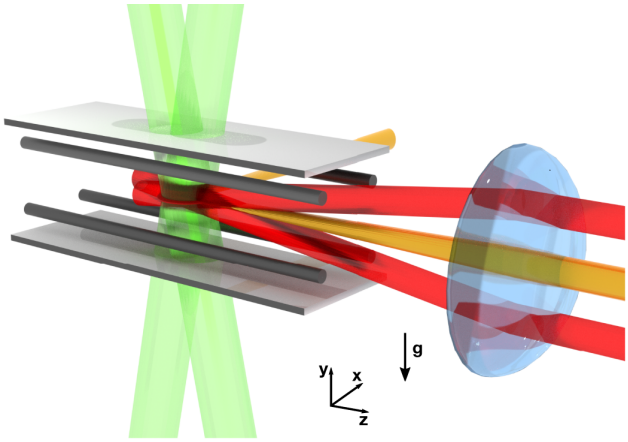

(b)

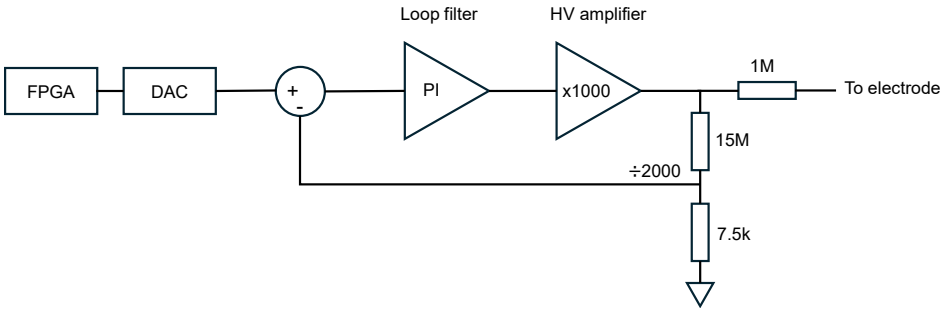

Figure 2.2: **(a)** The configuration of the electrodes is shown schematically, in addition to the paths of the xODT (orange), accordion lattice (red), and vertical lattice (green) beams. From [99]. **(b)** A schematic of the electrode stabilization system. See [83] for more details.

We made minor modifications to the electric field control system after the work described in previous theses [83, 84]. The negative voltage reference for the electrode DACs, generated using

an inverting operational amplifier circuit, was unexpectedly around four times noisier than the positive reference. Replacing the reference PCB with another of the same design removed the excess noise. We also explored reducing high frequency noise by using larger resistors to reduce the corner frequency of the RC low-pass filter following the electrode amplifier. We have typically used 1 M resistors, which combined with the 130 pF capacitance of the electrode cables, allowed the electric field to be changed in hundreds of microseconds [83] for the layer selection experiments (Sec. 3.2.3). Much slower field ramps are acceptable for other projects, allowing the use of a more aggressive filter. This would be important for future projects such as spin squeezing (Ch. 7), which require minimal phase noise between the microwave oscillator and the molecular qubit.

The measured noise voltage spectral density on one of the electrodes is shown in Fig. 2.3, along with estimated improvements if a larger filter resistor is used[12] . Replacing the 1 MΩ filter resistor with a 100 MΩ resistor would reduce the RMS noise voltage by a factor of 10 between 15 and 150 Hz, 16 between 150 Hz and 1.5 kHz, and 28 between 1.5 and 150 kHz.

[12] Somewhat counterintuitively, the total voltage noise due to Johnson noise after an RC filter scales as $1/\sqrt{C}$ and is independent of the resistor value. A larger resistor contributes more noise, which is compensated by the lower corner frequency of the filter [83].

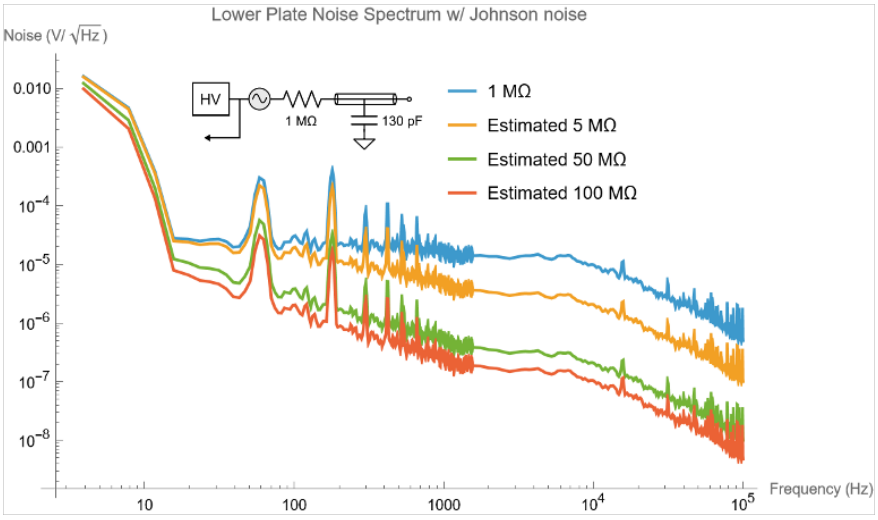

Figure 2.3: The noise spectral density on the lower plate electrode, as measured with an SRS SR760 FFT spectrum analyzer, is shown (blue). The orange, green, and red curves show the estimated PSDs if the 1 MΩ filter resistor was replaced with 5, 50, and 100 MΩ resistors respectively. The schematic of the output filter is taken from [83].

Care is required for accurate measurement of the noise of a system with high output impedance, such as the electrode output filter, as the input impedance of the measuring device can substantially modify the system's transfer function. To resolve this, we built a buffer amplifier circuit using an AD620 instrumentation amplifier with a 10 GΩ input impedance that can be interposed between the filter and test equipment for low-voltage noise measurements. This should ease future characterization of new output filters.

2.2 Experimental upgrades

Several upgrades to the apparatus made during my Ph.D. are described in this section. In addition, we built an accordion lattice for preparation of isolated 2D layers, which is described in detail in Ch. 6.

2.2.1 Optical lattices

In the first generation KRb machine, a three-dimensional optical lattice was used for a variety of experiments, including suppression of collisional loss [100], study of the spin dynamics of pinned molecules [101, 102], and creation of low-entropy samples of molecules [103, 104]. The first projects on the second generation machine were conducted in a bulk gas or a stack of layers in a one-dimensional vertical lattice. The vertical lattice is made from two beams launched through the top of the cell, each focused to a waist of 240 μm at the position of the atoms. One beam, angled approximately 11 degrees from vertical to avoid etalon effects from the glass electrodes, is directly incident on the atoms. The other beam is reflected from a dichroic below the cell and hits the atoms travelling upwards, making a lattice with 540 nm spacing. Above the cell, the beam is combined with a reflection of the downward beam off the electrode on a beamsplitter cube. This allows interferometric measurement of the lattice phase relative to the electrode [105]. Stabilizing the phase through feedback to a piezoelectric actuator on a mirror was critical to layer-resolved control of the molecules (Sec. 3.2.3).

The apparatus was designed to accommodate horizontal lattices through windows in the octagonal cell. In 2022, we decided to build the horizontal lattices in order to revisit dipolar spin and spin-motion physics, using electric fields for improved control over the molecular interactions.

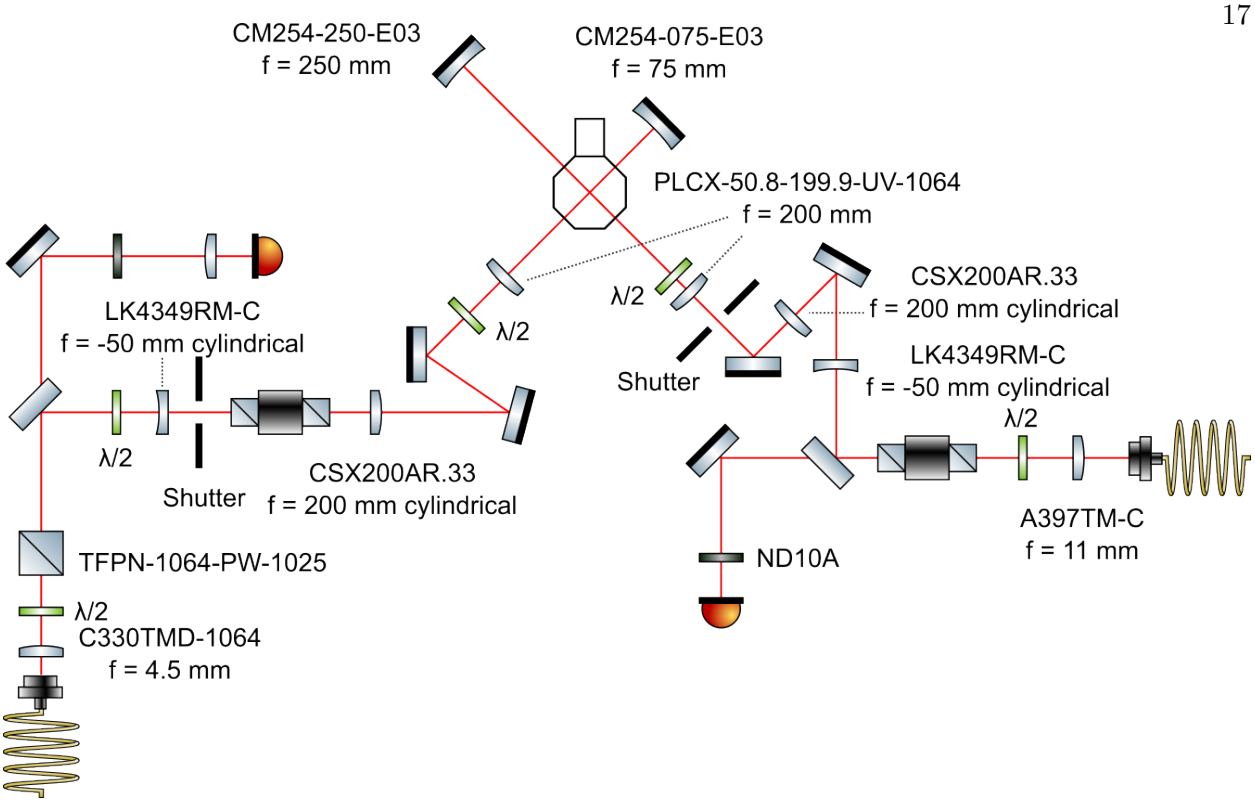

Figure 2.4: The optics for the horizontal lattices are shown schematically. The optical paths for the two lattices use different elements due to space constraints, but both deliver similarly sized beams to the atoms. The optics symbols are adapted from [106].

An overall layout of the lattice optics is shown in Fig. 2.4. Light from both lattices comes from our 1064 nm Nufern laser system and is transmitted to the experiment using NKT aeroGUIDE POWER photonic crystal fibers[13] . The beams are shaped by a 4:1 telescope and focused with waists of roughly 225 μm in the horizontal direction and 56 μm in the vertical direction at the position of the atoms. A curved mirror retroreflects the light, focusing it to a similar size to the forward beam at the position of the atoms. The polarizations of the lattices are controlled by half-waveplates in Thorlabs DDR25 motorized rotation mounts, enabling precise tuning to the magic angle [108] for state-independent trapping (Sec. 3.3.2.1) at different electric field settings.

Both the forward and retroreflected lattice beams must be well aligned to the atoms. To

[13] [107] contains a nice discussion of the photonic crystal fibers.

coarsely align the forward lattice beams, we coupled light from the Rb laser system through the fiber and optimized the pointing to maximize the depletion of a BEC with resonant light. Once this was optimized, we finely aligned the pointing by optimizing the position and depth of a crossed dipole trap made with the lattice beam and one of the xODT beams. To align the retroreflected beam, we optimized the back-coupling of light into the fiber using an optical isolator before the fiber in the laser box. Fine alignment was completed by maximizing the lattice's trap frequency.

The general physics of atoms or molecules in lattices and our procedure to calibrate the lattice depth are discussed in Sec. 3.3.1.

2.2.2 STIRAP laser system

We use STIRAP to transfer population between the Feshbach state and molecular ground state [53, 109, 110]. Previously, the up leg, at 968.3 nm, was generated using a TA seeded by an external cavity diode laser (ECDL), with a power of around 160 mW at the cell. The down leg, at 689.3 nm, generated using a diode injection locked to another ECDL, provided around 15 mW. Both lasers are Pound-Drever-Hall (PDH) locked [111] with tunable offset frequencies [83] to an ultra-low expansion cavity from Stable Laser Systems. The light enters the cell from the top and is focused to a waist of around 140 μm. With this system, the efficiency of a one-way transfer was around 85% at zero electric field, and the lasers would typically stay locked for a couple of hours before unlocking due to mode hops or drifts of the injection lock.

To improve the reliability of the system and efficiency of STIRAP, we replaced both lasers with fiber amplifier systems from Precilasers specified to output 2 W each. The up leg is generated from a doubled 1936 nm distributed feedback (DFB) seed, and the down leg uses sum-frequency generation with 1064 nm ECDL and 1957 nm DFB seeds. We also switched the PDH lock electronics from analog loop filters from the JILA electronics shop to an FPGA-based digital servo[14] . While the digital system has lower lock bandwidth than the analog loop filter, the lasers can be relocked remotely, which eases hands-off operation of the experiment. The lasers often remain locked for

[14] Liquid Instruments Moku:Lab

days at a time.

We currently operate the lasers substantially below their maximum output powers (around 140 mW for the up leg and 70 mW for the down leg) to avoid damaging the ITO coating on the glass electrodes. Nevertheless, we see improved efficiency of up to 92.0(9)% at 0 kV/cm due to the increased power and reduced noise. At higher electric fields, we see reduced efficiency, due to some combination of smaller transition dipole moments and additional electric field noise. The maximum efficiency is achieved by picking a STIRAP pulse time, here a $T = 10\,\mu$s linear ramp, that balances infidelity due to nonadiabaticity with infidelity from accumulated phase noise [112] (Fig. 2.5). Ref. [113] gives

$$P_{\mathrm{STIRAP}}(T) = \exp\left(-\frac{\tau_{\mathrm{adi}}}{T} - \frac{T}{\tau_{\mathrm{deph}}}\right) \text{ with } \tau_{\mathrm{adi}} = \frac{\pi^2\gamma}{\Omega^2} \tag{2.1}$$

as an approximate model for STIRAP efficiency. Here, Ω is the Rabi frequency of the STIRAP lasers (assuming equal Rabi frequency) and γ ($2\pi \times 6.7$ MHz for KRb [78]) is the decay rate of the excited state. The value of τ_{adi}, $0.35(5)\,\mu$s, extracted from a fit to the data, suggests that $\Omega = 2\pi \times 5.33(14)$ MHz. This agrees well with the root-mean-square value of the Rabi frequencies estimated from the transition dipole moments [78], power, and beam size of each laser, $2\pi \times 3.5(14)$ MHz for the up leg and $2\pi \times 6.7(1.1)$ MHz for the down leg.

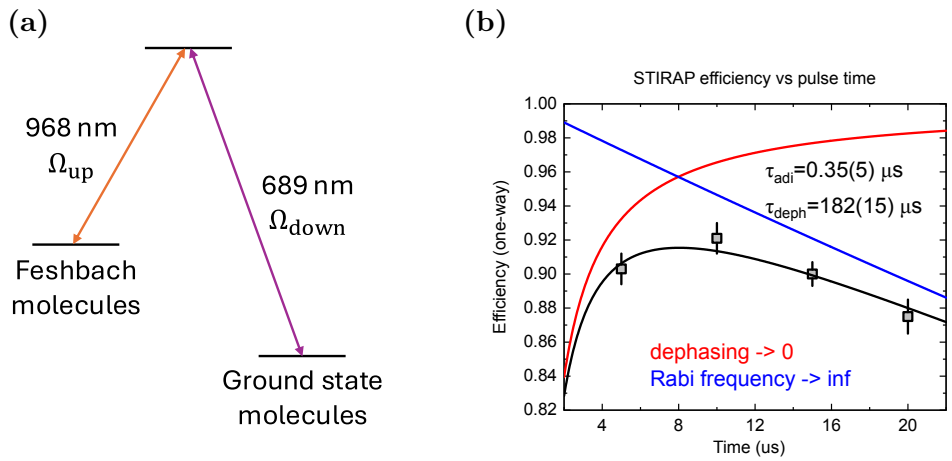

Figure 2.5: (a) The relevant levels and Rabi frequencies for STIRAP (b) The one-way STIRAP efficiency is plotted as a function of the duration of linear ramps. The black line is a fit to Eq. 2.1, from which the timescales for adiabaticity and dephasing are extracted. The red and blue lines show the expected efficiency in the absence of dephasing or in the limit of infinite Rabi frequency, respectively.

Should it be desirable to further improve the STIRAP efficiency, in order to avoid introducing additional entropy into quantum gases of polar molecules [86] or improve detection fidelity, it should be possible to both reduce τ_{adi} and increase τ_{deph}. By shining the STIRAP lasers on the molecules from the side, avoiding the ITO electrodes, it should be possible for each to deliver roughly 1 W of power with a waist $w_{z,y} = 250 \times 50$ μm. This would increase Ω by a factor of roughly 5. The coherence time τ_{deph} is likely limited by high frequency noise on the lasers. By suppressing this noise using feedforward, as discussed in [114, 115, 116], increasing τ_{deph} to a few milliseconds should be possible [113]. Eq. 2.1 suggests that these changes may allow a STIRAP efficiency greater than 99%.

2.2.3 Microwave synthesizer

We use microwaves coupled to the electrodes through a bias tee [82] to drive rotational transitions of the molecules. Prior to 2023, we generated microwaves by mixing the RF output

of an AD9910 direct digital synthesizer (DDS) with a microwave local oscillator[15] , and bandpass filtering and amplifying the upconverted output. The frequency, phase, and amplitude of the AD9910 output was selected from up to 7 preprogrammed profiles using the control system's TTL outputs, and the microwaves were enabled and disabled using a TTL-controlled RF switch.

While this system successfully provided microwaves for layer-resolved spectroscopy [105] and Ramsey spectroscopy with simple dynamical decoupling pulse sequences [117], its limitations became apparent as we began to use more complex microwave pulse sequences. The memory capacity of the FPGAs controlling the TTL outputs limited the length of the sequences to several tens of pulses, their timing resolution limited pulse fidelity, and the graphical programming of the sequence made writing new pulse sequences labor intensive and error prone. The limited number of profiles also restricted the range of pulse sequences that could be programmed and prevented the use of amplitude or phase-shaped pulses without additional hardware [84].

To resolve these issues, we worked with the JILA electronics shop to develop a programmable FPGA-based RF synthesizer based on the "Subharmonicon" system used for controlling AOMs in the Kaufman group [118]. The new synthesizer, which replaces the AD9910, has 4 RF channels generated using a Texas Instruments DAC38J84EVM high-speed digital-to-analog converter controlled by DDS cores running a Zynq UltraScale+ ZCU106 FPGA. Each channel can be programmed with up to 16384 samples updating the channel's phase, frequency (up to 307.2 MHz), and amplitude at specified times, at a rate up to 153.6 MHz. The synthesizer also has 7 digital outputs, enabling control of other devices such as switches or shutters synchronized with the microwaves.

The synthesizer is programmed over Ethernet using a Python library[16] developed for efficient, high-level representation of pulse sequences. Sequences are described using lists of pulses or toggling frame matrix representations [119], and automatically compiled to synthesizer timestamps using specified pulse shapes and calibrations of transition frequency and Rabi frequency. To ease development and debugging of sequences, the compiled pulse sequences can be plotted or used to

[15] Agilent E8257D or Valon 5009

[16] `https://github.com/krbjila/labrad_tools/tree/master/synthesizer`

drive a simulated spin system.

The new synthesizer has been used for Ramsey spectroscopy experiments with Knill dynamical decoupling (KDD) [120] sequences ([121] discussed in Ch. 5), and for randomized benchmarking [122] (discussed in Sec. 3.2.2) and Floquet pulse sequences [123] (discussed in Ch. 4 and 5). Its flexibility should allow for future explorations of higher spin systems [124] or synthetic dimensions encoded in molecular rotational states [125].

2.2.4 Robustness and automation

We made a variety of improvements to the experiment software, hardware, and procedures to simplify operation of the experiment and prevent common failures that required operator intervention. Some of the most helpful changes are listed:

- We developed updated software for controlling our Andor iXon 888 cameras. The most important change was fixing an issue where the camera would miss a trigger pulse and require a manual reset, which would happen every few hours. In the new control program, the camera is automatically reset if it does not receive the expected triggers within a shot. In addition, the camera is configured in the experiment sequence, rather than manually through a GUI, eliminating potential for operator error and simplifying storage of sequence metadata with each image.

- We set up a MongoDB database for recording images and experimental parameters, allowing automated data analysis using Python scripts and closed-loop operation of experiment. We tried using this for automatic optimization of experimental parameters using M-LOOP [126]. Unfortunately, this didn't improve the molecule conditions, possibly due to the complexity of the sequence and our long cycle time. However, we were able to implement automatic acquisition and fitting of microwave spectra to track changes in the RF frequency due to electric field drifts during long Ramsey spectroscopy datasets.

- We added an InfluxDB database for logging experimental conditions, such as temperature

and pressure of the ambient air and cooling water, frequencies of our lasers, and molecule number over time. We set up a Grafana dashboard for visualizing the data, as well as software to alert the team and automatically stop the experiment if parameters went outside normal ranges.

- We installed motorized mirror mounts with Newport Picomotors on all optical dipole trap and lattice paths, enabling precise alignment of beams without risk of disturbing the temperature of the experiment or bumping optics. This could allow automated alignment of the beams, particularly the xODT, in the future.

- We upgraded the DAC boards that control magnetic fields, laser intensities, and laser detunings. The new system still uses 48x Analog Devices AD669 DACs controlled by Opal Kelly XEM6001 FPGA development boards[17] We were able to reduce noise voltage spectral density by a factor of roughly 10 by adding 3 kHz bandwidth output filters and improving isolation between analog and digital signals. We also improved timing accuracy and synchronization between DAC boards by adding support for external clocking.

- We replaced an overly-sensitive flow rate switch used to interlock our bias coil power supply, which would sometimes trip multiple times per day. The replacement switch[18] also enables logging the flow rate. Regular replacement of the filters for the chilled water manifold is important to ensure sufficient water pressure.

Collectively, these changes enabled the experiment to operate hands-off for days at a time, rather than requiring manual intervention every couple hours. This improved the efficiency of studies requiring large volumes of data, such as [121, 123], and will benefit future projects.

[17] The XEM6001, which is also used for controlling our digital channels and electrodes, and by the Sr experiments, is no longer available for purchase. If more outputs are needed or the boards need to be replaced, the PCB and FPGA designs will need to be adapted to a newer FPGA or switched to a different solution.

[18] Proteus Industries 8000 series liquid flow meter

Chapter 3

Controlling polar molecules with electromagnetic fields

"You can't always get what you want

But if you try sometime you'll find

You get what you need"

You Can't Always Get What You Want – The Rolling Stones

In this chapter, we discuss how we use electromagnetic fields to control polar molecules. We first introduce the rotational structure of diatomic molecules, and show how d.c. electric fields can be used to tune their dipole moments (Sec. 3.1). We then discuss how microwave-frequency a.c. electric fields can coherently drive transitions between rotational states (Sec. 3.2), and present applications including preservation of coherence (Sec. 3.2.1) and layer-resolved control (Sec. 3.2.3). Finally, we discuss optical traps made using far-detuned light (Sec. 3.3), focusing on the behavior of atoms and molecules in optical lattices (Sec. 3.3.1) and magic traps which match the polarizabilities for different molecular states (Sec. 3.3.2).

3.1 Molecules in electric fields

Diatomic molecules possess a rich internal level structure, including electronic (100s of THz-scale), vibrational (THz-scale), rotational (GHz-scale), and hyperfine (100 kHz-scale) structure. For the work discussed in this thesis, the molecules are prepared in the ground electronic and vibrational level and in a single hyperfine state. The rotational levels, which can be described by a rigid rotor Hamiltonian, are of primary importance for our work, as they determine the nature of

dipolar interactions between molecules and their response to d.c. and microwave electric fields. In Sec. 3.3, we also discuss how the molecules' electronic states couple to off-resonant light, allowing optical trapping of the molecules.

In bialkali molecules (Fig. 3.12a), the electronic ground state is of $X^1\Sigma^+$ character. The superscript denotes the multiplicity, with ^{1} indicating that the two valence electron spins are in a singlet state. The X denotes that the molecule is in the electronic ground states[1] and Σ indicates that the projection of electron orbital angular momentum onto the internuclear axis Λ[2] is 0.

The rotational and hyperfine Hamiltonian of a diatomic molecule in an $X^1\Sigma$ ground state in the presence of electric and magnetic fields is

$$H_{\mathrm{KRb}} = H_r + H_d + H_{\mathrm{Zeeman}} + H_{\mathrm{hyperfine}} \tag{3.1}$$

$$H_r = B_\nu \mathbf{N}^2 \tag{3.2}$$

$$H_d = -\mathbf{d} \cdot \mathbf{E} \tag{3.3}$$

where the rotational constant $B_\nu = 1.1139$ GHz for KRb [78] and the electric dipole moment along the internuclear axis is $d = 0.574$ D [108]. The Zeeman and hyperfine structure is discussed in detail in previous theses, particularly [84], and a Julia package [127] has been developed for calculating the full Hamiltonian's spectrum. In our experiments, the molecules remain in a single hyperfine state and, for electric fields greater than a few hundred V/cm, the nuclear spins are largely decoupled from the rotational state. At zero electric field, coupling between the nuclear spins and molecular rotation allows the magnetic field to define a quantization axis for the molecular rotation and splits the nominally degenerate m_N rotational levels by approximately 100 kHz. We therefore focus our discussion on the rotational Hamiltonian.

At $|\mathbf{E}| = 0$, the eigenstates $|N, m_N\rangle$ of the rotational Hamiltonian are the spherical harmonics $Y_N^{m_N}$ with energies $E_N = B_\nu N(N+1)$. Assuming the electric field provides the quantization axis,

[1] Excited states with the same multiplicity as the ground state are labeled A, B, ... and excited states with different multiplicity are labeled a, b, c, ...

[2] $\Pi, \Delta, \ldots$ correspond to 1, 2, ... quanta

the matrix elements of the rotational and dipolar Hamiltonians are

$$\left\langle N, m_N \middle| H_r \middle| N', m'_N \right\rangle = B_\nu N(N+1)\delta_{N,N'}\delta_{m_N,m'_N} \tag{3.4}$$

$$\left\langle N, m_N \middle| H_d \middle| N', m'_N \right\rangle = -d|\mathbf{E}|\sqrt{(2N+1)(2N'+1)} \begin{pmatrix} N & 1 & N' \\ m_n & 0 & -m'_n \end{pmatrix} \begin{pmatrix} N & 1 & N' \\ 0 & 0 & 0 \end{pmatrix} \tag{3.5}$$

where the matrices are Wigner 3-j symbols [128]. Angular momentum selection rules mean that 3-j symbols are zero unless their second row sums to zero and that the elements of their first row satisfy the triangle inequality, here $|N-1| \leq N' \leq N+1$. This means that, for $^1\Sigma$ molecules, the electric field only mixes states with the same m_N and adjacent values of N. Diagonalizing the total Hamiltonian $H = H_r + H_d$ gives the field-dressed eigenstates $\left|\tilde{N}, \tilde{m}_N\right\rangle$, whose energies E_{N,m_N} as a function of electric field are shown in Fig. 3.1. In the figure and the remainder of the thesis, we use $|N, m_N\rangle$ to denote the field-dressed state $\left|\tilde{N}, \tilde{m}_N\right\rangle$ that adiabatically connects to the zero-field $|N, m_N\rangle$.

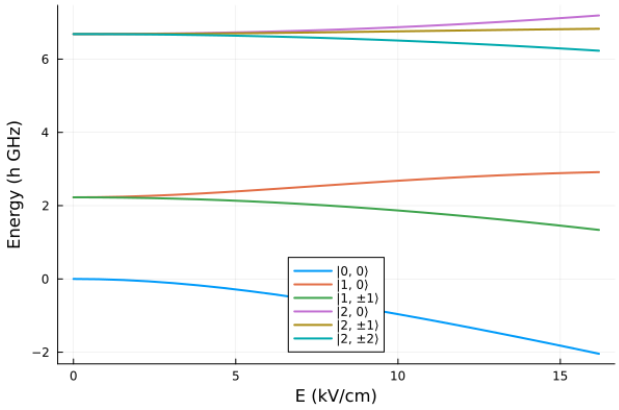

Figure 3.1: The energies of KRb's several lowest rotational levels are shown as a function of electric field, not including hyperfine structure. The states are labeled according to their undressed $|N, m_N\rangle$ quantum numbers. Calculated using [127].

The derivative of E_{N,m_N} with respect to electric field is the state's induced dipole moment in the lab frame, $d_{N,m_N} = \langle N, m_N|\mathbf{d}|N, m_N\rangle = -\frac{\partial E_{N,m_N}}{\partial|\mathbf{E}|}\hat{\mathbf{E}}$. The induced dipole moment, plotted as

a function of electric field in Fig. 3.2a, determines the force that a molecule feels in an electric field gradient generated either from an applied field or another molecule. At zero field, the rotational eigenstates are symmetric, so the lab frame dipole moment is zero. As the field is increased, the ground state $|0,0\rangle$'s dipole moment increases, while the other $|N,0\rangle$ states initially pick up a negative dipole moment that eventually becomes positive. The induced dipole moment of $|1,0\rangle$ is therefore maximized around 7 kV/cm, while the difference in induced dipole moments between $|0,0\rangle$ and $|1,0\rangle$ is maximized around 12 kV/cm. The induced dipole moments lead to Ising interactions in spin models (Ch. 4 and 5) and, at lower temperatures, spatially ordered phases [75].

The off-diagonal matrix elements $d_{N,m_N,N',m'_N} = \langle N, m_N|\mathbf{d}^p|N', m'_N\rangle$, shown in Fig. 3.2b, determine how strongly the different rotational states are coupled by electric fields carrying angular momentum $p = 0, \pm 1$. Since only adjacent N levels are coupled by H_d, transition dipole moments between N and $N+1$ are maximized at zero electric field, then gradually decrease as more rotational levels are mixed into the eigenstate. The transition dipole moments between non-adjacent $\tilde{N}$ levels increase with electric field because of the increasing admixture of adjacent N levels in the dressed states, but remain small over the range of electric fields considered. The transition dipole moments are relevant for driving rotational transitions using microwaves (Sec. 3.2) and spin-exchange interactions between molecules (Ch. 4 and 5).

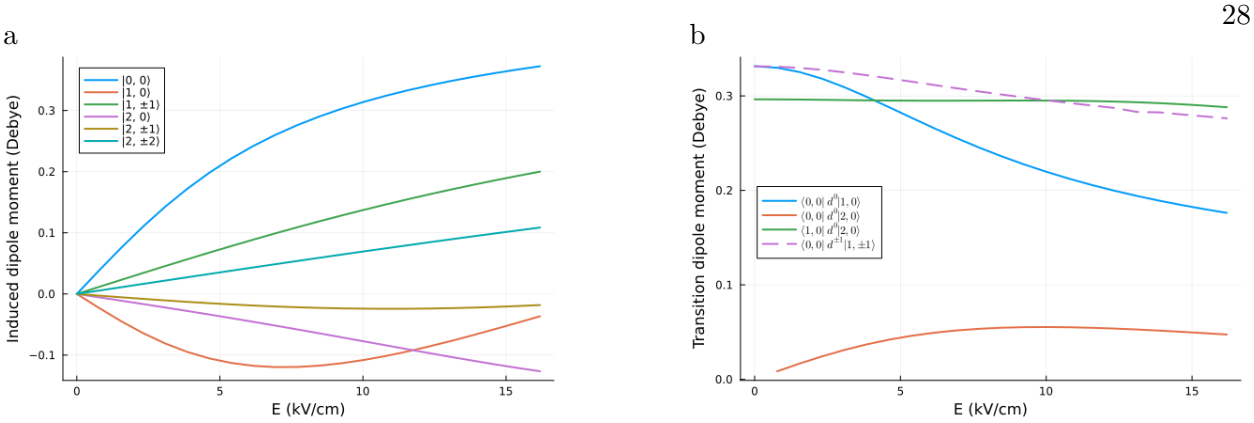

Figure 3.2: The induced (a) and transition (b) dipole moments for the lowest few rotational states of KRb are shown as a function of electric field. Calculated using [127], not including hyperfine structure.

3.2 Control with microwaves

An electromagnetic field can be used to drive transitions between rotational levels[3] . We consider microwaves with electric field $\mathbf{E}(t) = \mathbf{E}\exp\{-i\omega t\}$ with detuning Δ from a transition of energy $\hbar\omega_0$ between two molecular states $|\downarrow\rangle$ and $|\uparrow\rangle$ with transition dipole moment $d_{\uparrow\downarrow}$. Elements of $\mathbf{E}$ can be complex, encoding the phase of the electric field – the physical field is $\mathrm{Re}(\mathbf{E}(t))$. Assuming ω is far-detuned ($\Omega \ll \Delta$) from other transitions, we can neglect the effect of other energy levels. Under the rotating wave approximation[4] [129] and in a frame rotating at frequency ω_0, a state with Bloch vector $\mathbf{s} = \sum_{i\in\{X,Y,Z\}} \langle s_i\rangle \hat{i}^5$ evolves as

$$\dot{\mathbf{s}} = \mathbf{s} \times (\mathrm{Re}(\Omega)\hat{X} + \mathrm{Im}(\Omega)\hat{Y} + \Delta\hat{Z}) \tag{3.6}$$

where the Rabi frequency $\Omega = \langle\downarrow|d^p|\uparrow\rangle E_p/\hbar$, in which E_p is the component of the electric field in the spherical basis[6] with the correct polarization to connect the two states. When the microwaves are resonant with the transition ($\Delta = 0$), the Bloch vector rotates about an axis in the $X-Y$ plane,

[3] or hyperfine levels, due to coupling between the nuclear spin and molecular rotation [97]
[4] neglecting terms oscillating at high frequency $\omega_0 + \omega$, which rapidly average to zero
[5] Here and elsewhere in the thesis, we use capital letters to denote Bloch sphere directions and lowercase letters to denote real space directions.
[6] In the spherical basis, $E_0 = E_z$ and $E_{\pm1} = \mp(E_x \pm iE_y)/\sqrt{2}$.

with the axis determined by the phase of the microwaves $\arg(\Omega)$. If the microwaves are applied for $t_\pi = \pi/\omega$, the Bloch vector is rotated by an angle π, switching the population in $|\uparrow\rangle$ and $|\downarrow\rangle$. This is known as a π pulse. Similarly, $\pi/2$ pulses are often used to prepare an equal superposition from an initial state polarized along $\hat{Z}$.

Below, we discuss three applications of microwave control in our experiment. By driving appropriate dynamical decoupling pulse sequences, we can dramatically extend the coherence time of a superposition of rotational states (Sec. 3.2.1). We can characterize the fidelity of our microwave pulses by randomized benchmarking (Sec. 3.2.2). Combining static and microwave fields, we can control molecules in individual layers in our optical lattice (Sec. 3.2.3). Later, in Sec. 4.3, we discuss how microwave pulse sequences can tune interactions between molecules, allowing realization of highly tunable spin models.

3.2.1 Dynamical decoupling

One example of microwave control essential to our spectroscopic study of interactions between molecules is dynamical decoupling [130], which consists of microwave pulse sequences designed to cancel decoherence from technical noise. Due to fluctuations in electric field or molecular motion within optical or electric field gradients, the transition frequency $\omega_0(t)$ varies with time, both within single shots and between runs of the experiment. Therefore, $|\uparrow\rangle$ accumulates a phase $\Phi(t_1, t_2) = \int_{t_1}^{t_2}(\omega_0(t) - \omega(t))\,\mathrm{d}t$ relative to $|\downarrow\rangle$ over an evolution time T in a frame rotating at the microwave frequency ω. Additionally, because different molecules experience different local fields, ω_0 will vary molecule-to-molecule. This results in both dephasing between the molecules and the microwave field, with coherence time T_2^*, and dephasing between the different molecules, with coherence time $T_2 > T_2^*$. In our experiment, T_2^* is typically a few hundred microseconds, although an increase to several milliseconds has been observed using magic-angle optical traps (Sec. 3.3.2). However, for our typical interaction strengths, observation of coherent dynamics requires time evolution for milliseconds to hundreds of milliseconds, dramatically exceeding the system's technical noise limited coherence.

To understand how a microwave pulse sequence can extend the coherence, we consider the simplest dynamical decoupling sequence, known as a spin echo [131]. In spin echo, the system is allowed to evolve for time $T/2$, then a rapid π pulse is applied, swapping the states $|\uparrow\rangle$ and $|\downarrow\rangle$, before evolution for a further $T/2$. For initial state $c_\downarrow |\downarrow\rangle + c_\uparrow |\uparrow\rangle$, the state immediately before the π pulse is $c_\downarrow |\downarrow\rangle + c_\uparrow e^{i\Phi(0,T/2)} |\uparrow\rangle$, immediately after the pi pulse $c_\uparrow e^{i\Phi(0,T/2)} |\downarrow\rangle + c_\downarrow |\uparrow\rangle$, and at time T, $c_\uparrow e^{i\Phi(0,T/2)} |\downarrow\rangle + c_\downarrow e^{i\Phi(T/2,T)} |\uparrow\rangle$. Because of the π pulse, $|\uparrow\rangle$ and $|\downarrow\rangle$ have been switched, and have accumulated a relative phase of $\Phi_{\mathrm{SE}} = \Phi(0,T/2) - \Phi(T/2,T)$. If $\omega_0(t)$ is constant over the interval $(0,T)$, as in the case of ω_0 only varying shot-to-shot, $\Phi_{\mathrm{SE}} = 0$, so dephasing is fully cancelled for low frequency noise, whereas a phase of $\Phi(0,T) = (\omega_0 - \omega)T$ would be accumulated without the spin-echo.

However, higher frequency components of $\omega_0(t)$ still induce a response. Formally, assuming $\omega_0(t)$ has a single-sided power spectral density $G_\Delta(f)$, the variance of Φ is

$$\langle \Phi^2 \rangle = (2\pi)^2 \int_0^\infty G_\Delta(f) |R(f)|^2 \, \mathrm{d}f \tag{3.7}$$

in which $R(f)$ is the filter function generated by the decoupling pulse sequence [132, 133]. Based on the noise spectrum present in the experiment, we can design a pulse sequence to reduce the phase variance by minimizing the sensitivity at relevant frequencies. The filter function is the Fourier transform of the time-domain sensitivity $r(t)$ of the pulse sequence. For instance, for spin echo with instantaneous pulses, $r(t) = \begin{cases} 1 & 0 < t < T/2 \\ -1 & T/2 < t < T \\ 0 & \text{otherwise} \end{cases}$ such that $|R(f)|^2 = \frac{2}{\pi^2 f^2} \sin^4\left(\frac{\pi f T}{2}\right)$. More generally, assuming n equally spaced π pulses repeated at an interval $\tau = T/(n+1)$ with Rabi frequency Ω, the sensitivity is given in [133] as

$$|R(f)|^2 = \frac{\Omega^2}{\left(\pi f \Omega^2 - 4(\pi f)^3\right)^2} \left(2\pi f \cos(\pi f \tau) + \Omega \sin(\pi f(\tau - \pi/\Omega))\right)^2 \frac{\sin^2(\frac{\pi}{2}(1+n)(1+2f\tau))}{\cos^2(\pi f \tau)} \tag{3.8}$$

The sensitivity is plotted for different values of n for realistic experimental parameters $\Omega = 2\pi \times 100$ kHz, $T = 1$ ms in Fig 3.3. The sensitivity is strongly peaked around $f = 1/(2\tau)$ and suppressed at other frequencies, with the width of the peak decreasing with increasing T. The power spectral density of technical noise typically decreases with f, sometimes with peaks at particular frequencies. Therefore, by picking a sufficiently small τ that the passband of the sensitivity function is above the noisy portion of the spectrum and avoids prominent peaks, the effects of the noise on the state's phase can be largely cancelled. In practice, we found that τ between approximately 50 and 100 μs was effective at suppressing noise in our system (as discussed in Sec. 5.5.1 and below). We also, following the example of the lab's strontium clock experiments [132], were able to use pulse sequences with varying τ to characterize the spectrum of our electric field noise [83].

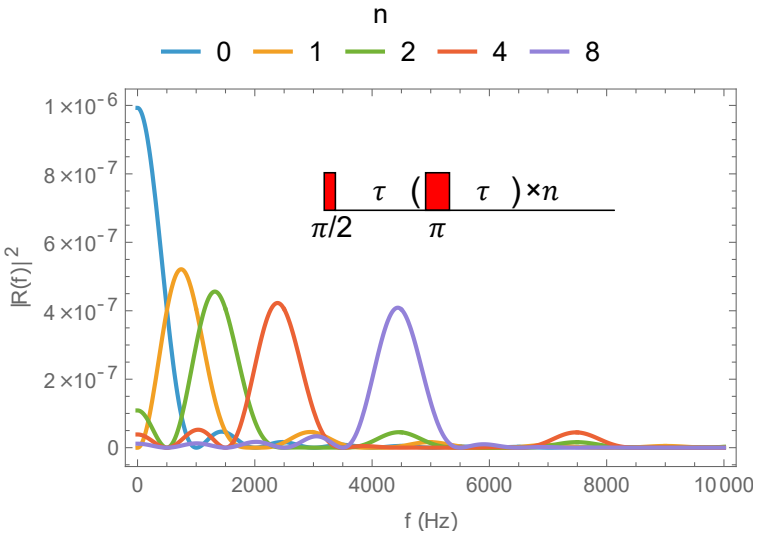

Figure 3.3: The filter function $|R(f)|^2$ for a dynamical decoupling sequence consisting of n π pulses with Rabi frequency $\Omega = 100$ kHz over a total time $T = 1$ ms is plotted as a function of frequency for different values of n. The pulse sequence, with spacing between pulses τ is $T/(n+1)$, is shown as an inset.

Unfortunately, driving larger numbers of decoupling pulses, as is required for $\tau \ll T$, has drawbacks. Typically, it is desirable to observe the dynamics of the system "in the dark", so the fraction of time during which Rabi oscillations are driven should be minimized. In addition, pulses

can off-resonantly drive molecules into other hyperfine or rotational states, leading to loss (see Sec. 5.5.1). If there is a systematic error in the rotation axis or angle of each pulse, the errors can accumulate over long pulse sequences, resulting in deviations from the desired final state. This can be partially mitigated through designing pulse sequences in which the errors cancel instead of adding up. In the case of dynamical decoupling sequences, this is typically done by varying the axis about which the pulses are applied. For instance, if a pulse of nominal area π rotates by an angle $\pi + \epsilon$ about an axis $\hat{\phi}$, a second pulse with the same area about $-\hat{\phi}$ will restore the initial state. Rules for designing robust decoupling pulse sequences are discussed in [119]. We used two dynamical decoupling pulse sequences robust to pulse errors, XY8 [134] in [117, 123] and KDD [120] in [121]. While more complex than XY8, KDD is less sensitive to pulse errors.

3.2.2 Pulse fidelity

In [123], we characterized the fidelity of our microwave pulses driving the $|0,0\rangle \leftrightarrow |1,0\rangle$ transition using the one-qubit randomized benchmarking sequence described in [122]. In brief, we applied a series of alternating $\pi/2$ and π pulses, where the axis of $\pi/2$ pulse was selected at random from $\{+X, -X, +Y, -Y\}$ and the axis of each π pulse was selected at random from $\{+X, -X, +Y, -Y, +Z, -Z, \emptyset\}$ (rotations about the $\pm Z$ axis are implemented by incrementing the RF synthesizer phase, swapping the orientation of the axes about which future pulses are performed, and no pulse is performed for $\emptyset$). The pulses were spaced by 1 μs. Sequences with a variable number N of $\pi/2$ pulses were applied, after which a final $\pi/2$ pulse was applied, if necessary, to rotate the expected Bloch vector direction to the $\pm Z$ axis. $\langle S \rangle_z$ over the ensemble was measured with state-resolved imaging and the experiment was repeated for different N and different random pulse sequences. The fidelity per $\pi/2$ pulse was determined by fitting the alignment of the spins with the expected state to exponential decay with time constant τ, reporting $F = 1 - 1/(2\tau)$. At 1 kV/cm, we measured fidelities of 0.99941(9) per $\pi/2$ pulse with itinerant molecules confined by a 65 E_r vertical lattice and 0.99915(14) with molecules pinned in a 65 E_r 3D lattice (shown in Fig. 3.4a). At 0 kV/cm, we measured a lower fidelity of 0.9941(9) with itinerant molecules, which we

attribute to off-resonant driving of other nearby hyperfine states. These fidelities are not limited by any fundamental effects and, in the future, could be improved through some combination of reducing electric field noise, using magic optical traps, and characterizing and improving phase and amplitude noise of the microwave synthesizer[7] .

It is worth noting that these fidelities are conditional on the molecules being detected. We saw a reduction in the molecule number as longer pulse sequences were applied, shown for the 1 kV/cm, 65 E_r 3D lattice data in Fig. 3.4b. The number loss, with a time constant of 4203(365) $\pi/2$ pulses (corresponding to 35.7(31) ms), is much faster than the expected lifetime of approximately 20 s in the deep 3D lattice [100]. We believe that the loss is due to off-resonant driving into other hyperfine states, and would be improved with lower Rabi frequency. This sort of loss, roughly analogous to erasure errors in quantum computing [135, 47], is less impactful for metrology or some many-body physics applications than errors in which the spins stay within the qubit manifold.

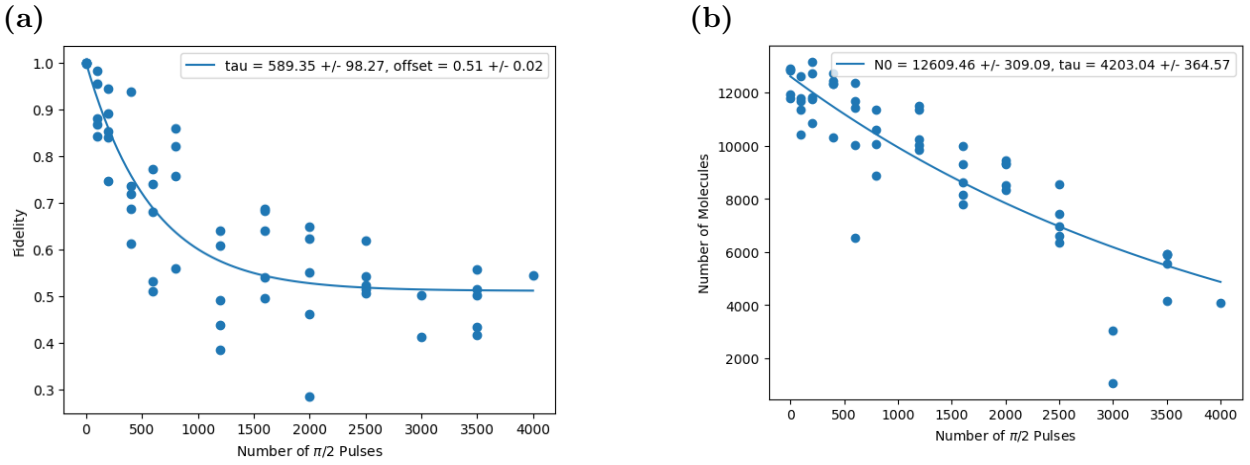

Figure 3.4: **Randomized benchmarking of microwave rotations** (a) The measured fidelities of random pulse sequences of varying length N $\pi/2$ pulses are plotted as a function of N and fit to an exponential decay model. The data shown here are taken at $|\mathbf{E}| = 1$ kV/cm in a 65 E_r 3D optical lattice. (b) The total molecule number during the measurement, fit with an exponential decay model.

[7] Technical details of the microwave system are discussed in Sec. 2.2.3

3.2.3 Layer-resolved control

Manipulation of the molecules using microwaves and static electric fields can be combined, enabling new scientific applications. For instance, we demonstrated the ability to perform layer-resolved state preparation and measurement in an optical lattice [83]. To do so, we applied an electric field gradient along the wavevector of our vertical optical lattice (Fig. 3.5a). Because the frequency of the $|0,0\rangle \leftrightarrow |1,0\rangle$ transition increases with electric field (Fig. 3.5b), it varies as a function of position along the gradient. For the parameters used in the experiment, $|\mathbf{E}| = 1$ kV/cm and $\partial_y |\mathbf{E}| = 6.4(2)$ kV/cm^2, adjacent layers 540 nm apart had transition frequencies differing by 14 kHz.

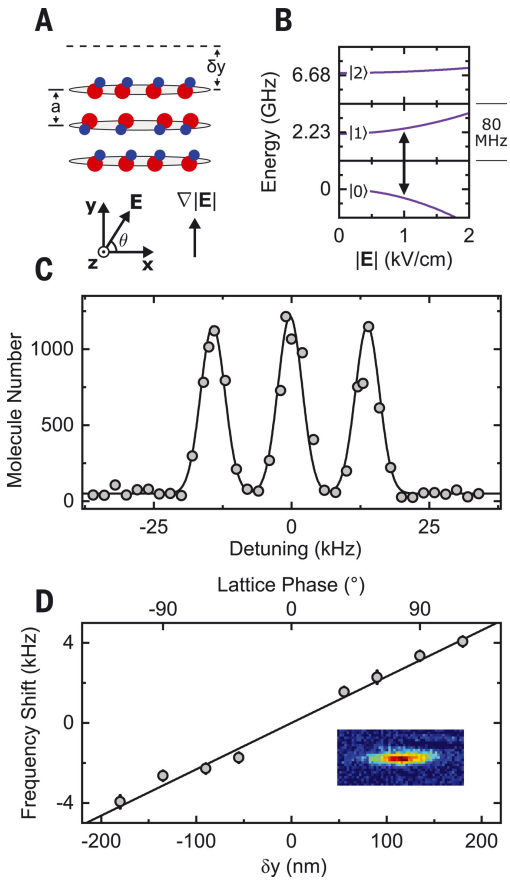

Figure 3.5: **Layer-resolved control** (**a**) Molecules occupied 2D layers in the $x-z$ plane, separated by layer spacing a. The bias electric field $\mathbf{E}$ was oriented at an angle θ in the $x-y$ plane, with an electric field gradient parallel to y. The lattice layers were displaced relative to the reference frame of electrodes generating $\mathbf{E}$ by a distance δy. (**b**) The KRb rotational structure is shown as a function of $|\mathbf{E}|$. The arrow indicates the layer selection transition. (**c**) $|0,0\rangle \leftrightarrow |1,0\rangle$ frequency spectrum of a trilayer at $\partial_y|\mathbf{E}| = 6.4(2)$ kV/cm^2. Only three adjacent lattice layers were populated. (**d**) Center frequency shift of layer selection versus δy. Displacements smaller than 20 nm were measured. Error bars are 1 standard error from fits to the rotational transition line shape. An absorption image of a single layer is shown in the inset. From [105].

By driving appropriate sequences of narrow microwave pulses resonant with a single layer, broad microwave pulses resonant with the entire ensemble, and pulses from the STIRAP down leg, which depleted molecules in $|0,0\rangle$ and $|1,0\rangle$, we were able to prepare arbitrary combinations of

occupied layers in different internal states. An example sequence for preparing an isolated trilayer with a central layer in $|0,0\rangle$ and the outer layers in $|1,0\rangle$ is shown in Fig. 3.6. Fig. 3.5c shows an example of preparation and layer-resolved detection of an isolated trilayer. After preparing a trilayer in $|1,0\rangle$, a final narrow pulse with variable detuning is applied to transfer the molecules at some position to $|0,0\rangle$ before imaging.

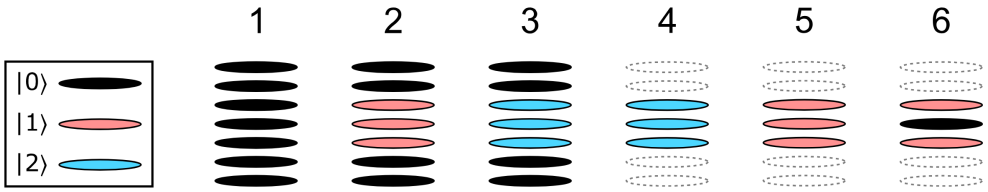

Figure 3.6: A sequence for preparing an isolated trilayer, with the inner layer in state $|0,0\rangle$ and the outer layers in $|1,0\rangle$. From [105].

The layer-resolved control places fairly stringent requirements on stabilization of the lattice and electric field and homogeneity of transition frequency within a layer. The electric field at the position of a layer molecules must be repeatable to within tens of mV/cm to ensure that its transition frequency does not change by more than a few kHz shot-to-shot. This is achieved by stabilizing the electrode voltages to a precision voltage reference (Sec. 2.1.5 and [83]) and interferometrically stabilizing the optical lattice to the electrodes to prevent motion of the layers along the electric field gradient. Fig. 3.5d shows the RF frequency of a layer changing as a function of lattice phase, indicating that changes of position of below 20 nm could be controlled and resolved. Electric field gradients in the horizontal direction would inhomogeneously broaden each layer's spectrum. The projection of the gradient along the **z** direction is minimized by optimizing the lattice's tilt relative to the electrodes and gradients in the **x** direction are minimized by adjusting the voltages applied to the electrodes. To minimize broadening from a.c. Stark shifts, the electric field is rotated to approximately 36° from the **y** axis, such that the lattice polarization is magic (Sec. 3.3.2).

We used the layer-resolved control and detection to probe spin-exchange interactions between layers that lead to molecule loss [105]. The same capability will be for future studies of superfluidity

in bilayers [136] or pair creation [137] or transport [138] across stacks of layers.

3.3 Optical trapping

We use optical dipole traps, formed from laser beams red-detuned from electronic transitions, to confine atoms and molecules in our experiment. In the presence of light with intensity $I(\mathbf{r})$, a particle experiences an AC Stark shift $U = -\alpha I(\mathbf{r})$, where α is the particle's polarizability[8] . Optical trapping is a standard technique in the ultracold community [139], so we focus our discussion on two topics important to our experiment. First, we discuss optical lattices, used to confine our atoms and molecules to lower dimensions and to regulate their motion. We present a brief introduction to the physics of particles in lattices and discuss techniques for calibrating the depth of an optical lattice (Sec. 3.3.1). Second, diatomic molecules like KRb exhibit different polarizabilities along and perpendicular to the internuclear axis, so their polarizability in general depends on their rotational state, the polarization of the trapping light, and applied electric or magnetic fields which can orient the molecule. We discuss how magic traps, where the polarizabilities of different rotational states are equal, can be created by tuning the polarization or wavelength of the trapping light (Sec. 3.3.2).

3.3.1 Optical lattices

Interference of laser beams generates wavelength-scale interference patterns, creating a highly regular potential landscape for atoms or molecules analogous to the crystal lattices of materials. For two plane waves, each with wavelength λ and intensity I, interfering at a half-angle θ from the x axis in the $x-y$ plane, the electric field is the sum of their individual electric fields,

$$\mathbf{E}(\mathbf{r},t) = \hat{\mathbf{E}}\sqrt{\frac{2I}{\epsilon_0 c}}e^{-i\omega t}\left(e^{i\mathbf{k}_1\cdot\mathbf{r}} + e^{i\mathbf{k}_2\cdot\mathbf{r}}\right) \tag{3.9}$$

where $\mathbf{k}_1 = \frac{2\pi}{\lambda}(\cos(\theta)\hat{x} + \sin(\theta)\hat{y})$, $\mathbf{k}_2 = \frac{2\pi}{\lambda}(\cos(\theta)\hat{x} - \sin(\theta)\hat{y})$, c is the speed of light, and ϵ_0 is the permittivity of free space. The potential in the resulting lattice is

[8] The polarizabilities of K, Rb, and KRb at 1064 nm are 28, 32, and 55 h Hz/(W/cm^2) respectively [84].

$$V_{\text{latt}}(r) = -\alpha\frac{\epsilon_0 c}{2}|\mathbf{E}(\mathbf{r},t)|^2 = -4\alpha I\cos^2\left(\frac{2\pi\sin(\theta)}{\lambda}r\right) = -V_0\cos^2\left(\frac{\pi}{a}r\right) \tag{3.10}$$

The maximum depth V_0 of the lattice potential is enhanced by a factor of two compared to non-interfering plane waves and the spacing a, corresponding to a lattice wavevector $k = 2\pi/a$, of intensity maxima can be varied between $\lambda/2$ at $\theta = \pi/2$ (counterpropagating beams) and ∞ at $\theta = 0$ (copropagating beams). The recoil energy $E_r = \frac{\pi^2\hbar^2}{2ma^2}$ is the characteristic energy scale for lattice physics. For K, Rb, and KRb in a lattice with $a = 532$ nm, $E_r/k_B = 211, 97$, and 67 nK respectively.

Within the lattice, atoms or molecules behave qualitatively differently from free space, occupying distinct energy bands and allowing description with discrete second-quantized real-space Hamiltonians. We give an intuitive description and present key results based on the tight binding model, but refer the reader to [140, 16] for detailed derivations. We also only discuss one-dimensional lattices, since in our experiment, the lattice is separable such that the eigenstates can be factored into $\psi(\mathbf{r}) = \psi_x(x)\psi_y(y)\psi_z(z)$. According to Bloch's theorem, eigenstates of a 1D lattice are functions of the form $\psi_q(r) = e^{iqr}u_q(r)$ where $u_q(r) = u_q(r+a)$ is a periodic function. A convenient basis is localized states $|j\rangle$ with wavefunctions given by the Wannier functions $\varphi_n(r - R_j)$ centered around site j at position R_j [141]. The eigenstates can then be written as the superposition $\psi_q^n(r) \propto \sum_j e^{iqR_j}\varphi_n(r - R_j)$ where $q \in (-\hbar k, \hbar k)$ is the crystal momentum and n is the band index.

To find the approximate form of the Wannier functions in a deep lattice (V_0 of at least several E_r), we can expand the lattice potential in a Taylor series about a potential minimum, finding $V_{\text{latt}}(r) = -V_0 + \frac{1}{2}m\omega^2r^2 + \mathcal{O}(r^4)$ where m is the mass of the particle and $\omega = \sqrt{\frac{2\pi^2V_0}{ma^2}} = \frac{2E_r}{\hbar}\sqrt{\frac{V_0}{E_r}}$ is the trap frequency. Then $\varphi_n(r)$ can be approximated as the nth harmonic oscillator wavefunction with energy $E_n = \langle j|\hat{H}|j\rangle \approx \hbar\omega(n + 1/2)$. We are typically interested in the regime where $k_BT \ll \hbar\omega$, such that only the $n = 0$ states are occupied; therefore, we drop the n index. The ground band Wannier functions (solid blue line) and the approximating harmonic oscillator wavefunction (dashed black line) are shown in Fig. 3.7 for different lattice depths, showing more

favorable agreement for deeper lattices.

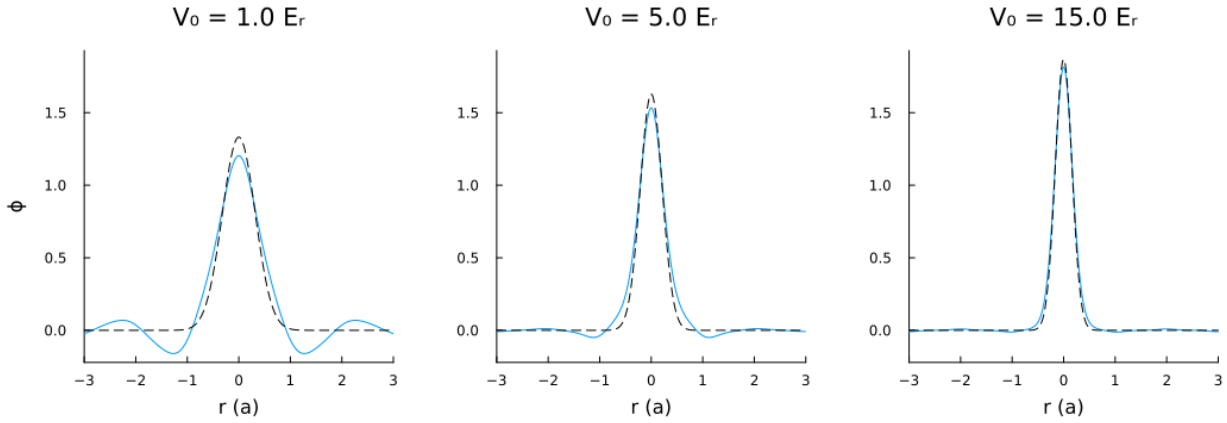

Figure 3.7: The ground band Wannier functions (solid blue line) and harmonic oscillator approximations (dashed black line) are plotted for lattices of depth 1, 5, and 15 E_r.

The dominant perturbation from isolated sites is coupling between neighboring sites arising from overlap of the tails of their wavefunctions. The matrix element $t = \langle j|\hat{H}|j+1\rangle/h = \frac{1}{h}\int \varphi_0(r)^* \left(-\frac{\hbar^2}{2m}\frac{\partial^2}{\partial r^2} + V_{\text{latt}}(r)\right)\varphi_0(r+a)\,\mathrm{d}r$, here given in frequency units, is known as the tunneling rate. For accurate calculation of t, it is necessary to use the Wannier functions instead of their harmonic oscillator approximations due to their heavier tails [52]. [142] gives the tunneling rate in a deep lattice as

$$t \approx \frac{4E_r}{\sqrt{\pi}h}\left(\frac{V_0}{E_r}\right)^{3/4}\exp\left(-2\sqrt{\frac{V_0}{E_r}}\right) \tag{3.11}$$

Numerically calculated and approximate values of t are plotted as a function of V_0 in Fig. 3.8.

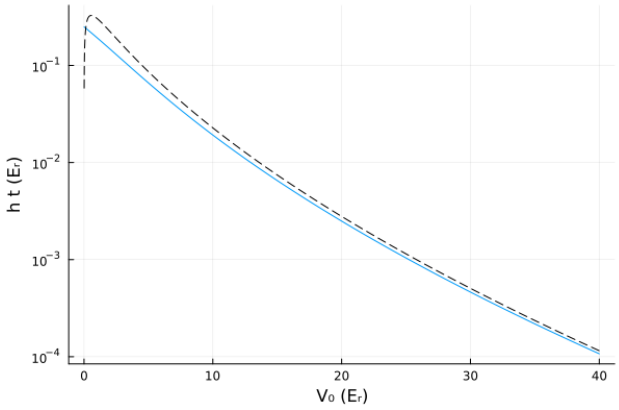

Figure 3.8: The tunneling rate t is plotted as a function of the depth V_0 of a sinusoidal lattice (solid blue line). The approximate form Eq. 3.11 is also shown (dashed black line).

The tight-binding Hamiltonian for a single particle is $-ht\sum_j(|j\rangle\langle j+1| + |j+1\rangle\langle j|)$. Diagonalizing it results in eigenstates with energies forming bands around the original levels E_n, with the ground band having width $\Delta E_0 = 4ht$ [52] (Fig. 3.9). To describe multiple particles, the Hamiltonian can be written in second-quantized form $H_t = -ht\sum_{\langle ij\rangle}(\hat{c}_i^\dagger\hat{c}_j + \hat{c}_i\hat{c}_j^\dagger)$, where the sum is taken over nearest neighbors and $\hat{c}_i^\dagger$ ($\hat{c}_i$) are creation (annihilation) operators for particles with the appropriate statistics at site i. As discussed in Sec. 5.4.1, additional terms can be added to describe interactions between particles.

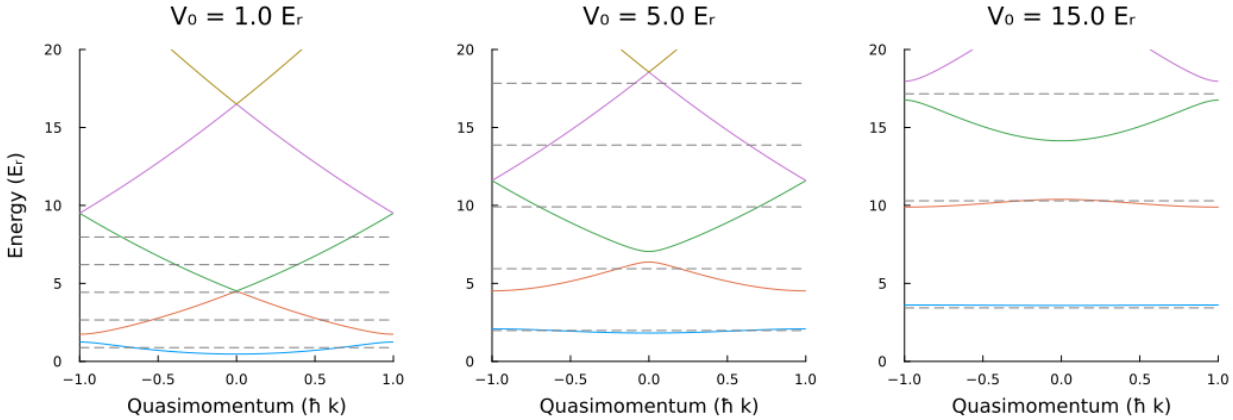

Figure 3.9: The dispersion is plotted for the lowest three bands of lattices of depth 1, 5, and 15 E_r. The corresponding harmonic oscillator energy levels are shown as dashed horizontal lines, which the lower eigenvalues approximate for deeper lattices.

Experimentally, we calibrate the lattice depths using parametric heating [80, 81], modulating the lattice depth by approximately 10% at a variable frequency ω_p. When ω_p is resonant with the gap between the $n = 0$ and $n = 2$ bands, particles are excited to the higher band[9] . We typically use a rubidium BEC for parametric heating, since the atoms are concentrated at $q = 0$, rather than spread throughout the band in a thermal or Fermi gas. This leads to a narrower resonance and easier interpretation of the data. For deep lattices, the spacing between the $n = 0$ and $n = 2$ bands scales like $2\hbar\omega$, although a substantial deviation persists up to tens of recoils. The numerically calculated (solid blue line) and approximate (dashed black line) splittings are plotted as a function of lattice depth in Fig. 3.10.

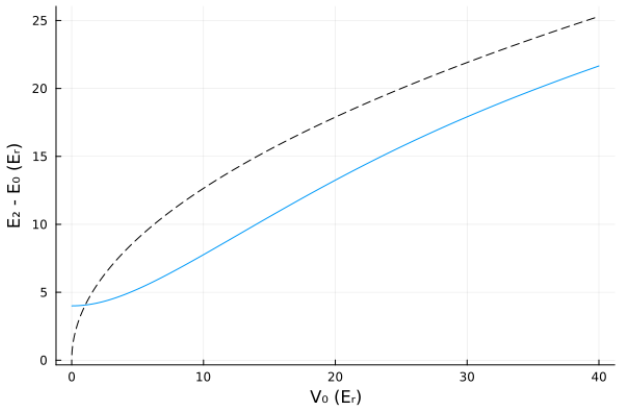

Figure 3.10: The $q = 0$ splitting between the $n = 0$ and $n = 2$ bands, corresponding to the energy for resonant parametric heating of a BEC, is plotted as a function of lattice depth (solid blue line). An approximation of $2\hbar\omega$ is plotted as a dashed black line.

3.3.2 Controlling a.c. Stark shifts

For high-fidelity control and realization of spin models without strong local disorder, it is desirable that each molecule has the same splitting ω_0 between $|\uparrow\rangle$ and $|\downarrow\rangle$. The splitting is sensitive to d.c. electric field, but because the electrodes are large and far from the molecules, the field is smooth over the sample, and can be homogenized by controlling the electric field gradient and

[9] Due to the anharmonicity of the lattice, the $n = 0$ to $n = 1$ transition can also be driven, although more weakly [143]

curvature (Sec. 2.1.5). However, the optical field from the dipole traps and lattices varies over a much smaller scale, due to the both the Gaussian shape of the beams, which is needed to confine the atoms and molecules, and various imperfections in their wavefronts.

If the states $|\uparrow\rangle$ and $|\downarrow\rangle$ have polarizabilities $\alpha_\uparrow$ and $\alpha_\downarrow$ respectively, the splitting changes by $\Delta\omega_0 = (\alpha_\uparrow - \alpha_\downarrow)I/\hbar$ when the molecule is exposed to light of intensity I. For KRb at 1064 nm, $\alpha_\uparrow$ and $\alpha_\downarrow$ can be different by as much as 30% [108], leading to decoherence within a few hundred microseconds for typical trap geometries. To achieve long coherence times, it is therefore important to engineer trapping light in which $\alpha_\uparrow = \alpha_\downarrow$.

Diatomic molecules generically have different polarizabilities for light with electric field along and perpendicular to the internuclear axis, $\alpha_\parallel$ and $\alpha_\perp$ respectively. Because the wavefunctions of different rotational states have different distributions of orientations of the molecule, the orientation-averaged polarizability can depend on the state. Several methods have been developed for making "magic" traps, which equalize the polarizabilities for two or more states of interest. In the following sections, we discuss two such methods, a magic angle, which we frequently use, and a magic wavelength, which we investigated spectroscopically. Other methods in use within the ultracold molecule community include magic ellipticity [144, 145], intensity [146], and magnetic field [146, 147] traps.

3.3.2.1 Magic angle

We consider the case where the molecule is exposed to light with linear polarization at angle θ to the rotational states' quantization axis, defined by the direction of an applied d.c. magnetic or electric field. Due to the spherical symmetry of its wavefunction, $|0,0\rangle$'s polarizability $\alpha_{|0,0\rangle} = (\alpha_\parallel + 2\alpha_\perp)/3$ is isotropic. In addition to scalar polarizability, excited rotational states have an additional tensor polarizability $\alpha^{(2)} \propto \alpha_\parallel - \alpha_\perp$, such that $\alpha_{|N,m_N\rangle} = \alpha^{(0)}_{|N,m_N\rangle} + \alpha^{(2)}_{|N,m_N\rangle}\langle P_2(\cos(\theta))\rangle_{|N,m_N\rangle}$, where the Legendre polynomial $P_2(\cos(\theta)) = (3\cos^2(\theta) - 1)/2$ and the average is taken over the state's angular wavefunction [148]. The anisotropic component therefore vanishes at the magic angle $\theta_0 = \arccos\left(1/\sqrt{3}\right) \approx 54.7°$.

Experimentally, we are often concerned with a spin encoded in the $|0,0\rangle$ and $|1,0\rangle$ or $|1,\pm1\rangle$ rotational states. This case is complicated by the light coupling different rotational states, with off-diagonal matrix elements comparable to the 100 kHz-scale nuclear quadrupole splittings between the $N = 0, \pm1$ states at realistic light intensities. This coupling necessitates diagonalizing the full Hamiltonian of the $N = 1$ states, shifting the magic angles for each pair up to several degrees from each other and θ_0 [108] (Fig. 3.11a). In addition, the mixing of rotational states from an applied d.c. electric field will also change $\alpha^{(2)}$ and the magic angle. We therefore optimized the angle of our optical traps for each electric field, using an adjustable waveplate to find the angle that minimizes the shift in transition frequency for different light intensities. Even so, it is not possible to realize a perfectly magic trap, as the magic angle depends on light intensity, leading to higher order polarizabilities.

Magic angle traps for polar molecules were first demonstrated using KRb in [108], facilitating study of spin models in [101], and subsequently used for NaK [149] and CaF [150]. In our apparatus, it is possible to simultaneously reach the magic angle with the optical dipole traps and horizontal lattices for a vertical electric field[10] . This condition was used in [121] to allow the lattice depths to be changed without having to rescan RF parameters. By tilting the electric field approximately 36° from vertical, the vertical lattice can also be made magic. We used this in [105] to demonstrate rotational coherence times up to several milliseconds (Fig. 3.11b) and reduce inhomogeneous broadening for layer-resolved spectroscopy (Sec. 3.2.3).

[10] The accordion lattice does not currently have a waveplate for polarization control, but could also reach the magic angle if such a waveplate was added.

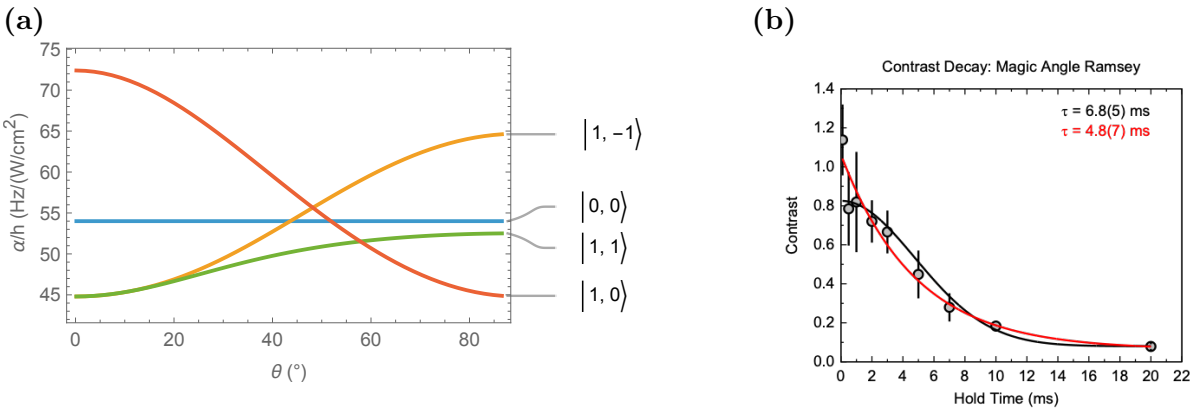

Figure 3.11: (a) The calculated polarizabilities of the $N = 0$ and 1 states at zero electric field and 2.3 kW/cm^2, following [108] The x-coordinate of the intersections between curves denote the magic angle for the corresponding transition. (b) The Ramsey contrast decay of KRb in a 1D lattice tuned to the magic angle by rotating the electric field to approximately 36° from vertical is plotted, fit with Gaussian (black) and exponential (red) contrast decay curves. The contrast decay time of approximately 5 ms is much greater than the few hundred microsecond time observed in a non-magic trap.

3.3.2.2 Magic wavelength

An alternative approach to generating state-independent traps is picking a trap wavelength where $\alpha_{\parallel} = \alpha_{\perp}$, so the polarizability is independent of orientation. This approach would allow simultaneous creation of magic or near-magic traps for multiple rotational levels [151] and allow more flexible trap geometries with less sensitivity to errors in polarization. In bialkali molecules (Fig. 3.12a), the electronic ground state is of $X^1\Sigma^+$ character (Sec. 3.1). Light with polarization parallel (perpendicular) to the internuclear axis couples to transitions where $\Delta\Lambda = 0$ ($\Delta\Lambda = \pm 1$). The transition to the excited triplet $b^3\Pi$ state is electric dipole forbidden since it requires flipping an electron spin, but can be weakly driven because of mixing with the nearby $A^1\Sigma^+$ state [151]. This admixture means that the $X^1\Sigma^+ \leftrightarrow b^3\Pi$ (X-b) transition can be driven by light with parallel polarization. As a result, $\alpha^{\parallel}$ varies strongly with detuning Δ from the transition, but $\alpha_{\perp}$ is nearly constant, since the nearest state coupled by perpendicularly polarized light, $B^1\Pi$, is detuned by

hundreds of terahertz (Fig. 3.12b). By picking an appropriate Δ, the two polarizabilities can be matched, allowing for magic wavelength trapping.

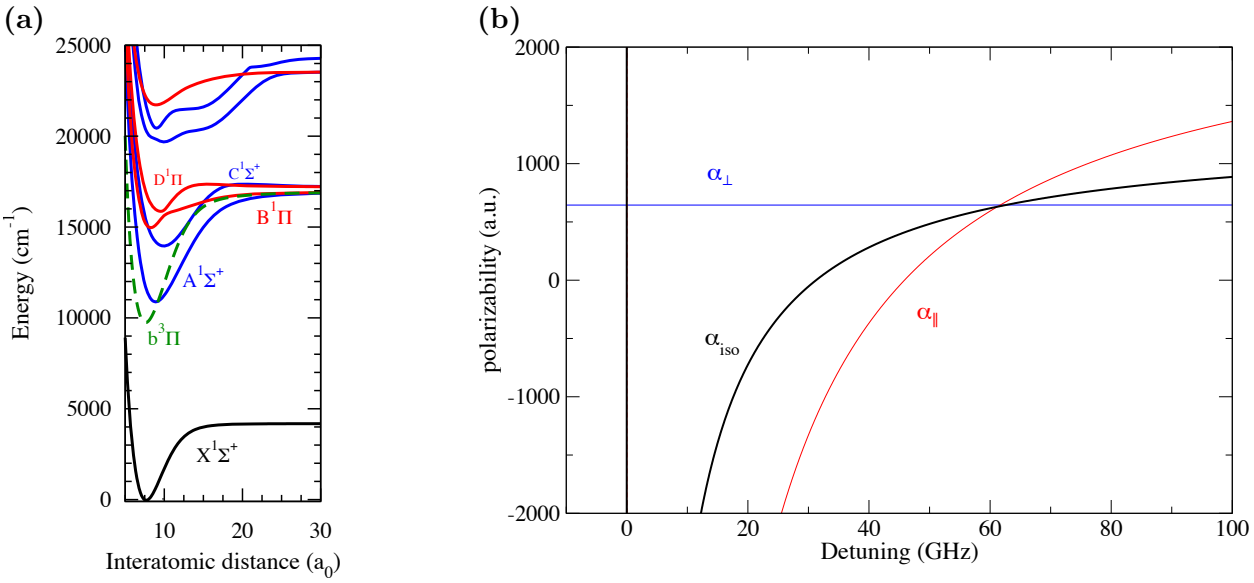

Figure 3.12: (a) The potential energy curves of the lowest several electronic states of KRb. From [152]. (b) Theoretical estimates of $\alpha_\parallel$, $\alpha_\perp$ and their weighted average $\alpha_{\rm iso}$ for KRb in the vicinity of the X-b transition. They were predicted to intersect at a magic detuning of approximately 60 GHz. From a private communication with Olivier Dulieu and Romain Vexiau.

This approach was first demonstrated in [153], where a laser near the X-b transition of NaK was tuned to engineer a magic wavelength between the $N = 0$ and $N = 1$ rotational states, as well as tuneout wavelengths at which $\alpha = 0$ for both levels. Although only approximately 10 GHz detuned from the X-b transition, the narrow 13.0(5) kHz linewidth was predicted to enable lifetimes of approximately one second in a magic trap. The magic wavelength for RbCs has also been extensively used, allowing second-scale rotational coherence times in an optical dipole trap [154], record entangling gate fidelities and Bell state coherence times in optical tweezers [155], and simultaneous magic trapping of three rotational states [156]. Given its enabling potential for highly coherent spin physics, we decided to explore whether these methods could be applied to KRb. In this section, I present preliminary measurements of the X-b transition in ^{40}K^{87}Rb and discuss

prospects for a magic-wavelength trap.

The X-b transition in ^{41}K^{87}Rb was previously observed [157] with the intent of directly laser cooling the molecules. Since we expect isotope shifts to be small, we used their measured frequency of 291.4172(2) THz as the starting point for our search. To generate light around 1028.7 nm to drive the transition, we built an external cavity diode laser, which we locked to a wavemeter. After an optical isolator and fiber, the laser delivered around 2 mW to the molecules. The beam was focused to a waist of 135 by 150 μm, giving a peak intensity of approximately 6 W cm^{-2}. This intensity is substantially lower than that required to make an optical dipole trap (only corresponding to a trap depth of 9 nK at the theoretically estimated real polarizability of 645 a.u. = $30h$ Hz/(W/cm^2)), so sensitive spectroscopy and careful elimination of systematic shifts was required to measure the polarizability of the molecules.

To characterize the polarizability of the molecules, we used double resonance spectroscopy (Fig. 3.13a), where we measured the frequency of the $|0,0\rangle$ ($|0\rangle$) to $|1,0\rangle$ ($|1\rangle$) rotational transition while the molecules are exposed to light near the X-b transition. Ramsey interferometry with a spin echo pulse sequence, with the laser applied before the echo pulse, enables this measurement (Fig. 3.13b). Phase shifts due to static disorder are canceled by the echo pulse, but the frequency shift from the different energy shifts of $|0\rangle$ and $|1\rangle$ due to the laser shifts the phase of the Ramsey fringe. The phase of the Ramsey fringe was measured to approximately 5° precision and Ramsey interrogation times of up to 20 ms are used, giving sensitivity to frequency shifts of 0.7 Hz. Because the Ramsey phase can wrap to values beyond 2π when the frequency shift is large, measurements were also taken at shorter Ramsey times to disambiguate the frequency shift.

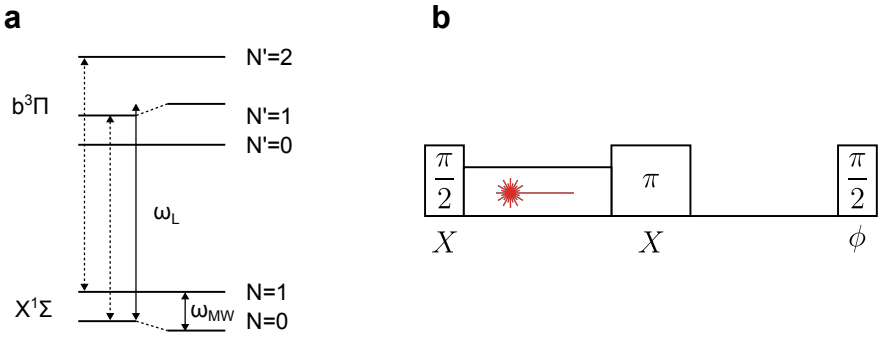

Figure 3.13: (a) The double resonance spectroscopy scheme is shown schematically. A laser at frequency ω_{L} connects levels in the ground and excited state manifolds, inducing an a.c. Stark shift in the $|0\rangle \leftrightarrow |1\rangle$ transition. The Stark shift is measured using microwaves at frequency ω_{MW}. Here, the laser is shown as blue detuned from the $|N = 0\rangle \leftrightarrow |N' = 1\rangle$ transition; the other allowed rotational transitions from $|0\rangle$ and $|1\rangle$ are shown as dashed arrows. (b) The spin-echo pulse sequence for measuring the a.c. Stark shift while rejecting other frequency shifts is shown. The sequence consists of an initial $\pi/2$ pulse, after which the laser is turned on for time T, after which a π pulse flips the state about the $\hat{X}$ axis. The spins evolve for another T in the dark, and a final $\pi/2$ pulse with variable phase ϕ maps the accumulated phase onto $\langle S_z \rangle$.

For these measurements, we produced approximately 10^4 KRb molecules at an average filling fraction of approximately 10% in a 3D optical lattice to suppress motion and collisional loss. Time-dependent disorder and dipolar interactions can lead to contrast decay, which reduces the measurement sensitivity. Because the molecules are pinned by a 3D lattice, the dominant remaining source of disorder is time-varying a.c. Stark shifts from intensity noise of the optical lattice (hence the need for a magic wavelength trap). To minimize this effect, the two horizontal lattices were set to the magic angle while the polarization of the vertical lattice was fixed at 90° from the quantization axis, which is defined by a 545.9 G magnetic field. In this configuration, the Ramsey coherence time was 9 ms with a spin echo pulse. The coherence time was still limited by dipolar interactions between the molecules [101, 121]. Therefore, for the double resonance spectroscopy measurements, the density of the molecules was uniformly reduced by shelving 30% of the molecules in $|1\rangle$ while

removing molecules in $|0\rangle$ through application of resonant light from the STIRAP down leg [117]. This increased the spin echo coherence time to approximately 25 ms, which is sufficient for the polarizability measurement.

We found three dispersive features in the RF spectrum, corresponding to light resonant with the $|X,0\rangle \leftrightarrow |b,1\rangle$, $|X,1\rangle \leftrightarrow |b,0\rangle$, and $|X,1\rangle \leftrightarrow |b,1\rangle$ transitions (Fig. 3.14a). Fitting this spectrum to the model from [153], we extract a transition frequency of 291.41725(5) THz and an excited state rotational constant of 1.1387(5) GHz. The transition frequency is identical to the measurement in ^{41}K^{87}Rb within the 50 MHz uncertainty we assign to our wavemeter. We also measured the difference in polarizability at larger detunings (Fig. 3.14b), finding that the magic wavelength is roughly 32 GHz detuned from the $N = 0 \leftrightarrow N' = 1$ transition. To check that the magic wavelength does not strongly depend on polarization, we repeated the measurement with the electric field of the spectroscopy light aligned (orange) and perpendicular (blue) to the magnetic field defining the quantization axis, finding a zero crossing at the same position. The differential polarizability is calculated based on the beam size as measured on a profile camera and the power measured before the cell, but may be subject to systematic errors if the beam at the position of the molecules is distorted from a Gaussian distribution of the measured size.

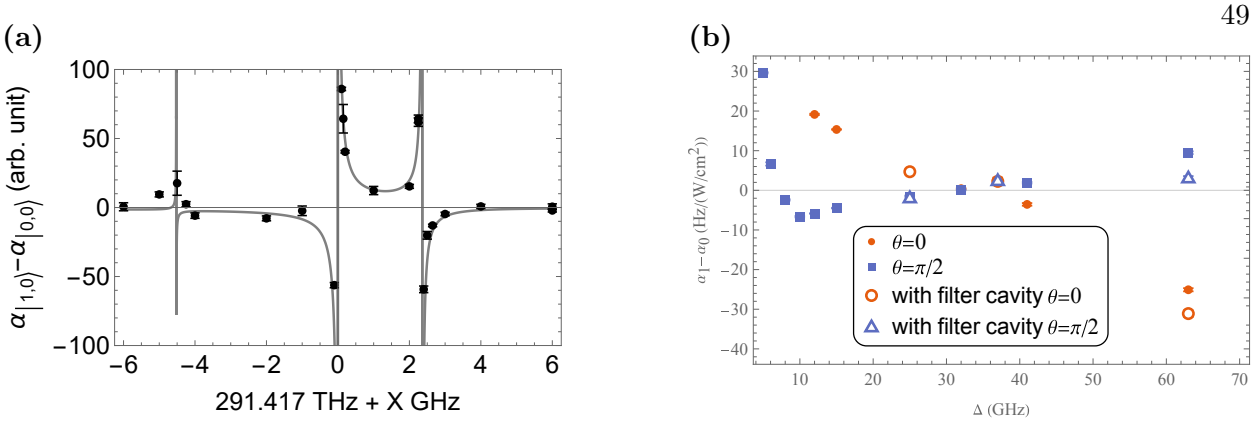

Figure 3.14: (a) The difference in polarizability between $|1\rangle$ and $|0\rangle$ is plotted as a function of detuning from the X-b transitions for small detunings. Three features are present, corresponding to the $N = 1 \leftrightarrow N' = 0$, $N = 0 \leftrightarrow N' = 1$, and $N = 1 \leftrightarrow N' = 2$ transitions from left to right. The line is a fit to a model of the polarizability, Eq. 1-2 in [153]. (b) The difference in polarizability between $|1\rangle$ and $|0\rangle$ is plotted as a function of detuning from the X-b transitions for two polarizations, $\theta = 0$ (orange) and $\theta = \pi/2$ (blue) between the light's electric field and the quantization axis provided by the magnetic field. Measurements both with (hollow points) and without (filled points) the filter cavity are shown, indicating similar zero crossings in both conditions. Both polarizations cross zero at a detuning of around 32 GHz, indicating the magic wavelength. The y-axis is calibrated based on the measured beam size and power.

Scattering of the trap light can cause heating and loss of the molecules. Because the magic wavelength is near the band of X-b transitions, we would expect the imaginary polarizability to be higher than the farther-detuned 1064 nm used for our other optical traps. In particular, we expect both scattering from the $v = 0$ X-b transition, which we can model as a two-level system, and from other states, which we assume to contribute a constant imaginary polarizability $\mathrm{Im}\,\alpha_{\mathrm{bg}}$ in the vicinity of the magic wavelength.

We measure the imaginary polarizability by measuring the molecule lifetime as a function of laser detuning and intensity. Because the scattering rate scales as Δ^{-2}, even a small amount of light near resonance will cause rapid loss, which we saw during initial measurements. To suppress

spontaneous emission from the laser which was causing the loss, we added a Fabry-Perot filter cavity with finesse of approximately 1000 and free spectral range 72 GHz[11] . The cavity is locked to the laser with dither locking and with optimized cavity coupling, we were still able to deliver around 2 mW to the molecules. At the magic detuning of 32 GHz, the intensity of light on resonance is suppressed by a factor of 2.5×10^{-6} by the cavity, which was sufficient for our lifetime measurements.

During the measurement, a deeper 3D lattice suppresses tunneling and collisional loss, but off-resonant scattering of the 1064 nm lattice light can limit molecule lifetime [100]. To balance the two loss processes and provide the longest overall lifetime, the lattice depth was set to 25 Er, giving a lifetime of 24(2) s, determined by fit to a one-body loss model. We subtract the loss rate due to the lattice from the measured loss rates with the X-b laser applied.

Assuming small Δ such that scattering from the X-b transition is the dominant loss process, the scattering rate is given in [153] as

$$\gamma_{\mathrm{sc}} = \frac{3\pi c^2}{2\hbar\omega_0^3}\frac{\Gamma\Gamma_e}{\Delta^2}I \tag{3.12}$$

where Γ_e is the decay rate from the excited state and $\Gamma = \Gamma_e F$ where F is the Franck-Condon factor between the ground and excited states. The measured loss rates are shown in Fig. 3.15, along with a fit to Eq. 3.12 (black). From the fit, taking $F = 0.9474$ [157], we extract $\Gamma_e = 2.77(4)$ kHz. This is narrower than the 4.9 kHz linewidth measured for $^{41}\mathrm{K}^{87}\mathrm{Rb}$ [157]. Although it is possible that this is a real difference, it is more likely due to imperfect calibration of the intensity.

[11] The cavity was adapted from a Thorlabs SA210-8B Fabry-Perot interferometer by shortening the cavity spacer to increase the FSR. We used a Liquid Instruments Moku:Go for the dither lock.

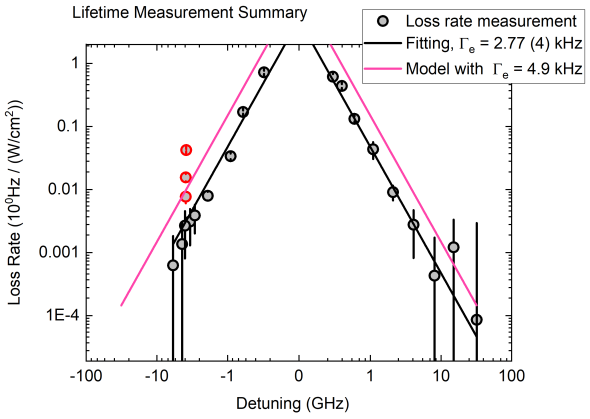

Figure 3.15: The intensity-normalized scattering rate is plotted as a function of detuning from the X-b transition. A fit to Eq. 3.12 (black), along with the expected loss rate if the linewidth matched ^{41}K^{87}Rb [157] (pink) are plotted. The points shown in red, which possibly come from leakage through another cavity mode or coupling to another molecular state, are excluded from the fit.

Based on these measurements, we can analyze prospects for optical trapping at the magic wavelength. For a 40 E_r 3D lattice, in which tunneling would be strongly suppressed, the one-body lifetime at the magic wavelength of +32 GHz would be 1.2 s, assuming the scattering from the X-b transition dominates over background imaginary polarizability and taking the 4.9 kHz linewidth from [157]. While sufficient for the timescales of spin physics that we have so far explored, the lifetimes may be too short for efficient evaporative cooling of the molecules ([99] and Sec. 6.2.3) in the magic wavelength trap, so both 1064 and 1028 nm lasers systems might be required. In addition, either a high-finesse, high-power filter cavity or a laser source with intrinsically low amplified spontaneous emission[12] would be required to suppress near-resonant light which could otherwise cause much faster loss. In light of the lifetime limitations, the success of dynamical decoupling (Sec. 3.2.1) at extending coherence, and the technical complexity of adding a new high-power laser system, we decided not to immediately implement a magic wavelength trap on the KRb experiment. With an appropriate design, it may be an interesting future direction.

[12] Vertical-external-cavity surface-emitting-lasers (VECSEL) from Vexlum, as used by the Cornish group's RbCs experiment, may be promising for this approach.

Chapter 4

Mean-field spin dynamics with itinerant molecules

"Well, shake it up, baby, now

Twist and shout (Twist and shout)"

Twist and Shout – The Beatles

Generalizations of the Heisenberg model (Eq. 1.3) include XYZ spin models of the form

$$H_{XYZ} = \sum_{i<j} J_{ij} \left(g_x s_i^X s_j^X + g_y s_i^Y s_j^Y + g_z s_i^Z s_j^Z \right) \tag{4.1}$$

describe fundamental phenomena in magnetism. In particular, the XXZ model with $g_x = g_y = g_\perp$,

$$H_{XXZ} = \sum_{i<j} J_{ij} \left(g_\perp \left(s_i^X s_j^X + s_i^Y s_j^Y \right) + g_z s_i^Z s_j^Z \right) \tag{4.2}$$

generalizes the XY ($g_z = 0$), XXX ($g_z = g_\perp$), and Ising ($g_\perp = 0$) Hamiltonians. Here, the coefficients J_{ij} encode the coupling between different particles indexed by i and j. These models can be simulated with superexchange of atoms in an optical lattice with contact interactions ([158] and Sec. 1.2). Optical cavities can mediate all-to-all interactions between atoms, allowing study of highly collective dynamics [159]. Disordered couplings can lead to spin glass phases [160], which have recently been realized in multimode cavity QED systems [161]. Polar molecules and other dipolar systems such as magnetic atoms [162] and nitrogen-vacancy (NV) centers in diamond [163], most naturally realize anisotropic, long-range interactions

$$J_{ij} \propto \frac{1 - 3\cos^2(\theta_{ij})}{|r_{ij}|^3}. \tag{4.3}$$

For these systems, the effective range of the interaction can be reduced by Floquet engineering [164] or allowing superexchange to dominate over dipolar interactions, or, in the case of molecules or magnetic atoms, extended by allowing itinerance. This chapter focuses on the XYZ model's dynamics in the latter case.

For deeply degenerate itinerant molecules confined in a 2D plane, J_{ij} can be approximated as a constant J. This can be derived by considering molecules occupying different eigenstates i and j of a 2D harmonic potential in which molecules can move and computing the matrix elements of the dipolar interactions $J_{ij} = \iint |\psi_i(\mathbf{r}_1)|^2 V_{\mathrm{dd}}(\mathbf{r}_1, \mathbf{r}_2) |\psi_j(\mathbf{r}_2)|^2 \, \mathrm{d}\mathbf{r}_1 \, \mathrm{d}\mathbf{r}_2$. Because of the delocalization of the wavefunctions, the matrix element depends only weakly on the values of i and j, justifying approximation with an average value J [165]. A classical intuition for the system can be gained by noting that the motion, assumed to be fast relative to the dynamics generated by H_{XXZ}, averages the interactions over different configurations of the molecules, as in motional narrowing [166]. In this limit, the Hamiltonian can be approximated as a collective spin model

$$H^c_{XXZ} = J \left(g_\perp \left(S_X^2 + S_Y^2 \right) + g_z S_Z^2 \right) + h_Z S_Z \tag{4.4}$$

where $\mathbf{S} = \sum_i \mathbf{S}_i$ and J is an average $\langle J_{ij} \rangle_{i \neq j}$ over the occupied motional modes.

For an isotropic three-dimensional system, J averages to zero, as the head-to-tail and side-to-side interactions have opposite signs and cancel each other. This can be seen by integrating Eq. 4.3 over a sphere. Therefore, a lower dimensional system is needed to see collective dynamics arising from the spin model. Experimentally, we generated 2D systems by confining molecules in one or more layers of a 1D optical lattice. In this geometry, molecules in the same layer all interact side-to-side with the same sign of interactions, since $\theta = \pi/2$ in Eq. 4.3 if the quantization axis is oriented along the lattice wave-vector (effects of changing the quantization axis direction are discussed in Sec. 4.2.1.1). Because of the large spatial extent of the other layers, collective interactions between layers are largely averaged out and only slightly affect the dynamics on the millisecond timescales considered in this chapter [105]. We can therefore approximate the system as a stack of isolated

layers, and consider the dynamics within a single layer.

In this chapter, we discuss experimental realization and characterization of collective spin models with itinerant molecules, using electric fields (Sec. 4.2 based on [117]) to realize tunable XXZ Hamiltonians and show that the interactions can be dynamically reversed by selecting different qubit states (Sec. 4.2.2). We further apply Floquet engineering (Sec. 4.3 based on [123]) to generate an XYZ Hamiltonian. In Ch. 5, we explore spin dynamics in regimes in which the collective description breaks down.

4.1 Measuring mean-field dynamics

Per the Ehrenfest theorem, the expectation values of the collective Bloch vector $\mathbf{S}$ under the all-to-all Hamiltonian Eq. 4.4 evolve as

$$\frac{\mathrm{d}\langle S_i\rangle}{\mathrm{d}t} = 2J\sum_{j,k}\epsilon_{ijk}g_j\langle S_j\rangle\langle S_j\rangle \tag{4.5}$$

where ϵ_{ijk} is the Levi-Civita symbol.

Experimentally, we can measure these dynamics using state-resolved imaging combined with global rotations of the spins on the Bloch sphere. We produce molecules in $|0\rangle$, corresponding to $\langle\mathbf{s}\rangle = \hat{Z}/2$. By applying a microwave pulse on the $|0\rangle \leftrightarrow |1\rangle$ transition with phase ϕ and area θ, we rotate the Bloch vector by θ about an axis $-\sin(\phi)\hat{X} + \cos(\phi)\hat{Y}$, preparing a state with average Bloch vector $\langle\mathbf{s}_0\rangle = \frac{1}{2}(\cos(\phi)\sin(\theta), \sin(\phi)\sin(\theta), \cos(\theta))$ (Fig. 4.1a). Time evolution transforms the Bloch vector into $\langle\mathbf{S}\rangle$. We can measure $\langle S_Z\rangle$ by imaging the molecules in $|0\rangle$ and $|1\rangle$ ([105] and Sec. 2.1.4). To measure the other components of $\langle\mathbf{S}\rangle$, we can apply an additional $\pi/2$ pulse to map S_X or S_Y onto S_Z before imaging (Fig. 4.1b). Thus, over three shots with different readout pulses, we can measure $\langle\mathbf{S}\rangle$[1] . We used this method in [123]. For the dynamics in [117], the Bloch vector remained at the same $\langle S_Z\rangle$, so we measured only S_X and S_Y by applying a readout pulse with area $\pi - \theta$ and variable phase (Fig. 4.5a and c).

[1] It should be possible to read out $\langle\mathbf{S}\rangle$ in a single shot by mapping the projection of $\mathbf{S}$ onto different Bloch sphere axes to the population in multiple internal states, then imaging each state. This has been demonstrated using trapped ions in [167].

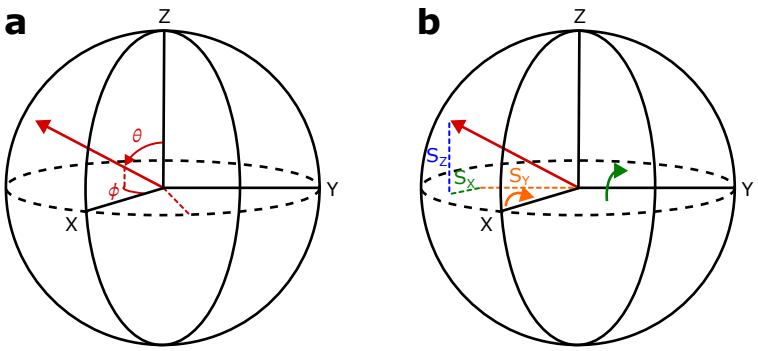

Figure 4.1: (a) An initial state **S** at polar angle θ from $\hat{Z}$ and azimuthal angle ϕ from $\hat{X}$ is prepared by a rotation of area θ about the axis $-\sin(\phi)\hat{X}+\cos(\phi)\hat{Y}$. (b) To read out the $\hat{X}$ or $\hat{Y}$ component of **S**, a $\pi/2$ rotation about the $\hat{Y}$ or $\hat{X}$ axis is applied to map the respective component onto the $\hat{Z}$ direction.

To understand systematic errors in the imaging process, in [123] we prepared a superposition $\cos(\theta)\left|0\right\rangle+\sin(\theta)\left|1\right\rangle$ for different angles θ with a microwave pulse immediately before our imaging sequence. For itinerant molecules, we find that for θ close to 0 or π, fewer molecules are in the minority state than would be expected from the state preparation. We attribute this to loss from inelastic collisions during the imaging sequence. As these collisions occur nearly 100 times more rapidly for distinguishable molecules [105], their effect on the density can be modelled as $\frac{\mathrm{d}N_i}{\mathrm{d}t}=-\beta_p N_i N_j$ for $i\neq j$ in which the indices are over the states $\left|0\right\rangle$ and $\left|1\right\rangle$ and β_p is the p-wave loss rate. By fitting the solution to this system of differential equations to the measured molecule numbers, we are able to correct measured N and $\langle S\rangle$ for this loss (Fig. 4.2).

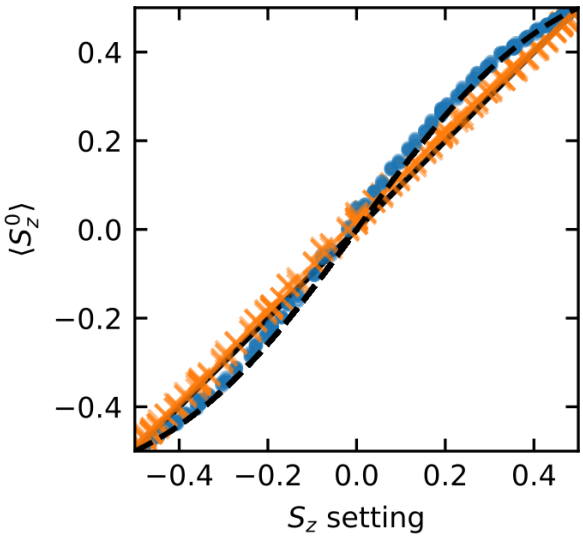

Figure 4.2: **Correcting imaging for loss.** The measured value of $\langle S_Z^0 \rangle$ is plotted (blue circles) as a function of the value prepared by a microwave pulse. The dashed curve is a fit to the loss model. By inverting the model, the data can be corrected for loss during imaging (orange crosses).

4.2 XXZ dynamics: one-axis twisting

Noting that $\mathbf{S} \cdot \mathbf{S} = S_X^2 + S_Y^2 + S_Z^2$, the all-to-all XXZ Hamiltonian (Eq. 4.4) can be rewritten

$$H_{XXZ}^c = J_\perp \mathbf{S} \cdot \mathbf{S} + \chi S_Z^2 + h^Z S_Z \tag{4.6}$$

. where $J_\perp = J g_\perp$ and $\chi = J(g_z - g_\perp)$. Under the $\mathbf{S} \cdot \mathbf{S}$ term, any state with the same Bloch vector length has the same energy, independent of its orientation. As such, the term does not cause rotation of the Bloch vector, but protects the spins against dephasing by opening an energy gap between states where N and $N-1$ spins are aligned [168]. The h_Z term, which can come from both detunings between the probe field and transition frequency due to technical noise, as well as an effective magnetic field generated by the spins, causes a global rotation about the Z axis of the Bloch sphere. Its effect can be cancelled by a spin-echo pulse sequence [130]. We focus on measuring the effect of the χ term, which, under the mean-field approximation, is $\chi \langle S_z \rangle S_z$. This

causes $\mathbf{S}$ to rotate about the Z axis at a rate proportional to $\langle S_z \rangle$. Beyond mean-field effects, this term should also generate entanglement between the spins, allowing preparation of metrologically useful spin-squeezed states by one-axis twisting (OAT) [169]. This is discussed in detail in Ch. 7.

In [117], upon which this section is largely based, we measured χ using Ramsey spectroscopy [170] . To do so (Fig. 4.5a), we initialized the spins in the state $\cos(\theta/2)\,|\downarrow\rangle + \sin(\theta/2)\,|\uparrow\rangle$ with a pulse of area θ. We then allowed the system to evolve for $T = 1.2$ ms while applying dynamical decoupling, consisting of an XY8 pulse sequence [134] repeated three times. Finally, we applied another pulse of area $\pi - \theta$ with variable phase ϕ before measuring S_z with state-resolved imaging. The Ramsey fringes (Fig. 4.5c) exhibit phase shifts proportional to $\langle S_z \rangle$ (Fig. 4.5d), with constant of proportionality U_χ. To confirm that the phase shifts arise from interactions, we measured U_χ as a function of molecular density, finding a linear relationship (Fig. 4.5e), extracting χ as U_χ/n.

We have experimental access to several parameters to control the interaction strength χ_0. By changing the strength of an applied electric field, the values of g_z and $g_\perp$ can be varied and by controlling its orientation, the orientation-averaged value of J can be tuned (Sec. 4.2.1). By selecting different internal states as the spin-1/2 system, the sign of the interaction can be reversed (Sec. 4.2.2).

4.2.1 Electric field tuning

At zero electric field, the molecules have negligible lab-frame dipole moment, so interact through spin-exchange with rate $d_{\downarrow\uparrow} d_{\uparrow\downarrow}$. A d.c. electric field mixes the eigenstates of the bare molecular Hamiltonian (Sec. 3.1). This has two relevant effects: a dipole moment $d_\uparrow$ or $d_\downarrow$ in the lab frame is induced, and the spin-exchange interaction $d_{\uparrow\downarrow}$ is suppressed. A theoretical calculation, neglecting hyperfine structure, of interaction strengths of the states $|\downarrow\rangle = |0,0\rangle$ and $|\uparrow\rangle = |1,0\rangle$ is plotted as a function of electric field in Fig. 4.3c. The coefficients in the XXZ Hamiltonian (Eq. 4.2) can be written in terms of the dipole moments as $g_\perp = 2 d_{\downarrow\uparrow} d_{\uparrow\downarrow}$ and $g_Z = (d_\downarrow - d_\uparrow)^2$. Their difference, $\chi_0 = g_Z - g_\perp$, which is proportional to the expected rate of OAT, is plotted as a black line in Fig. 4.3c.

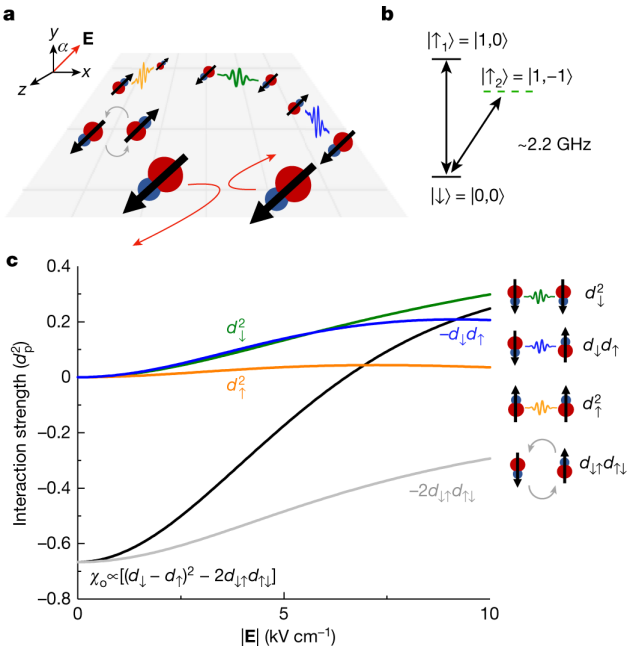

Figure 4.3: **A 2D itinerant spin system with polar molecules.** **a**, Molecular spins are free to move within a 2D layer. Their dipolar interactions are tuned by a bias electric field **E** with configurable magnitude and orientation in the $x-y$ plane. Yellow, blue, green and gray curves illustrate interaction processes detailed in **c**. Red arrows represent dipolar elastic collisions. **b**, Energy diagram for the ground and first excited rotational states in which we encode the spin-1/2 degree of freedom. The transitions are driven by microwaves. **c**, Calculated dipolar interaction strength as a function of $|\mathbf{E}|$ for the spin manifold $\{|\downarrow\rangle, |\uparrow_1\rangle\}$. The dipolar coupling strength is given in units of the permanent dipole moment of KRb $d_\mathrm{p} = 0.574$ Debye. The molecules interact through their induced dipole moments $d_\downarrow$ and $d_\uparrow$, as well as the transition dipole moment $d_{\downarrow\uparrow}$. The black line shows the field dependence of χ_0.

We measured χ, as described in Sec. 4.2, for several electric fields between 0 and 8.96 kV/cm (Fig. 4.5f). The data followed the calculated scaling of χ with electric field, starting large and negative with the zero field spin-exchange interactions, then crossing zero as the field was increased beyond 6.5 kV/cm. At 6.5 kV/cm, the so-called Heisenberg point, g_z and $g_\perp$ are of equal magnitude, realizing a Heisenberg XXX Hamiltonian. The calculated values of χ_0, where the overall scale is fit

to the data to account for the geometric component of the interactions, are plotted as a black line. For fields below 500 V/cm (gray shaded region), couplings between the nuclear spins and rotation can substantially modify the transition dipole moment, thus χ from the values shown in Fig. 4.3c.

4.2.1.1 Tuning with electric field direction

The orientation of the electric field can also be varied. If $\mathbf{E}$ is tilted at angle α with respect to the lattice wavevector in the $x-y$ plane (inset in Fig. 4.5g), the average geometric factor of the dipolar interaction for a 2D system can be tuned. We can estimate this factor for molecules confined to an isotropic 2D geometry, taking molecule i fixed at the origin and molecule j at azimuthal angle β from the $\hat{x}$ axis (Fig. 4.4). The angle between $\mathbf{r}_{ij}$ and $\mathbf{E}$ satisfies $\cos^2(\Theta_{ij}) = \sin^2(\alpha)\cos^2(\beta)$. Averaging over β gives $\langle\cos^2(\beta)\rangle = 1/2$, such that the average geometric factor in the collective XXZ Hamiltonian (Eq. 4.6) becomes

$$J(\alpha) = \langle 1 - 3\cos^2(\theta_{ij})\rangle = (3\cos^2(\alpha) - 1)/2 \tag{4.7}$$

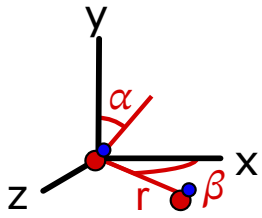

Figure 4.4: The coordinate system for interactions between molecules in a tilted electric field.

In Fig. 4.5g, the measured value of χ is plotted as a function of α for $|\mathbf{E}| = 1$ kV/cm, showing that the magnitude and sign of χ can be varied. The data are fit with a scaled version of Eq. 4.7, showing excellent agreement. The ability to tune the electric field angle for 2D or layered dipolar systems is relevant to realizing magic-angle optical traps for reducing single-particle decoherence (Sec. 3.3.2) or observing pairing and superfluidity [171, 172, 173] or Fermi surface deformation [174] in a spin-polarized gas.

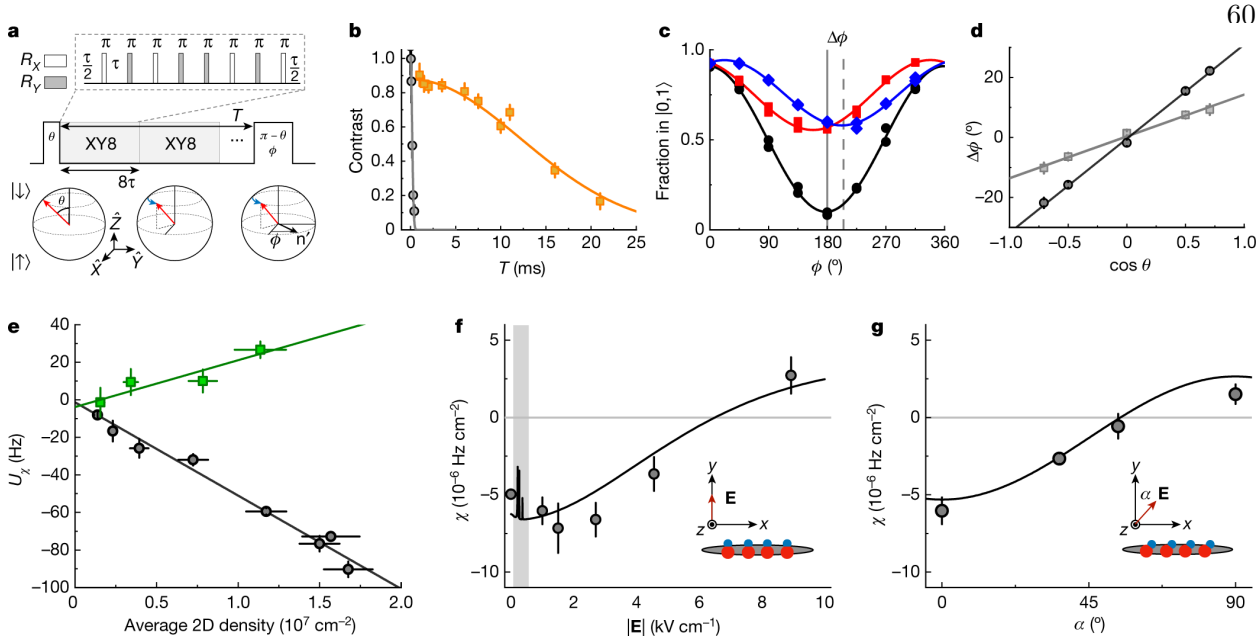
a
b
c
d
e
f
g
Contrast
T (ms)
Fraction in |0,1⟩
Δφ
φ (°)
Δφ (°)
cos θ
XY8
XY8
8τ
Average 2D density (10^7 cm^−2)
U_χ (Hz)
χ (10^−6 Hz cm^−2)
|E| (kV cm^−1)
α (°)
E

Figure 4.5: **Dynamical decoupling and tunable dipolar interactions between molecules.** **a**, The standard Ramsey sequence consists of an initial pulse of area θ, followed by an evolution time T, and finally a pulse of area $\pi - \theta$ about an axis $\hat{n} = \hat{X}\cos(\phi) + \hat{Y}\sin(\phi)$. We insert one or more XY8 sequences during T, denoted as XY8 XY8 $\times M$. One XY8 sequence (zoomed region) consists of eight Rabi-π pulses spaced by time τ, for a total free precession time of 8τ. **b**, Decay of Ramsey fringe contrast between $|\downarrow\rangle$ and $|\uparrow_1\rangle$ without dynamical decoupling (gray circles) and with XY8 $\times$ 3 at a density of $n = 0.14(2) \times 10^7\text{cm}^{-2}$ (orange squares). We use a low density to reduce interaction effects. Error bars are 1 s.d. from bootstrapping. **c**, Measured Ramsey fringes with dynamical decoupling for an average 2D density $n = 1.4(1) \times 10^7\text{cm}^{-2}$ for initial population imbalance $\theta = \pi/4$ (blue diamonds), $\pi/2$ (black circles) and $3\pi/4$ (red squares) for $T = 1.2$ ms at $|\mathbf{E}| = 0$. Solid lines are fits to $A\cos\left((\pi/180)\phi - \Delta\phi\right)$ plus an offset, from which we extract the measured shift $\Delta\phi$. **d**, Measured $\Delta\phi$ versus $\cos(\theta)$ for $n = 1.4(1) \times 10^7\text{cm}^{-2}$ (black circles) and $0.65(7) \times 10^7\text{cm}^{-2}$ (gray squares). The strength of the mean-field interaction U_χ is extracted from the slope of the linear fit (solid lines). Error bars are 1 s.e. from fits. **e**, Density dependence of U_χ for the $\{|\downarrow\rangle, |\uparrow_1\rangle\}$ manifold (gray) and the $\{|\downarrow\rangle, |\uparrow_2\rangle\}$ manifold (green). Black and green solid lines are linear fits to the data. The slopes of the fits are direct measurements of χ_1 and χ_2, respectively. Error bars are 1 s.e. from linear fits. **f**, Dependence of χ for the $\{|\downarrow\rangle, |\uparrow_1\rangle\}$ manifold on $|\mathbf{E}|$ at $\alpha = 0°$. The solid line is a one parameter fit to $A\left((d_\downarrow - d_\uparrow)^2 - 2d_{\downarrow\uparrow}d_{\uparrow\downarrow}\right)$ calculated for KRb at the experimental magnetic field and trapping conditions, which includes modifications to the dipole moments from the mixing of hyperfine and rotational states at $|\mathbf{E}|$ below roughly 500 V cm^{-1} (shaded area). Gray line indicates zero. Error bars are 1 s.e. from linear fits. **g**, Angular dependence of χ for the $\{|\downarrow\rangle, |\uparrow_1\rangle\}$ manifold at $|\mathbf{E}| = 1.02$ kV cm^{-1}. Solid line is a one parameter fit to $-A(3\cos^2(\alpha) - 1)$. Gray line indicates zero. Error bars are 1 s.e. from linear fits.

4.2.2 Tuning with internal state

Different sets of states have different dipole moments, thus different values of $J_\perp$ and J_Z. Microwaves can rapidly and coherently transfer the population between different levels [97], enabling

dynamic control. For instance, the transition dipole moment between $|0,0\rangle$ and $|2,0\rangle$ is zero for $|\mathbf{E}| = 0$. This pair of states was used by our group in [105] to switch off spin-exchange between lattice layers and in RbCs in [154] to eliminate interaction-induced dephasing, allowing observation of second-scale rotational coherence times. Rapidly turning interactions on and off can also be used to implement quantum gates [144] or study quench dynamics [175]. By picking a pair of states with the opposite sign of $J_\perp$, the interactions to be reversed. At $|\mathbf{E}| = 0$, the interactions in the $|0,0\rangle$ and $|1,\pm1\rangle$ manifold are spin-exchange, but with opposite sign as between $|0,0\rangle$ and $|1,0\rangle$, namely

$$J_\perp^{|0,0\rangle\leftrightarrow|1,\pm1\rangle} = -1/2 J_\perp^{|0,0\rangle\leftrightarrow|1,0\rangle} \tag{4.8}$$

The ability to evolve the system under a forward, then reversed, Hamiltonian, known as a Loschmidt echo [176], is valuable for both many-body physics and metrology. In many-body physics, it enables the study of out-of-time-ordered correlators [177], measuring the scrambling of quantum information. For metrology, reversal of interactions can enable amplification of a signal of interest, leading to entanglement-enhanced metrology with relaxed detection requirements relative to spin squeezing [165, 178, 179, 180].

We can address both $|1,0\rangle$ and $|1,-1\rangle$, which are split by around 400 kHz by coupling between the nuclear spins and molecular rotations [84], by changing the microwave frequency. In Ref. [117], using the Ramsey spectroscopy procedure described in Sec. 4.2, we measured χ in both the $|0,0\rangle \leftrightarrow |1,0\rangle$ and $|0,0\rangle \leftrightarrow |1,-1\rangle$ manifolds (black circles and green squares in Fig. 4.5e, respectively), finding $\chi_{|0,0\rangle\leftrightarrow|1,0\rangle} = -4.9(3)\times10^{-6}$ Hz cm^2 and $\chi_{|0,0\rangle\leftrightarrow|1,\pm1\rangle} = 2.3(8)\times10^{-6}$ Hz cm^2. These interactions differ by a factor of roughly minus two, as expected (Eq. 4.8).

Building upon this control, we also demonstrated coherent reversal of the spin Hamiltonian by switching the population in $|1,0\rangle$ to $|0,0\rangle$ in the middle of a Ramsey sequence (Fig. 4.6a). After preparing molecules in a superposition of $|0,0\rangle$ and $|1,-1\rangle$ with a pulse of area $\theta = \pi/4$ or $3\pi/4$, we allowed the system to evolve for a variable time T_s of up to 1.2 ms while suppressing dephasing with XY8 dynamical decoupling. After T_s, we applied a composite pulse of duration 70 μs consisting of

three π pulses to transfer the population in $|1,-1\rangle$ to $|1,0\rangle$. We then allowed the system to evolve for an additional time $T - T_s$ before applying a readout pulse of area $\pi - \theta$ and variable phase ϕ and imaging the molecules in $|0,0\rangle$ and $|1,0\rangle$. By repeating the measurement for different angles ϕ, we can fit the phase of the resulting Ramsey fringes, $\Delta_\phi(\theta = \pi/4)$ and $\Delta_\phi(\theta = 3\pi/4)$. To make the measurement sensitive to interactions while cancelling common phase shifts originating when the state is switched, we extract the phase difference $\Delta\phi = \Delta_\phi(\theta = \pi/4) - \Delta_\phi(3\theta = \pi/4)$. In Fig. 4.6b, we plot $\Delta\phi$ as a function of $T = T_1 + T_2$. For T less than 1.2 ms, we fix a short $T - T_s = 80\,\mu$s and scan T_s (green squares). For longer T, we fix $T_s = 1.2$ ms. There, the phase accumulation in the second phase is reversed, with slope approximately twice the slope in the first phase (gray circles). At $T = 1.6$ ms, $\Delta\phi$ returns to the original value.

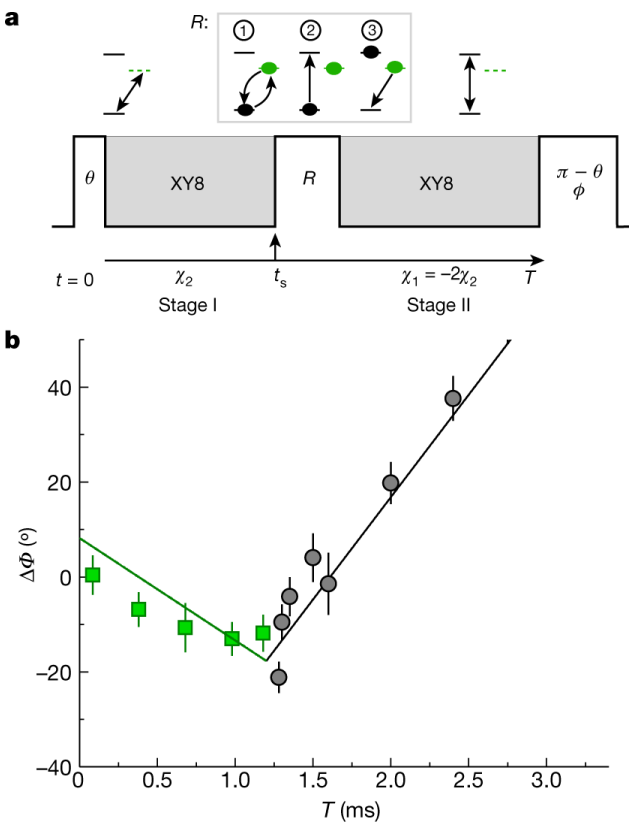

Figure 4.6: **Reversal of the spin dynamics.** **a**, Measurement sequence. Molecules are initially prepared and allowed to evolve in a superposition of $|\downarrow\rangle$ and $|\uparrow_2\rangle$. A composite pulse R coherently transfers the population in $|\uparrow_2\rangle$ to $|\uparrow_1\rangle$ while preserving its relative phase to $|\downarrow\rangle$. Molecules then evolve in $\{|\downarrow\rangle, |\uparrow_1\rangle\}$. Inset shows the composition of R. **b**, Measured time evolution of $\Delta\Phi = \Delta\phi(\theta = \pi/4) - \Delta\phi(\theta = 3\pi/4)$ at $n = 1.1(1) \times 10^7 \mathrm{cm}^{-2}$. The phase accumulation in stage I (green squares) and stage II (black circles) are plotted over time. For $T < 1.2$ ms, we fix the duration of stage II to be $80\,\mu$s and scan the time of stage I. For $T > 1.2$ ms, we fix the duration of stage I to be 1.2 ms and scan the time of stage II. The total time plotted excludes the widths of the microwave pulses. A piecewise linear fit to the time evolution of $\Delta\Phi$ is shown as a solid line. The ratio between the two slopes is constrained to -2. Error bars are 1 s.e. from fits.

Interesting near-term experiments with the KRb apparatus are enabled by the demonstrated Hamiltonian reversal. The degree of coupling between the interacting spins and molecular motion

can be characterized using Loschmidt echos, which reverse the spin Hamiltonian but leave the motion unaffected. This was explored using freely moving Rydberg atoms in Ref. [181], which also demonstrated time reversal of Floquet-engineered XXZ models. Our additional control over motion with optical lattices (see Ch. 5) should allow study of different regimes. In addition, it would be interesting to explore amplification of phase accumulated in a Ramsey spectroscopy experiment, as demonstrated in a cavity QED system in [179] and with an ensemble of NV centers in [180].

4.3 XYZ dynamics: two-axis twisting

In addition to d.c. fields, the interactions between molecules can be tuned by sequences of microwave pulses. This process is an example of Floquet engineering, in which periodic driving of a quantum system can be used to modify its dynamics. With an appropriate pulse sequence, the native low-field XY interactions can be transformed into a range of XXZ or XYZ Hamiltonians. Although this method had already been demonstrated in dipolar spin systems, including Rydberg atoms [182], NV centers [183], and polar molecules [147], we applied it in two novel directions. First, we designed, implemented, and characterized a Floquet pulse sequence for generating two-axis twisting using an XYZ Hamiltonian using itinerant molecules, building off our previous work characterizing XXZ Hamiltonians. This project is discussed in the following sections. In addition, as described in Sec. 5.5, we systematically compared the long-time dynamics of Floquet-engineered and d.c. field-tuned XXZ Hamiltonians in order to explore Floquet engineering's efficacy and limitations.

Our results on Floquet-engineered spin dynamics with polar molecules are published in [123], upon which this section is based.

4.3.1 Floquet engineered spin models

The dynamics of a quantum system under periodic driving can be described with a Magnus expansion [130]. Its leading order for small t_c/T, in which t_c is the period of the cycle and T is the characteristic timescale of interactions, is average Hamiltonian theory [184]. Under average Hamiltonian theory, the system evolves under the interaction picture Hamiltonian $H_{\text{avg}} = \frac{1}{t_c}\int_0^{t_c} H(t)\,\mathrm{d}t$,

in which $H(t) = H(t - t_c)$ is the periodic Hamiltonian. If H consists of periods of free evolution separated by rapid changes of the Hamiltonian, $H_{\text{avg}} = \frac{1}{t_c}\sum_i \tau_i H_i$, in which τ_i is the free evolution time under Hamiltonian H_i in each cycle. In our experiment, this can be realized by applying rapid microwave pulses that rotate each spin by an angle θ about an axis $\hat{n}$ on the Bloch sphere (Sec. 3.2).

At low electric field, the molecules interact with an XY Hamiltonian, $g_X = g_Y = g_\perp$ and $g_Z = 0$. If the state on the Bloch sphere is rotated by a $-\pi/2$ pulse about the $\hat{Y}$ axis, the original $\hat{X}$ axis now points along the $\hat{Z}$ direction (Fig. 4.7b). In the reference frame that rotates with the original $\hat{Z}$ axis, known as the toggling frame, the interactions have been transformed to $g_Y = g_Z = g_\perp$ and $g_X = 0$. If another $-\pi/2$ pulse is applied about the $\hat{X}$ axis, the toggling frame $\hat{Y}$ axis points along the $\hat{Z}$ direction, leading to interactions $g_X = g_Z = g_\perp$ and $g_Y = 0$. By varying the ratio of times spent in each orientation, the average Hamiltonian can be tuned over the range of XYZ Hamiltonians with constant trace $g_X + g_Y + g_Z = 2g_\perp$ and with $g_{X,Y,Z} > 0$ (Fig. 4.7c).

With an appropriate pulse sequence, the tuning of interactions can be combined with cancellation of disorder. If each toggling frame axis spends equal time pointing along the $\pm\hat{Z}$ directions, precession from detuning is cancelled, as in a spin-echo pulse sequence. Additionally, if spins are rotated clockwise and counterclockwise an equal amount about each axis, the pulse sequence is robust to lowest order to errors in pulse area. A convenient algebraic formalism for evaluating and designing pulse sequence is presented in [119]. Methods also exist for designing pulse sequences robust to errors, finite repetition frequency, and finite pulse time at higher order [185].

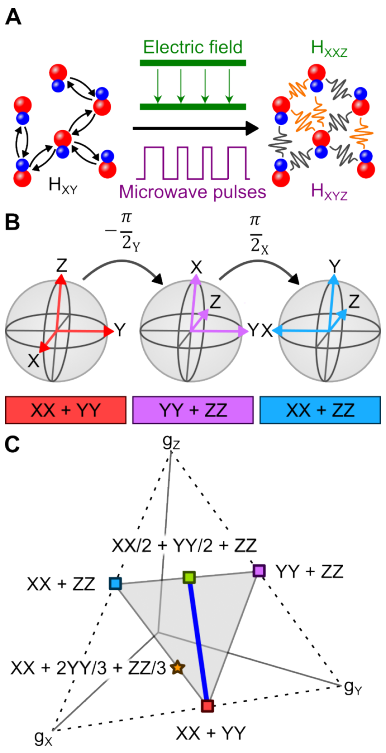

Figure 4.7: **XXZ and XYZ Hamiltonian engineering.** **A**, At low electric fields, molecules interact through spin exchange. XXZ and XYZ models can be realized with d.c. electric fields (green) and microwave pulse sequences (purple), respectively. **B**, Microwave $\pi/2$ pulses rotate the spins on the interaction picture Bloch sphere, transforming the spin-exchange XX + YY interactions into XX + ZZ or YY + ZZ interactions. **C**, A range of XXZ (blue line) and XYZ (shaded triangle) interaction Hamiltonians can be realized by controlling the amount of time the spins spend in each frame, starting with the low-electric-field spin-exchange Hamiltonian between the $|0\rangle$ and $|1\rangle$ states. The orange star indicates the Hamiltonian used to study TAT dynamics. The axes represent the strength of the couplings in the XYZ Hamiltonian.

This method presents an alternative to d.c. electric fields for realizing XXZ Hamiltonians with coefficients between $(g_{X,Y}, g_Z) = (g_\perp, 0)$ and $(g_\perp/2, g_\perp)$. In Sec. 5.5, I discuss a comparison of the Ramsey contrast decay dynamics of Floquet engineered and electric field-tuned Hamiltonians. In addition, less symmetric XYZ models can be engineered. In the next section, I discuss one such model that generates two-axis twisting dynamics, which can be applied to efficient spin squeezing.

4.3.2 Two-axis twisting

Time evolution under the all-to-all XYZ Hamiltonian $g_X = -g_Z$ and $g_Y = 0$ generates two-axis (counter)twisting (TAT) [169]. TAT can prepare spin-squeezed states from initial coherent states at the $\pm\hat{Y}$ poles of the Bloch sphere by compressing and extending the quasiprobability distribution in orthogonal directions rotated by $\pi/4$ radians relative to the twisting axes (Fig. 4.10a). For the optimal evolution time, the standard deviation of the projection of the spin in the squeezed direction scales as $1/N$, where N is the number of spins. This scaling saturates the Heisenberg limit for the minimum noise that can be achieved for sensing with N spins [186]. As such, TAT is an appealing process to generate entangled states for sensing or precision measurement on a variety of platforms, including polar molecules [29, 33].

XYZ Hamiltonians that generate TAT are not native to common platforms and can be challenging to realize. Mean-field TAT dynamics were only recently observed in a cavity QED system [187] using four-photon couplings between atoms. Following [188], we demonstrated an alternative approach to generating TAT via Floquet engineering. Subsequently, Floquet engineering has also been used to generate TAT in a two-dimensional ensemble of NV centers [180].

Because Floquet engineering preserves the trace $g_x + g_y + g_z$, it is impossible to tune the coefficients to $g_X = -g_Z$ and $g_Y = 0$. However, it is possible to create the Hamiltonian H_{TAT} with $\mathbf{g} = (g_\perp, 2g_\perp/3, g_\perp/3)$, which is the two-axis twisting Hamiltonian plus $2g_\perp/3\mathbf{S}\cdot\mathbf{S}$. Because any point on the surface of the Bloch sphere is an eigenstate of $\mathbf{S}\cdot\mathbf{S}$, this term does not affect the dynamics at short time. To do so, we used a modified XY8 pulse sequence [134], which we called XY8-TAT, in which each π pulse about the $\hat{Y}$ axis is split into a pair of $\pi/2$ pulses (Fig. 4.8). For pulse spacing τ, this results in 4τ being spent with XX + ZZ interactions and 8τ with XX + YY interactions, realizing H_{TAT} on average. Because each axis of the toggling frame spends equal time oriented in the $\pm\hat{Z}$ directions, XY8-TAT contains a series of spin-echos, thus is insensitive to static disorder. Because the pulses are about the same axes as XY8, it shares XY8's robustness to errors in pulse area or detuning [134, 119].

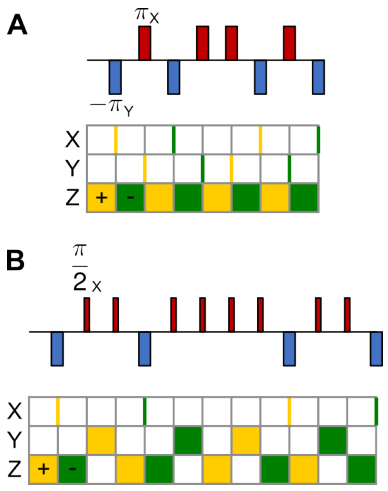

Figure 4.8: **XY8 and XY8-TAT pulse sequences.** Pulse sequences for generating OAT (XY8; **A**) and TAT (XY8-TAT; **B**) dynamics are shown using the notation of ref. [119]. Narrow (wide) rectangles represent $\pi/2$ (π) pulses, red (blue) rectangles pulses about the $\pm X$ ($\pm Y$) axes, and pulses above (below) the line about the + (-) axes. The frame matrix representation shows which axis points along the +Z direction as a function of time, with yellow (green) blocks representing axes originally along the + (-) directions.

To characterize the dynamics under H_{TAT}, we first prepared the spins with an initial Bloch vector $\langle \mathbf{S}_0 \rangle$ with a microwave pulse. We then repeated XY8-TAT for 2.4 ms before measuring the collective Bloch vector in the X, Y or Z bases (Sec. 4.1). To validate our procedure, we also repeated the same sequence but with a standard XY8 pulse sequence instead of XY8-TAT, which we previously measured (Sec. 4.2) to generate OAT.

Data from repeating this measurement for a range of $\langle \mathbf{S}_0 \rangle$ spanning the surface of the Bloch sphere is presented in Fig. 4.9. OAT has two stable fixed points at the $\pm Z$ poles of the Bloch sphere. Between the poles, interactions rotate the Bloch vector about the $\hat{Z}$ axis (Fig. 4.9a). As discussed in Sec. 4.2 and [117], the phase shift $\Delta\phi = \arctan\left(\frac{\langle S_Y \rangle}{\langle S_X \rangle}\right) - \arctan\left(\frac{\langle S_Y^0 \rangle}{\langle S_X^0 \rangle}\right)$ under OAT is proportional to $\langle S_Z^0 \rangle$ (Fig. 4.9c). We also see that $\langle S_Z \rangle$ does not depend on ϕ (Fig. 4.9e). By contrast, TAT has two unstable fixed points at the $\pm\hat{Y}$ poles of the Bloch sphere and four stable fixed points at the $\pm\hat{X}$ and $\pm\hat{Z}$ poles[189, 190]. Between the fixed points, the Bloch vector

moves alternately upwards and downwards as a function of angle in the X–Z plane, completing two oscillations around the circumference of the sphere (Fig. 4.9b). This behavior is apparent in our data (Fig. 4.9f).

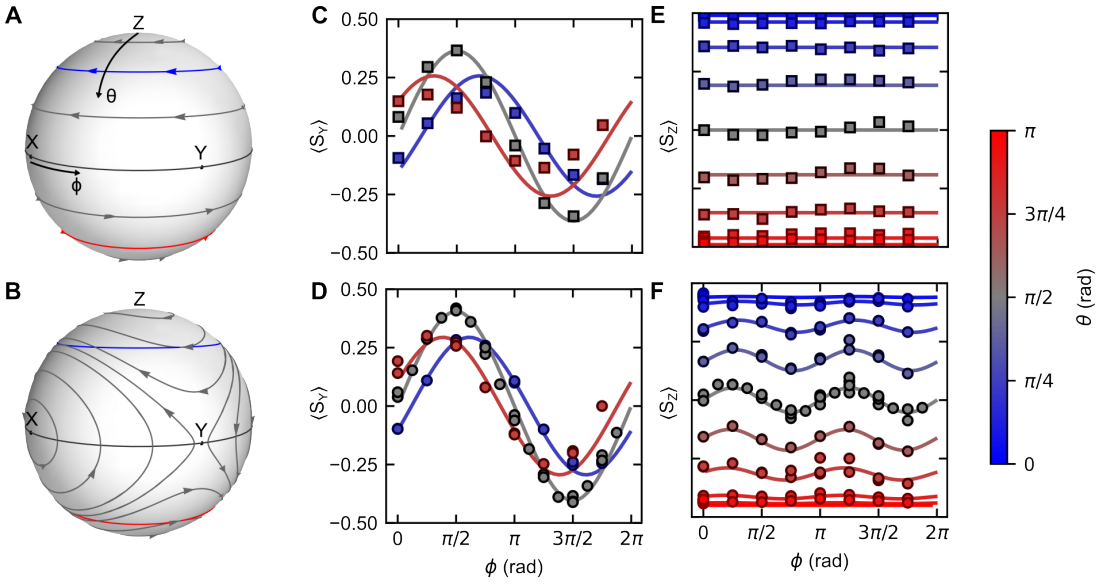

Figure 4.9: **Engineering OAT and TAT. A**, **B**, The Bloch vector phase portraits for OAT (**a**) and TAT (**B**) on the Bloch sphere. The blue, dark gray and red latitudinal lines mark $\theta = \pi/4, \pi/2, 3\pi/4$ respectively. **C**-**F**, The projection of the average Bloch vector in the Y (**C**, **D**) and Z (**E**, **F**) directions for OAT (**C**, **E**) and TAT (**D**, **F**) as a function of the phase (x-axis) and tipping angle (color) of the initial state after 2.4 ms evolution. The points are experimental data, and the solid lines are results from a mean-field simulation.

We compare our measurements to predictions from the collective mean-field model Eq. 4.5, shown as lines in (Fig. 4.9). To account for collisional dephasing (Sec. 5.3) with rate $\gamma_\perp$ we add a term $-\gamma_\perp \langle S_i \rangle$ to the equations for $\frac{\mathrm{d}\langle S_x \rangle}{\mathrm{d}t}$ and $\frac{\mathrm{d}\langle S_y \rangle}{\mathrm{d}t}$. We numerically solve the equations of motion to obtain final values for $\langle \mathbf{S} \rangle$. For OAT, $\mathbf{g} = (g, g, 0)$and for TAT, $\mathbf{g} = (3g, 2g, g)/3$ under average Hamiltonian theory. When $\gamma_\perp$ is set to zero, we observe excellent agreement between simulations using the average Hamiltonian theory interaction strengths and simulations of applying

the XY8-TAT pulse sequence with XY interactions. To properly simulate the dephasing, which is partially transformed into depolarization by the Floquet pulse sequence, we chose to model the TAT dynamics by modelling the application of the XY8-TAT pulse sequence with instantaneous pulses and XY interactions between pulses. We fitted the output of our simulations to the OAT and TAT data to find the values of g and $\gamma_\perp$. To ensure that the fit is not dominated by points with abnormal molecule number, we included only measurements for which the number is within two standard deviations of the average number for the TAT data. We found that the sum of squares of the errors was minimized when $g = 360$ s^{-1} and $\gamma_\perp = 130$ s^{-1} for our typical molecule density of $1.08(9) \times 10^7$ cm^{-2}.

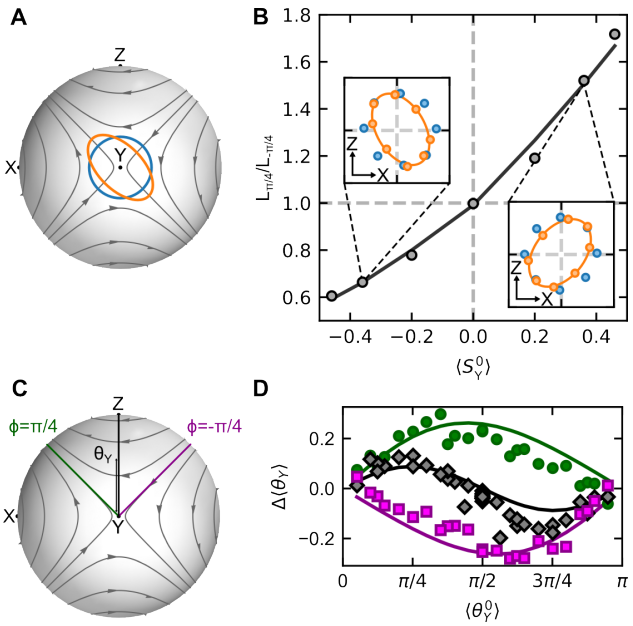

Figure 4.10: **TAT mean-field dynamics.** **A**, TAT mean-field dynamics plotted around the +Y pole of the Bloch sphere, where spin squeezing would be generated. In a mean-field analog to squeezing, points along the blue circle evolve to points along the orange ellipse. Similar dynamics mirrored about the Y–Z plane would be observed near the -Y pole. **B**, An ellipse is fitted to data (orange points in insets) prepared at different phases ϕ in the X–Z plane and angles θ_Y^0 from the +Y axis (blue points in insets) after 2.4 ms evolution time. The aspect ratio of the ellipse, as measured along axes with angle $\pi/4$ and $-\pi/4$ from the +Z axis, is plotted as a function of the initial spin $\langle S_Y^0 \rangle = \cos\left(\theta_Y^0\right)/2$ (black points). The same fit to the mean-field simulations is plotted as the black line. The insets show the X and Z components of the initial and final Bloch vectors for $\theta_Y^0 = \pi/4$ and $3\pi/4$. The axis range is -0.5 to 0.5. **C**, TAT mean-field dynamics plotted around the +Y pole of the Bloch sphere. The contours at $\phi = -\pi/4, 0$ and $\pi/4$ are plotted in green, dark gray and purple, respectively. **D**, Measured values of $\langle \theta_Y \rangle$ after 2.4 ms evolution under TAT dynamics are plotted as a function of θ_Y^0 for $\phi = \pi/4$ (green circles), 0 (gray diamonds) and $-\pi/4$ (purple squares). The lines are mean-field simulation results under the same conditions.

We observed the mean-field version of the squeezing generated by TAT by preparing a ring of initial states in an $X-Z$ plane of the Bloch sphere for different values of $\langle S_Y^0 \rangle$ and fitting their positions after evolution under TAT for 2.4 ms to an ellipse (positions before (after) evolution in blue (orange) are shown in insets in Fig. 4.10b). We plot the ratio of the sizes of the fitted ellipses along the $X = \pm Z$ directions as a function of $\langle S_Y^0 \rangle$ (Fig. 4.10b). Near $\langle S_Y^0 \rangle = \pm 1/2$,the ellipses are more stretched, with the major axis in opposite directions. The measured shapes agree well with a mean-field simulation of the experiment (solid line in Fig. 4.10d). The reduced size of the ellipse after time evolution relative to the initial circle is probably a result of dephasing from collisions and inhomogeneous dynamics between the layers. Near the $\pm Y$ poles, the rate of rotation of the Bloch vector is proportional to the Bloch vector's angle from the pole, resulting in exponential growth of the displacement with time. We measured the change in the angle θ_Y between $\langle \mathbf{S} \rangle$ and the $\hat{Y}$ axis for an evolution time of 2.4 ms after preparing states at a range of $\langle S_Y^0 \rangle$ values for $\langle S_X^0 \rangle = \pm \langle S_Z^0 \rangle$, for which $\frac{\mathrm{d}\theta_Y}{\mathrm{d}t}$ should be extremized, and $\langle S_X^0 \rangle = 0$, for which it should be zero (green, purple and gray lines in Fig. 4.10c, respectively). We observe good agreement with the mean-field model at 2.4 ms evolution time (green ($\langle S_X^0 \rangle = \langle S_Z^0 \rangle$), purple ($\langle S_X^0 \rangle = -\langle S_Z^0 \rangle$) and gray ($\langle S_X^0 \rangle = 0$) points and solid lines in Fig. 4.10d). As a result of the finite time, $\Delta\theta_Y$ (gray points in Fig. 4.10d) is non-zero for $\langle S_X^0 \rangle = 0$, although $\frac{\mathrm{d}\theta_Y}{\mathrm{d}t} = 0$ at $t = 0$.

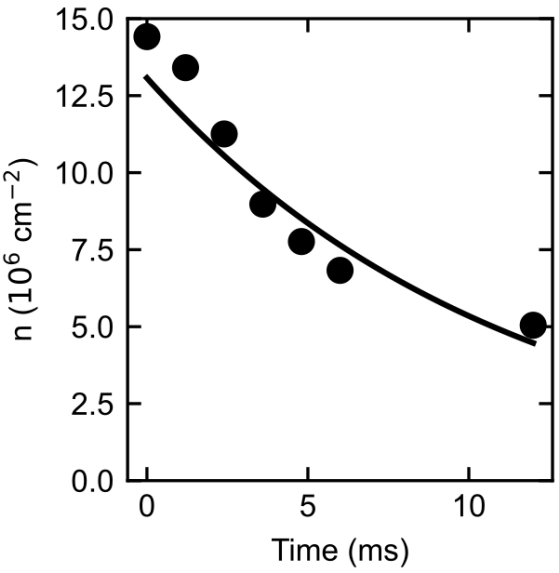

Figure 4.11: **Number loss during TAT Floquet engineering.** The average molecule density is plotted as a function of time as the XY8-TAT pulse sequence is repeatedly applied. The solid curve shows an exponential fit to the data, with time constant 11.2(6) ms.

4.4 Outlook

This chapter describes our work demonstrating multiple methods for tuning interactions between itinerant molecules and characterizing their short-time dynamics at the mean-field level.

In Ch. 5, I discuss our exploration of the limits of the all-to-all spin model that effectively describes the measurements in this chapter, as well as our study of the effect of motion on the spin dynamics. Focusing on short-time dynamics, some interesting directions for future work could include:

- Both OAT and TAT are expected to generate spin-squeezed states, with TAT approaching the Heisenberg limit [169, 191]. This could be verified by measuring the spin noise in addition to $\langle \mathbf{S} \rangle$, likely in a single-layer system. If a squeezed state is successfully created, it could be used in a proof-of-principle experiment on quantum-enhanced metrology, for

instance measuring electric fields or gradients. Demonstration of spin squeezing with polar molecules would be valuable for future precision measurement experiments, for which molecules offer enhanced sensitivity to new physics [33]. Some preliminary efforts in that direction are discussed in Ch. 7.

- Exploring the short-time spin dynamics of molecules that are pinned in a deep lattice, or allowed limited itinerance through tunneling may show qualitatively different or interesting trends. A complementary direction could be using local readout to measure correlations, as in [147, 192].

- Modeling interactions as all-to-all should be a better approximation for deeply degenerate gases. It could be interesting to explore how the dynamics change as a function of temperature or phase space density.

- The Floquet engineering methods can be generalized to systems with more than two levels [124], allowing exploration of the physics of higher spins or synthetic dimensions encoded in rotational states [125].

Chapter 5

Probing spin-motion models with Ramsey spectroscopy

"Time, time, time, see what's become of me"

A Hazy Shade of Winter – Simon & Garfunkel

In Ch. 4, I showed that short-time spin dynamics of itinerant molecules can be described by mean-field models. However, at longer times, the simple model breaks down, with the length of the spin vector decaying as motion and spin are coupled by dipolar collisions between the molecules. In this chapter, I discuss our efforts to explore the many-body physics of the system through Ramsey spectroscopy, measuring the decay of magnetization after preparing a fully magnetized initial spin state. By tuning dipolar interactions with electric field strength or Floquet engineering and motion through confinement in optical lattices, we develop a quantitative understanding of the spin dynamics in different regimes. This chapter is largely based on Ref. [121], with sections describing components of [117, 123].

In Sec. 5.2, I discuss the simplest regime, in which molecules are pinned to sites of a deep 3D optical lattice. Here, a spin model parameterized by $J_\perp$ and J_z fully describes the observed dynamics. The low and stochastic lattice filling accessible in current experiments means that the dynamics are dominated by strongly-interacting clusters.

If the molecules are allowed to freely move within layers of a 1D optical lattice, as described in Ch. 4, we observe qualitatively different Ramsey contrast decay rates than with pinned molecules. In Sec. 5.3, I present our measurements in this regime, which agree with a model based on two-body collisions.

By allowing some motion with optical lattices of intermediate depth, we can interpolate between pinned and fully itinerant molecules. Taking advantage of the polar molecule platform, we were able to tune the system parameters so either motion or dipolar interactions is the dominant energy scale. In Sec. 5.4, I discuss how in this regime the molecules realize a generalized $t-J$ Hamiltonian relevant to quantum simulation of condensed matter systems, and our efforts to understand its rich out-of-equilibrium dynamics.

Finally, in Sec. 5.5, I show that XXZ Hamiltonians can also be generated by Floquet engineering, and compare their dynamics to their electric-field tuned counterparts for both pinned and itinerant molecules. This sort of verification between different experimental implementations is valuable for quantum simulation in general [20], since it is important to ensure that the target Hamiltonian is being faithfully realized. To my knowledge, our comparison, which shows regimes in which Floquet engineering is effective and others in which its performance can be improved, represents the first direct comparison between static and Floquet Hamiltonians on the same experimental platform.

5.1 Measuring Ramsey contrast decay

The measurements discussed in this chapter were all taken with similar experimental procedures. We prepared a degenerate K-Rb mixture in the xODT, then loaded the atoms into either a deep 1D vertical lattice in [117] or a deep 3D lattice in [121, 123]. After Feshbach association and STIRAP to the rovibrational ground state, we were able to produce around 15000 molecules occupying 19(1) layers of the vertical lattice at a typical temperature of 300 nK at the electric field $\mathbf{E}$ used for the experiment. For itinerant measurements in [121, 123], the horizontal lattice was then ramped to the desired depth in 5 ms.

A $\pi/2$ pulse prepares an equal superposition of $|0\rangle = |\downarrow\rangle$ and $|1\rangle = |\uparrow\rangle$. After evolution for a time T, during which a dynamical decoupling or Floquet engineering pulse sequence is applied, a final $\pi/2$ pulse with variable phase ϕ is used to map the spins from the $X-Y$ plane to the Z axis of the Bloch sphere. The number of molecules in $|0\rangle$ and $|1\rangle$ is detected using state-resolved

dissociation and imaging (Sec. 2.1.4). This process, here including a Knill dynamical decoupling (KDD) sequence [120], is shown in Fig. 5.1a.

In principle, S_z as a function of ϕ could be fit to a sinusoid, with amplitude indicating the length of the Bloch vector and the phase indicating its angle in the $X-Y$ plane. In Ch. 4, we used this procedure to measure rotations of the Bloch vector due to interactions between molecules for T up to 2.4 ms. For longer T, phase coherence between the molecules and microwaves decays, predominantly due to variations in the transition frequency $|\downarrow\rangle \leftrightarrow |\uparrow\rangle$ due to electric field noise. This results in a shot-to-shot fluctuation of the phase of the Bloch vector, which reduces the amplitude of a fit sinusoid, even if the length of the Bloch vector remains constant. We therefore extracted the Ramsey contrast as $C = 2\sqrt{2}\sqrt{\sigma_f^2 - \sigma_0^2}$ where σ_f is the standard deviation of the fraction of molecules f measured in $|\uparrow\rangle$ and σ_0 is the measured fluctuations in f with a fully decohered sample at long times [105]. We estimated the uncertainty in the contrast by bootstrapping. By repeating the measurements for different times T, we could measure how the contrast decayed over time (Fig. 5.1b). We found that the contrast decay was well described by a stretched exponential, $C(T) = e^{-(\Gamma T)^\nu}$ with dephasing rate Γ and stretching parameter ν. In all of our measurements, ν was greater than 1 – the subexponential decay may be due to number loss, spatial disorder or other effects [121, 183, 193].

To ensure that the observed dynamics were due to interactions and not one-body physics, we repeated the measurement for several initial densities. In this process, it is important to vary the density without changing other parameters of the system, like its temperature. To do so, prior to the Ramsey spectroscopy pulse sequence, we applied a microwave pulse of area θ to create a superposition $\cos(\theta)|\downarrow\rangle + \sin(\theta)|\uparrow\rangle$ before removing the population in $|\downarrow\rangle$ using resonant light from the STIRAP down leg[105]. This reduced the density by a factor of $\sin^2(\theta)/2$ uniformly across the sample, since the microwave Rabi frequency is uniform to within roughly 2% [84] and efficiency of molecule removal by STIRAP is close to unity. At $|\mathbf{E}| = 1$ kV/cm, the STIRAP also depletes molecules in $|\uparrow\rangle$, so we shelved the molecules in $|2\rangle$ before the down leg pulse [105]. For all scenarios we studied, we found that the contrast decay rate Γ increased linearly with average density n (Fig.

5.1c). We therefore fit a linear function $\Gamma(n) = \Gamma_0 + \kappa n$ in which Γ_0 represents the one-body contrast decay rate and κ the density-normalized contrast decay rate.

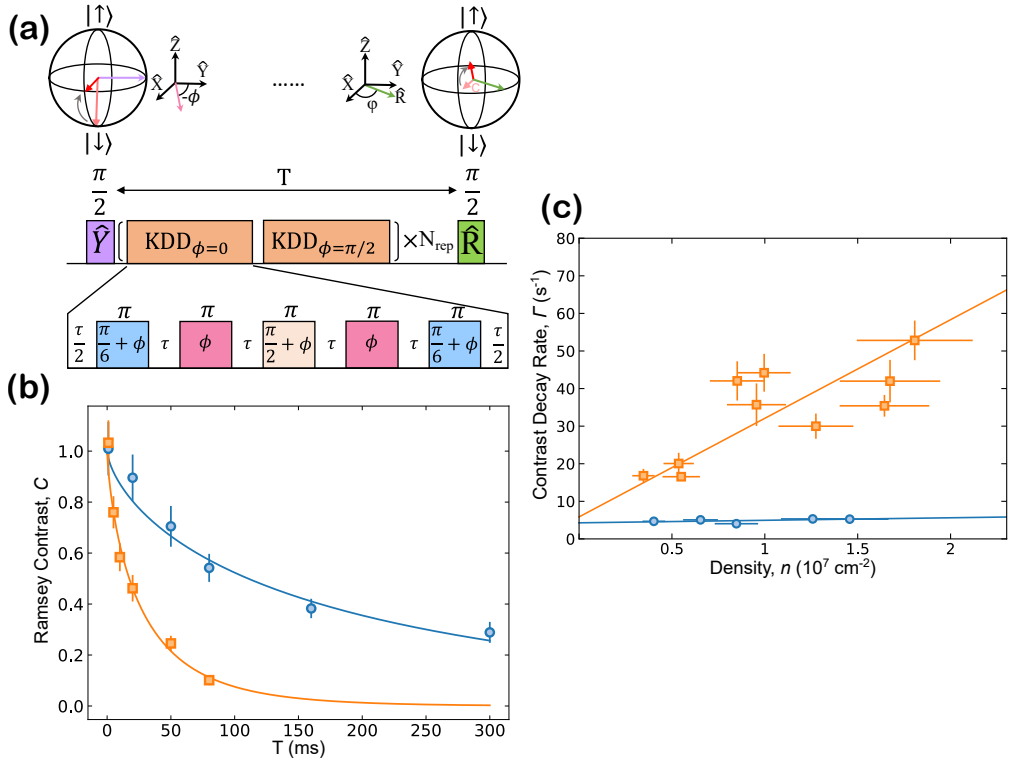

Figure 5.1: **Dynamical magnetization of interacting pinned molecules.** (a) Ramsey spectroscopy is used to measure the dynamical magnetization of the molecules. The top and middle rows show the pulse sequence, and the bottom row shows the orientation of the collective spin in the Bloch sphere representation. A $\pi/2$ pulse about the $\hat{Y}$ axis prepares the molecules in a coherent superposition of $1/\sqrt{2}(|\uparrow\rangle + |\downarrow\rangle)$. A KDD pulse sequence (shown as the top row) removes single-particle dephasing and is repeated a variable number of times N_{rep} to extend the total interrogation time to T. A final $\pi/2$ pulse about variable axis $\hat{R}$ reads out the projection of the Bloch vector orthogonal to $\hat{R}$. By repeating the measurements varying $\hat{R}$, the equatorial length of the Bloch vector, which is the Ramsey contrast (dynamical magnetization) C, at time T is extracted. (b) Measured contrast decay $C(T)$ for $\chi = 0$ (blue circles) and $\chi = 102\,\text{Hz}$ (orange squares) for initial 2D average densities of roughly 1.5×10^7 cm$^-2$ of molecules confined in a deep 3D optical lattice. Solid lines are stretched exponential fits to the experimental data. Error bars are 1 s.d. from bootstrapping. (c) Extracted Ramsey contrast decay rates versus initial density for $\chi = 0$ (blue circles) and $\chi = 102$ Hz (orange squares). Solid lines are linear fits to the data whose slopes measure density-dependent decoherence rate κ. Error bars are 1 s.e. from fits (stretched exponential fit for contrast decay rates, one-body loss for densities). From [121].

5.2 Pinned molecules: XXZ spin models

If the atoms are loaded into a deep 3D optical lattice prior to association, molecules are produced with high probability on lattice sites containing exactly one K and Rb atom in the ground band. With the conditions that can be straightforwardly achieved in the KRb apparatus, an average filling of up to 13% is possible[1] [121].

In the low filling regime, the spin dynamics of XY Hamiltonians have previously been studied with polar molecules. In Refs. [101, 102], the Ramsey contrast decay was measured using KRb molecules in a bulk 3D system. In Ref. [147], the correlations during time evolution were measured using quantum gas microscopy of a 2D system. The dynamics of higher filled systems have been studied using magnetic [194] or Rydberg [195] atoms.

Taking advantage of our ability to control interactions with electric fields and advanced microwave pulse sequences, we revisited the spin dynamics of pinned molecules under more general XXZ Hamiltonians. Besides elucidating the effect of varying the anisotropy of the interaction, this relatively simple regime allowed us to test our experimental procedures and modeling before studying more complex itinerant systems. We repeated the measurement at several electric fields between 1 and 12.7 kV/cm, finding κ is roughly proportional to $|\chi|$ (Fig. 5.2a), with slightly faster decay for predominantly Ising interactions ($\chi > 0$) than spin exchange interactions ($\chi < 0$).

At 6.5 kV/cm, corresponding to $\chi = 0$, we measured $\kappa = 0.07(7) \times 10^{-6}\mathrm{cm}^2\mathrm{s}^{-1}$, consistent with no density-dependence of the contrast decay. For $\chi = 0$, the XXZ Hamiltonian reduces to the XXX Hamiltonian $H_{XXX} = \sum_{i<j} J_{ij}\mathbf{s}_j \cdot \mathbf{s}_k$. Any initial state on the surface of the Bloch sphere is an eigenstate of this Hamiltonian, so no interaction-induced dephasing is expected.

An understanding of the experimental results can be developed by analyzing the spin model that we realized. In the low filling regime, decay of Ramsey contrast is dominated by strong interactions within local neighborhoods. To develop an intuition for the dynamics in the simplest case, we can consider two molecules initialized in the state $|-Y\rangle \otimes |-Y\rangle$. After evolution for time

[1] Prospects for increasing the filling are discussed in Ch. 6.

T under an XXZ Hamiltonian $H = J_\perp(s_1^X s_2^X + s_1^Y s_2^Y) + J_z s_1^Z s_2^Z$ (where here we absorb the spatial component of the interaction J_{ij} in Eq. 4.2 into the definitions of $J_\perp$ and J_Z), the state is

$$\psi(T) = \frac{1}{2} e^{-iJ_z T/4} \left(|\downarrow,\downarrow\rangle - |\uparrow,\uparrow\rangle - ie^{-i(J_\perp - J_z)T/2}(|\downarrow,\uparrow\rangle + |\uparrow,\downarrow\rangle) \right) \tag{5.1}$$

Neglecting a global phase, the state oscillates between the initial product state with $\langle S_y \rangle = -1$, thus $C = 1$, and the state $(|\downarrow,\downarrow\rangle - |\downarrow,\uparrow\rangle - |\uparrow,\downarrow\rangle - |\uparrow,\uparrow\rangle)/2$ with $\langle S_y \rangle = 0$ and $C = 0$ with frequency $(J_\perp - J_z)/2 = \chi/2$. This behavior was apparent in [101, 102], in which oscillations in the contrast were observed at the frequency corresponding to the interaction strength between neighboring lattice sites and in [147], in which the oscillating correlations between neighboring molecules were directly observed. Because molecules at different distances and orientations interact, oscillations at different frequencies will add up, leading to an overall decay of the contrast, even considering only two-particle subsystems.

Clusters containing more than two particles are needed to quantitatively describe the observed dynamics, particularly for $\chi < 0$. In order to explain observations in [101], Ana Maria Rey's group developed a numerical method known as moving-average cluster expansion (MACE) [102]. In MACE, a system of spins representative of the experimental geometry and disorder is initialized. Then, each spin's dynamics are simulated by solving the Schrödinger equation for the cluster containing the spin and its M most strongly coupled neighbor. Observables, such as the contrast, are estimated by averaging over the central spins of each cluster. For $M \geq 6$, the simulated contrast decay rates agree well with experimental observations. MACE results for $M = 8$ are shown as a gray line in Fig. 5.2a and agree with data with no free parameters. A slight difference is observed in both the experimental data and the MACE simulations for Ising ($\chi > 0$) and spin-exchange ($\chi < 0$) dominated dynamics. This is due to more collective behavior in the spin-exchange regime [196, 197], which can lead to oscillations in the Ramsey contrast within clusters [101, 102, 121]. Because our times are too coarsely sampled, we do not directly observe the oscillations seen in [101, 147] in [121].

The ability of MACE with small M to explain the data indicates that the dynamics in our three-dimensional system are essentially local due to the anisotropy of the dipolar interactions. For isotropic interactions or lower-dimensional systems, XXZ models can generate highly collective dynamics. In a 2D system with slightly higher filling, it should be possible to observe a dynamical phase transition [198, 199], in which, above a certain filling, the dipolar interactions keep the spins aligned, preserving Ramsey contrast at long evolution times. This regime is also expected to generate scalable spin squeezing [196, 197]. In a complementary direction, spin-exchange interactions between pinned molecules can be used to realize two-qubit gates for quantum computing. These have been demonstrated in several experiments using optical tweezer arrays [200, 201, 202, 155].

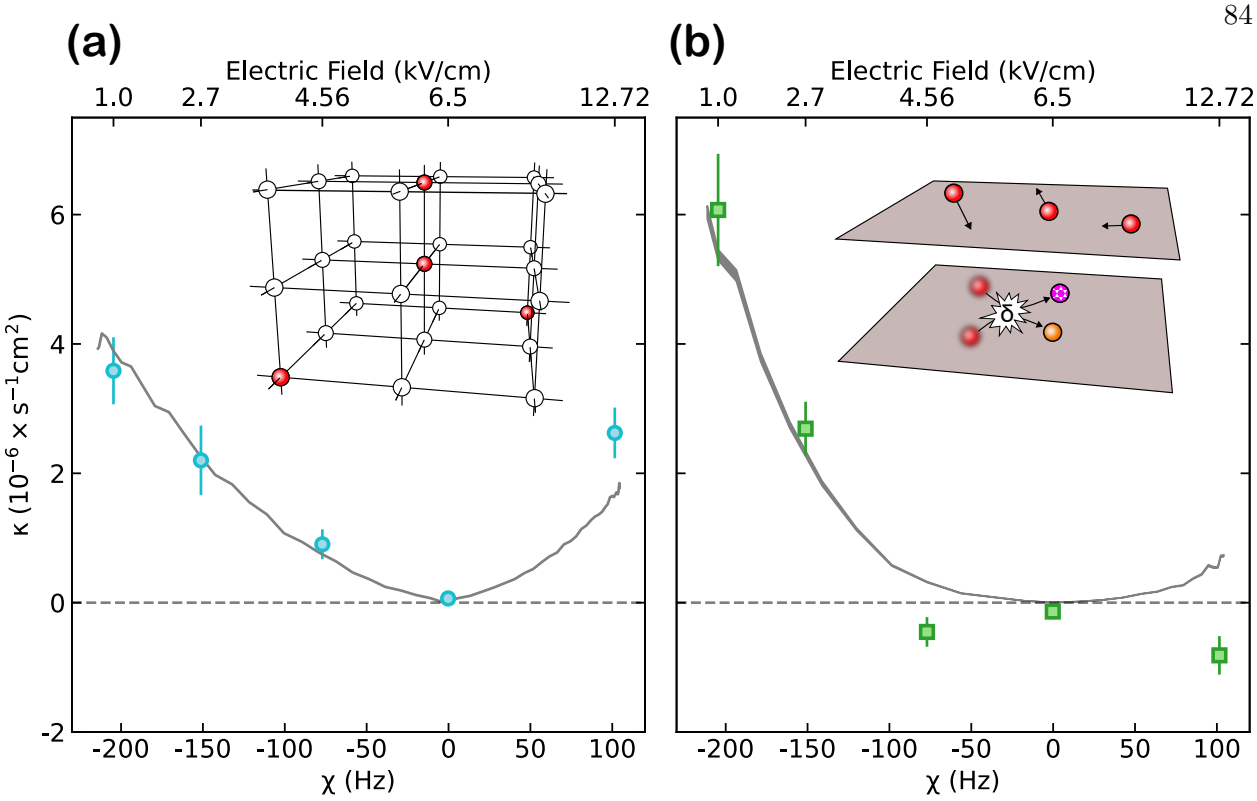

Figure 5.2: **Field-tunable density-dependent decoherence rates.** (a) Density-normalized contrast decay rates for pinned molecules tuned with interaction anisotropy χ. Blue circles are experimental data extracted from slopes illustrated in Fig. 5.1c. Error bars are 1 s.e. from linear fits. Gray line is a MACE simulation with the same density-normalization procedure as experimental data with no scaling. Inset shows the 3D lattice with fully pinned molecules, with white circles representing unoccupied sites and red circles denoting sites occupied by a molecule initially in $1/\sqrt{2}(|\uparrow\rangle + |\downarrow\rangle)$. (b) Same as (a) but for molecules confined to 2D layers without horizontal corrugation. Green squares are experimental data. Error bars are 1 s.e. from linear fits. Gray shaded band is from Monte Carlo coherent collision simulations with no scaling, with the band halfwidth representing 1 s.e. of linear fit. Inset shows 2D geometry of the system, with molecules (red circles) free to move within 2D layers. Collisional dephasing is shown schematically in the bottom 2D layer of the inset, with a collision leading to a relative phase shift $\delta = \delta_{\leftrightarrow} - \delta_{\updownarrow}$, making the molecules no longer identical after the collision, illustrated as one molecule becoming pink and the other turning orange. From [121].

5.3 Itinerant molecules: collisions

The short-time spin dynamics of itinerant molecules were discussed in detail in Ch. 4. In [117], we also measured the decay of the Ramsey contrast, finding faster decay than would be expected from the all-to-all spin model thought to describe the short-time dynamics. There, we found that the contrast decay rate increased with increasing density and χ, but did not have a detailed explanation for the contrast decay mechanism. Other groups have also observed interaction-driven decay of Ramsey contrast in 3D gases of polar molecules [149, 154], but had treated the molecules as pinned in their modeling (using MACE, as described in the previous Sec. 5.2).

The results from Ref. [117] are shown in Fig. 5.3. At 0 kV/cm, with the quantization axis defined by a magnetic field along the lattice wavevector, the Ramsey contrast over time was found to be consistent with exponential decay (Fig. 5.3a) with rate Γ increasing with density. We also measured contrast decay at 1 kV/cm with the electric field oriented 36° from the lattice $\mathbf{k}$ vector (at the magic angle, as discussed in Sec. 3.3.2.1). There, we found Γ also increased with density, but with proportionality κ 3.1(4) times lower (Fig. 5.3b). We posited that collisions between pairs of molecules randomized their phase relative to the rest of the ensemble, and attributed the difference to a reduced collisional cross-section $\sigma \propto \chi^2$, with χ at 36° being lower because of the averaged angle-dependence of dipolar interactions (Eq. 4.7). This is analogous to the relationship in atomic systems between the mean-field shift and elastic cross-section [50]. However, we did not yet have a detailed microscopic model of the contrast decay mechanism, and were not sure how our understanding would generalize to other interaction regimes.

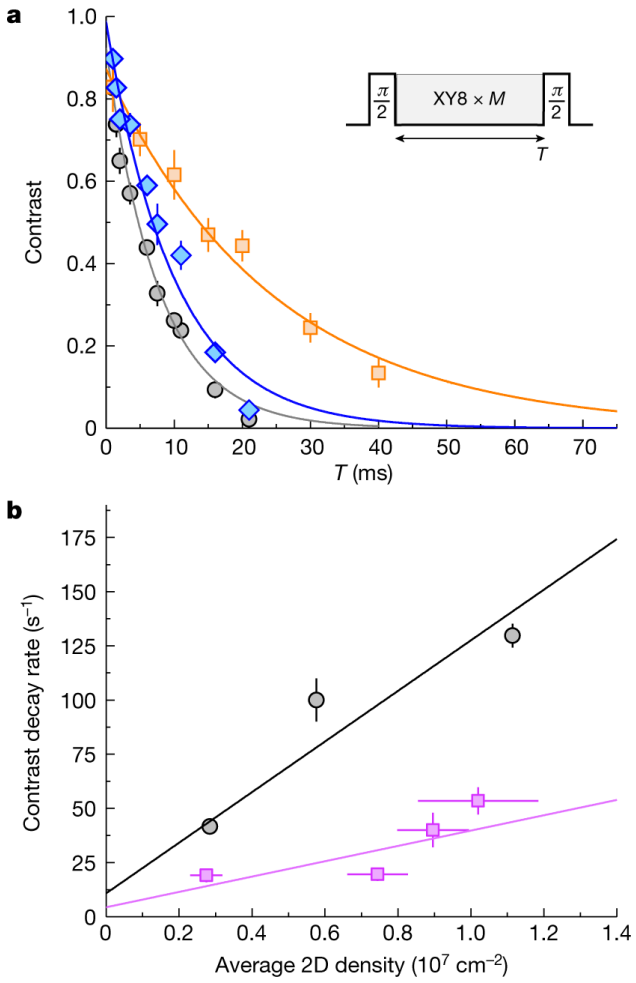

Figure 5.3: **Dipolar collisional decoherence.** (a) Decay of Ramsey contrast between $|0,0\rangle$ and $|1,0\rangle$ for density $n = 1.1(1) \times 10^7 \mathrm{cm}^{-2}$ (gray circles), $0.57(4) \times 10^7 \mathrm{cm}^{-2}$ (blue diamonds), $0.28(3) \times 10^7 \mathrm{cm}^{-2}$ (orange squares) at $|\mathbf{E}| = 0$. Decoupling sequences used are XY8 × 3 for the gray and blue traces and XY8 × 7 for the orange trace. Error bars are 1 s.d. from bootstrapping. (b) Contrast decay rate Γ as a function of n for $|\mathbf{E}| = 0$, $\alpha = 0°$ (gray circles) and $|\mathbf{E}| = 1.02$ kV cm^{-1}, $\alpha = 36°$ (purple squares). Error bars are 1 s.e. from exponential fits. From [117].

This gap in our understanding motivated us to make systematic measurements of the contrast decay of itinerant molecules at several electric fields in [121]. We followed the measurement procedure described in Sec. 5.1, ramping off the horizontal optical lattices after molecule production to produce an itinerant sample. As in the pinned case, we measured the density-normalized contrast

decay rate κ as a function of χ, as shown in Fig. 5.1b. Unlike in the short-time dynamics described in Ch. 4, where the spins can be treated as pinned in a harmonic oscillator mode space lattice [165], mode-changing collisions cause coupling between the spin and motional degrees of freedom, leading to dephasing in the spin sector. We measured that, like for pinned molecules, κ increases with $|\chi|$, but with a stronger scaling of roughly $|\chi|^3$.

Our collaborators in John Bohn's group developed two methods for understanding our observations, collisional Monte Carlo simulations and a simplified analytic model, presented in [121] and refined in [203], whose notation we largely follow. Both are based on collisions between pairs of molecules, which are assumed to be discrete events despite the long-range nature of dipolar interactions due to the nondegenerate gas's large kinetic energy. Because the molecules are spin-1/2, we can write their joint state prior to scattering in the basis of triplet and singlet states:

$$\text{triplet}: \begin{cases} |\Downarrow\rangle & = |\downarrow,\downarrow\rangle \\ |\Psi^+\rangle & = \frac{|\downarrow,\uparrow\rangle+|\downarrow,\uparrow\rangle}{\sqrt{2}} \\ |\Uparrow\rangle & = |\uparrow,\uparrow\rangle \end{cases} \tag{5.2}$$

$$\text{singlet}: \begin{cases} |\Psi^-\rangle & = \frac{|\downarrow,\uparrow\rangle-|\downarrow,\uparrow\rangle}{\sqrt{2}} \end{cases} \tag{5.3}$$

We take the molecules as initially prepared in the state $|X\rangle$ (varying by a global phase from the initial state in Sec. 5.2 for notational simplicity) such that

$$\psi(0) = \frac{1}{2}\left(|\downarrow,\downarrow\rangle + |\uparrow,\uparrow\rangle + |\downarrow,\uparrow\rangle + |\uparrow,\downarrow\rangle\right) = \frac{1}{2}(|\Downarrow\rangle + |\Uparrow\rangle + \sqrt{2}\,|\Psi^+\rangle) \tag{5.4}$$

The first collision therefore occurs entirely in the triplet sector. Because Fermi statistics suppress close approaches between identical molecules, collisions in this sector are primarily elastic, leading to scattering off the dipolar potentials at long range. This means that the primary effect of the collisions on the spin sector is that the involved molecules pick up a phase relative to the other molecules. The phase shift is proportional to dipole length $a_D = \frac{m}{2\hbar^2} d^2 4\pi\epsilon_0$, with d being the dipole

moment [204]. We make the further simplifying assumption that the dynamical decoupling sequence is fast compared to the collisions, so that $|\Downarrow\rangle$ and $|\Uparrow\rangle$ states are constantly switched, thus take on the same scattering phase shift $\delta_{\updownarrow} \propto d_{\downarrow}^2 + d_{\uparrow}^2 \propto V + \frac{J_\perp}{4} + \frac{\chi}{4}$ (where the dipole moments are found as in Sec. 3.1). The anti-aligned triplet states $|\Psi^+\rangle$ take on a different phase shift $\delta_{\leftrightarrow} \propto d_{\downarrow\uparrow}^2 + d_{\downarrow} d_{\uparrow} \propto V + \frac{J_\perp}{4} - \frac{\chi}{4}$. The collision results in a change in contrast $\Delta C = 2\sin^2(\delta_{\leftrightarrow} - \delta_{\updownarrow}) \propto \chi^2$ for small $\delta_{\leftrightarrow} - \delta_{\updownarrow} \propto \chi$ (shown schematically in inset of Fig. 5.2b). The overall contrast decay rate is $\kappa \propto \Delta C \beta_{\mathrm{el}}$, where $\beta_{\mathrm{el}} = n\sigma \langle v \rangle$. For low-energy dipolar identical fermions in 2D, $\sigma \approx 8\pi k a_d$, where k is the colliding pair's relative momentum [99, 205, 204]. Both the aligned and anti-aligned channels contribute to the elastic scattering, such that $\beta_{el} = (\beta_{\updownarrow} + \beta_{\leftrightarrow})/2 = 8\pi\hbar k^2((a_d^{\updownarrow})^2 + (a_d^{\leftrightarrow})^2)/m$, where the dipole moments for $a_d^{\updownarrow}$ and $a_d^{\leftrightarrow}$ are $d_{\downarrow}^2 + d_{\uparrow}^2$ and $d_{\downarrow} d_{\uparrow} + d_{\downarrow\uparrow}$ respectively. In general, since $J_\perp$ (J_z) decreases (increases) with increasing $|\mathbf{E}|$, $\beta_{\leftrightarrow}$ ($\beta_{\updownarrow}$) follow the same trend. Computation of the product for κ gives super-linear scaling with χ, as observed in the data.

For a more quantitative model [121, 203], we describe the effects of a collision through scattering matrix S, which transforms the pre-collision two-molecule density matrix ρ into the post-collision state $\rho' = S\rho S^\dagger$. In the selected basis, S is taken as diagonal but not unitary - the large energy scale for inelastic collisions should lead to loss of the involved molecules through chemical reaction or expulsion from the trap. The collision cross-sections and matrix elements of ρ are computed by solving the quantum scattering problem and used as inputs to a Monte Carlo simulation of the dynamics. In the simulation, the molecules move along classical trajectories under influence of external potential. Following the direct simulation Monte Carlo method [206], nearby pairs of molecules are sampled to undergo collision, picking up the appropriate phase shifts and momentum change, or possibly undergoing inelastic loss. Assuming Markovian dynamics, entanglement between pairs of molecules is ignored, with the single-particle reduced density matrix of each molecule used as the initial state for the next collision. The contrast as a function of time is computed as the expectation value of S_x, averaged over all the remaining molecules. The results of the Monte Carlo simulation is plotted along with experimental data as the gray band in Fig. 5.2b, showing excellent agreement.

One interesting effect observed in both the data and the simulation is a decrease in the contrast decay rate due to collisional loss. The kinetic energy of the molecules is insufficient for inelastic collision at long range. At short range however, chemical reactions can occur, leading to loss of molecules. Scattering of identical fermions cannot occur in the singlet channel, but at low energies predominantly takes place in the triplet channel, which has a μK-scale p-wave barrier [207]. Once a molecule has undergone a collision, it picks up a phase shift, and is no longer identical to the remaining molecules in the gas. Further collisions can therefore occur in the singlet channel, which lacks the barrier and can have attractive interactions. As a result, molecules colliding in singlet channel (which will have already undergone dephasing collision), are lost much faster than molecules colliding in triplet channel [83]. This process, dubbed "loss-induced autoselection", extends contrast of the remaining molecules beyond what would be expected without loss. This mechanism, however, is not sufficient to explain the negative values of κ observed around $\chi = 0$ in Fig. 5.2b [203].

Given the excellent agreement between the simulation and the data, we have an improved understanding of the itinerant contrast decay dynamics in the non-degenerate regime. In the future will be interesting to explore the effect of Fermi degeneracy where Pauli blocking [208] would be expected to play a role. For a deeply degenerate single-layer gas, the dipolar interactions are expected to be approximately all-to-all [165]. Recent theory [209] and measurements with magnetic atoms [194] suggest slower contrast decay and enhanced coherent dynamics with degenerate, itinerant systems. This regime will be exciting to explore with the highly tunable interactions between polar molecules.

5.4 Generalized t-J models

When horizontal optical lattices of intermediate depth are applied, the molecules' motion is strongly modified. Rather than freely moving within a harmonic oscillator potential, the molecules instead coherently tunnel between neighboring lattice sites with rate t (Sec. 3.3.1). In this regime, the molecules realize a version of the t-J Hamiltonian (Eq. 1.2), which has been widely studied in the condensed matter community. The t-J model, and variations thereof, are known to possess a

rich phase diagram and believed to describe the essential features of high-temperature superconductivity (Sec. 1.2) [17]. Ultracold atoms in optical lattices have emerged as a leading platform for quantum simulation of Fermi-Hubbard and t-J Hamiltonians [210], but the $J = 4t^2/U$ scaling of superexchange interactions restrict the portion of the phase diagram that can be explored to $J \ll t$ and require extremely low temperatures to reach interesting portions of the phase diagram [14].

Polar molecules in optical lattices provide an alternative platform for realizing a highly tunable generalization of the t-J Hamiltonian, the t-J-V-W model [76, 211]

$$\begin{aligned}\hat{H}_{tJVW} = &- h \sum_{\langle i,j\rangle,\sigma} t_{ij} \left(\hat{c}^\dagger_{i\sigma}\hat{c}_{j\sigma} + \text{h.c.}\right) + h\sum_{i\neq j} \frac{V_{ij}}{2}\left(J_\perp \hat{\mathbf{s}}_i \cdot \hat{\mathbf{s}}_j + \chi \hat{s}^Z_i \hat{s}^Z_j + V\hat{n}_i\hat{n}_j + W\left(\hat{n}_i\hat{s}^Z_j + \hat{n}_j\hat{s}^Z_i\right)\right) \\ &+ hU\sum_i \hat{n}_{i\downarrow}\hat{n}_{i\uparrow} \end{aligned} \tag{5.5}$$

which includes tunneling t, dipolar XXZ interactions J, density-density interactions V, and density-spin interactions W.

Theoretical work suggests that the additional terms in the t-J-V-W model may lead to qualitatively different physics than the basic t-J or Fermi-Hubbard models. Recent computational studies [72] suggest that beyond-nearest-neighbor interactions are needed to realize superconducting phases in Hubbard models. Other modifications to the phase diagrams may emerge, such as superconducting phases at half filling [212]. Anisotropy of dipolar interactions, encoded in the coefficient V_{ij}, is another rich tuning knob [75, 173] that may enable rich new phases or dynamics. Thus, the realization of t-J-V-W models is well-motivated from the perspective of quantum simulation and many-body physics.

While the initial temperatures we can currently achieve are far above those at which ordered phases are expected to occur, we can still apply Ramsey spectroscopy to study the system's dynamics. This probe allows us to demonstrate experimental tuning of the Hamiltonian terms, benchmark state-of-the-art theoretical tools for modeling quantum dynamics, and establish a baseline for behavior against which future work with ordered phases can be compared. We discuss our measurements and analysis in Sec. 5.4.2, after summarizing how the terms in the Hamiltonian

emerge from dipolar interactions between molecules.

5.4.1 The dipolar t-J-V-W Hamiltonian

In this section, I briefly discuss the origin of the terms in the t-J-V-W Hamiltonian for polar molecules in an optical lattice, building on the discussion of t-J and Hubbard models in Sec. 1.2. For more detail, refer to [211]. The t term in the t-J-V-W Hamiltonian (Fig. 5.4b) comes from tunneling of molecules between lattice sites and can be tuned by varying the depth of the optical lattices (Sec. 3.3.1). By using horizontal lattices at the magic angle (Sec. 3.3.2), we keep t equal for both rotational states, but, in principle, each state's t could be independently tuned using a state-dependent lattice. t can be independently tuned for the different lattice directions – in the current experiments, the vertical tunneling $t_y \approx 0$. For lattices deeper than approximately 10 E_r, tunneling of ground band molecules between neighboring sites is a good description of the motion. For shallower lattices, next-nearest neighbor tunneling and, for depths below approximately 5 E_r at our current temperatures, thermal occupation of higher bands become relevant (see SI of [121]).

The remaining terms are due to the electric dipole interactions between molecules, as summarized in Fig. 5.4c. The molecules possess induced dipole moments $d_\uparrow$ and $d_\downarrow$ and transition dipole moment $d_{\uparrow\downarrow}$ (Sec. 3.1). All the dipolar interaction terms follow the same spatial dependence (Eq. 4.3), whose coefficient is found by integration of $V_{\mathrm{dd}}(\mathbf{R}) = \frac{1}{4\pi\epsilon_0(Ra_x)^3}(1-3(\hat{\mathbf{R}}\cdot\hat{\mathbf{E}})^2)$ over each pair of site's ground state Wannier orbitals $w_i(\mathbf{r})$:

$$V_{ij} = \int \mathrm{d}\mathbf{r} \int \mathrm{d}\mathbf{r}'\, w_i(r) w_i^\dagger(r) V_{\mathrm{dd}}(\mathbf{r}-\mathbf{r}') w_j(r') w_j^\dagger(r') \tag{5.6}$$

where r is taken in units of the horizontal lattice spacing. While J_{ij} is approximately proportional to $1/r_{ij}^3$, the finite extent of the wavefunction increases J_{ij} at short range relative to molecules located exactly at the center of their lattice sites [213]. In the full Hamiltonian, there are also terms in which the molecules hop to different sites due to the dipolar interactions, but these are strongly suppressed by the small overlap of Wannier functions in deep lattices [213].

The $J_\perp$ and χ terms are the same as those discussed in the pinned and fully itinerant XXZ

Hamiltonians in Secs. 5.2 and 5.3. The spin-exchange interaction $hJ_\perp = 2d^2_{\uparrow\downarrow}$ describes hopping of an excitation from one molecule to another. The Ising interaction $hJ_z = (d_\downarrow - d_\uparrow)^2$ originates from the difference between the two states' induced dipole moments. We choose to parameterize the Hamiltonian in terms of $\chi = J_z - J_\perp$, such that χ describes the deviation of the Hamiltonian from the isotropic XXX Hamiltonian. $J_\perp$, J_z, and χ are shown as a function of electric field in Fig. 5.4d. The density-density interaction $hV = (d_\downarrow + d_\uparrow)^2/4$ is due to the average induced dipole moment and the density-spin term $hW = (d^2_\uparrow - d^2_\downarrow)$ arises from the cross-term of differential and average dipole moments.

There are several Hamiltonian terms of varying levels of importance that are not explicitly included in the t-J-V-W model. The most important is an external confining potential $\sum_i V_{\mathrm{ext}}(i)\hat{n}_i$, which is approximately harmonic and state-independent in the current experiment. In addition, the t-J-V-W model approximates a generalized Fermi-Hubbard Hamiltonian, in which multiple molecules can occupy the same lattice site. Doublon population is suppressed by kHz-scale on-site dipolar and contact interactions and doublons also undergo rapid s-wave loss. Finally, the molecules also undergo one-body loss and heating from light scattering [100] and intensity and phase noise of the optical traps [62]. These occur over timescales of tens of seconds, which are much longer than the duration of present experiments.

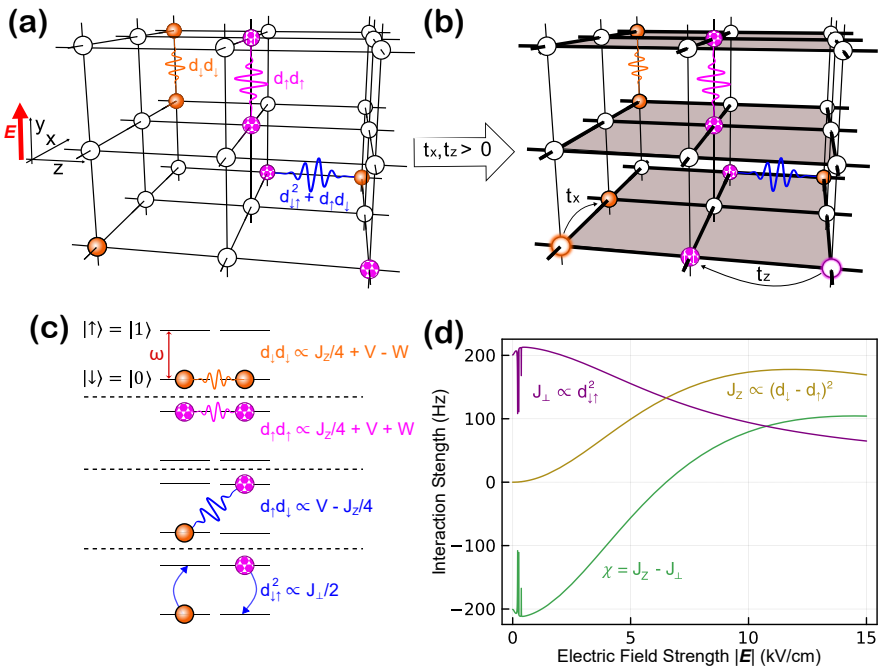
(a)
(b)
(c)
(d)
E
y
x
z
$d_\downarrow d_\downarrow$
$d_\uparrow d_\uparrow$
$d^2_{\downarrow\uparrow} + d_\uparrow d_\downarrow$
$t_x, t_z > 0$
t_x
t_z
$|\uparrow\rangle = |1\rangle$
$|\downarrow\rangle = |0\rangle$
ω
$d_\downarrow d_\downarrow \propto J_z/4 + V - W$
$d_\uparrow d_\uparrow \propto J_z/4 + V + W$
$d_\uparrow d_\downarrow \propto V - J_z/4$
$d^2_{\downarrow\uparrow} \propto J_\perp/2$
$J_\perp \propto d^2_{\downarrow\uparrow}$
$J_z \propto (d_\downarrow - d_\uparrow)^2$
$\chi = J_z - J_\perp$
Interaction Stength (Hz)
200
100
0
−100
−200
0
5
10
15
Electric Field Strength |E| (kV/cm)

Figure 5.4: **Field-tunable dipolar interactions between lattice-confined molecules.** (a) Molecules sparsely occupy a deep 3D optical lattice. Sites are shaded white if unoccupied, pink patterned if in the $|\uparrow\rangle$ state, and solid orange if in the $|\downarrow\rangle$ state. Molecules interact with induced dipole moments and transition dipole moments represented by squiggly lines between lattice sites. (b) Lowering the lattice depth in the horizontal directions allows tunneling between sites within layers, represented by the black arrows t_x, t_z. For most of our experiments $t_x = t_z$. (c) Molecular interactions arising from dipole moments can be rewritten in terms of $J_\perp$, J_Z, V, and W, the spin-exchange, Ising, density-density, and spin-density interactions, respectively, which are used in a spin-basis Hamiltonian. The interactions set by $d_\downarrow^2$, $d_\uparrow^2$, $d_\uparrow d_\downarrow$, and $d_{\downarrow\uparrow}^2$, and their associated Hamiltonian terms, are drawn schematically from top to bottom. The two lowest rotational states of the molecules, $|\downarrow\rangle$ and $|\uparrow\rangle$, are split by microwave-frequencies ω (red arrow between the spin levels in top row). (d) Calculated dipolar interaction strengths for KRb molecules separated by 532 nm perpendicular to the dipole orientations as a function of $|\mathbf{E}|$. Purple represents the spin-exchange interaction $J_\perp$ arising from the transition dipole moment between a $|\downarrow\rangle$ molecule and a $|\uparrow\rangle$ molecule which decreases with increasing electric field magnitude, gold represents the Ising interaction J_Z from induced dipole moments which increases with increasing field strength, and green represents the interaction-type anisotropy $\chi = J_Z - J_\perp$ which crosses zero around 6.5 kV/cm. Hyperfine structure of the molecules produces interaction strengths that change dramatically with small changes in $|\mathbf{E}|$ for small electric fields less than 1 kV/cm. From [121].

5.4.2 Tunable t-J-V-W spin dynamics

In Ref. [121], we measured the density-normalized Ramsey contrast decay rate κ, following the procedure in Sec. 5.1 for a range of t-J-V-W Hamiltonians. Following molecule production in a deep 3D optical lattice at $|\mathbf{E}|$ between 1 kV/cm and 12.72 kV/cm, and removal of some fraction of the molecules to realize a target filling up to 13%, we ramp one or both of the horizontal lattices to depths calibrated to provide tunneling rates $t_{x,y}$ between 0 and roughly 250 Hz (Sec. 3.3.1). Because we apply a KDD [120] pulse sequence, the spins are rapidly flipped between the $|\downarrow\rangle$ and

$|\uparrow\rangle$, averaging the W term to zero. We also do not expect the V term to play a major role in the dynamics at low filling [121], so we describe our measurement parameters in terms of χ and t. The resulting measurements of κ for $|\mathbf{E}| = 1$ kV/cm ($\chi = -205$ Hz; black circles), 6.5 kV/cm ($\chi = 0$ Hz; blue squares), and 12.72 kV/cm ($\chi = 102$ Hz; orange triangles) are shown as a function of lattice depth for molecules allowed to tunnel with rate t (horizontal axis) in one (Fig. 5.5c) or two (Fig. 5.5a) directions. The pinned and fully itinerant data discussed in Sec. 5.2 and Sec. 5.3 are shown as the leftmost and rightmost points, respectively. As in the fully pinned and fully itinerant cases, κ is close to zero at $\chi = 0$ for all tunneling rates, as the isotropic XXX interactions do not lead to dephasing. We discuss the other data in more detail.

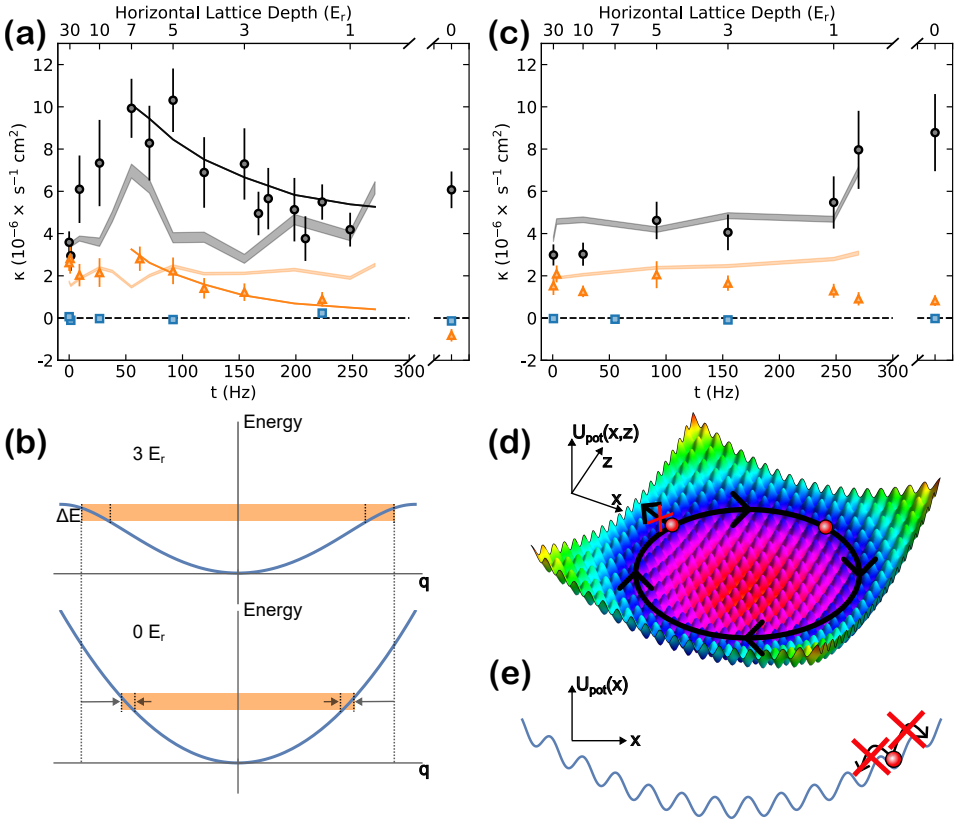

Figure 5.5: **Tuning coherent t-J dynamics**. (a) Density-dependent contrast decay versus tunneling rate t in two directions. Black circles, blue squares, and orange triangles represent experimental data for $\chi = -205, 0, 102$ Hz respectively. Horizontal axis break occurs when transverse lattices are turned off (case of Fig. 5.2b). Error bars are 1 s.e. from linear fits. Light gray (orange) bands are EMACE simulations for $\chi = -205$ Hz ($\chi = 102$ Hz) with no scaling, with the band halfwidth representing 1 s.e. of linear fit. Black (orange) solid lines shown for $t > 50$ Hz are two-body simulations with a scaling by 0.75 for $\chi = -205$ Hz ($\chi = 102$ Hz). (b) Top row shows kinetic energy of two particles in a 3 E_r lattice as a function of relative quasimomentum q, and the bottom shows the kinetic energy in the absence of a lattice where $q = k$. Shaded orange regions show the range of momentum states within a given energy interval, showing the increased density of states in a shallow lattice compared to the no lattice case. (c) Same as (a) but for tunneling only in one direction. (d) 3D rendering of the single-molecule potential energy U_{pot} in the $\hat{x}$ and $\hat{z}$directions arising from a weak 2D optical lattice and a crossed optical dipole trap. Colors indicate equipotential surfaces. Due to the site-to-site energy shift, molecular tunneling along the radial directions is suppressed, and instead tunneling occurs along azimuthal rings. (e) Schematic of the localization of molecules within a potential landscape U_{pot} produced by a weak 1D optical lattice in the $\hat{x}$ direction and a crossed optical dipole trap (equivalently, by taking a 1D slice of the 2D lattice potential shown in (d)) due to site-to-site energy shifts, when the motion is also frozen in the other two directions by deep optical lattices. From [121].

We first consider the scenario where tunneling is allowed in two directions. For $\chi = 102$ Hz, κ interpolates smoothly between its pinned and fully itinerant values. More unexpectedly, for $\chi = -205$ Hz, κ peaks for $t \approx 70$ Hz, decreasing for both weaker and stronger tunneling. Our theory collaborators were able to extend their understanding of pinned and fully itinerant systems to the t-J regime, developing models of the system that, while not showing perfect quantitative agreement, provided some intuition for the observed dynamics. When the molecules are nearly pinned, we would expect faster dephasing as some itinerance is allowed because the tunneling

couples the spin and motional degrees of freedom. In this regime, Ana Maria Rey's group was able to develop an extended version of their MACE simulation (Sec. 5.2), incorporating molecular motion. In their method, dubbed EMACE, the central molecule of each cluster was allowed to tunnel over several nearby lattice sites, and the cluster was expanded to include molecules that interact strongly with a molecule on any of the sites to which tunneling is allowed. The results of the simulation are shown as shaded bands in Fig. 5.5a and c, where the width of the band denotes 1 s.e. of a linear fit in which the EMACE results are analyzed in the same way as experimental data. The EMACE simulations, which qualitatively reproduce the peak, are computationally expensive due to their large Hilbert space, thus are unable to include other effects that may be relevant to the experimental observations, like occupation of higher bands at low lattice depth or molecular loss due to collisions.

Beginning from the itinerant side, increasing lattice depth narrows the bands that the molecules occupy (Fig. 5.5b). This increases the density of states, increasing the rate of mode-changing collisions, thus increasing the rate of decoherence in the spin sector. Additional effects that may contribute to increased contrast decay with lattice depth are an increased effective mass, which reduces velocity and increases phase shift per collision, and a suppression of loss, which preferentially removes decohered molecules. This regime was simulated using a two-body model, in which time evolution of pairs of molecules initially occupying motional eigenstates was numerically simulated. The results of the simulation, discussed in detail in the Supplementary Materials of [121], are shown as solid lines in Fig. 5.5a, with an empirically determined overall scale factor to fit the data.

We also compared the dynamics in the scenario where one horizontal lattice was kept at a sufficient depth to forbid tunneling, and the depth of the other was varied (Fig. 5.5c). There, the peak observed at $\chi = -205$ Hz with two-dimensional tunneling is absent, and κ only strongly deviates from its pinned value for lattices below approximately 1 E_r deep. We believe that this large difference is due to the harmonic potential which confines the molecules, in addition to the lattices. When the molecules are allowed to move in two dimensions, they can tunnel along a ring of sites at approximately the same potential (Fig. 5.5d), but with one-dimensional tunneling,

are mostly localized in all three dimensions (Fig. 5.5e). The observed behavior is consistent with EMACE simulations which take the confining potential into account, shown as shaded bands in Fig. 5.5c.

5.5 Validating Floquet XXZ models

In Ch. 4.3, I discussed how Floquet engineering could be used to realize a broad class of XYZ Hamiltonians and presented measurements of their mean-field dynamics. One notable subspace of these XYZ Hamiltonians is the same XXZ Hamiltonians that we generated using electric fields. This provided an exciting opportunity to compare the dynamics under electric field tuning and Floquet engineering, revealing generally similar dynamics, with differences in behavior in certain regimes.

To realize tunable Floquet XXZ Hamiltonians, we applied a DROID-R2D2 pulse sequence [185, 214], originally developed in Mikhail Lukin's group for experiments with NV centers. In addition to cancelling single-particle noise and maintaining robustness to pulse errors like the XY8 [134] and KDD [120] sequences used in our previous work [117, 121], the DROID-R2D2 sequence includes $\pi/2$ pulses, which change the orientation of the toggling frame, thus the nature of the spin model (see Sec. 4.3). In the standard DROID-R2D2 sequence, the spins spend equal time in each toggling frame orientation, thus averaging to an isotropic XXX Hamiltonian. The Ramsey coherence time of interacting NV centers was maximized under this pulse sequence [214], similar to our observations with polar molecules under an XXX Hamiltonian (Sec. 5.2). By varying the pulse spacing, a range of XXZ (or XYZ, as discussed in Sec. 4.3) Hamiltonians can be generated (blue dashed line in Fig. 5.6a), as previously demonstrated using NV centers [183]. Beginning with spin exchange interactions $g_\perp^0$ of KRb at 1 kV/cm, the coefficients of the XXZ Hamiltonian (Eq. 4.2) can be tuned between approximately $g_{\perp,Z} = \left(g_\perp^0, 0\right)$ and $g_{\perp,Z} = \left(g_\perp^0/2, g_\perp^0\right)$, which corresponds to $|\mathbf{E}| = 10.5$ kV/cm. For comparison, by varying $|\mathbf{E}|$ between 1 and 12.7 kV/cm, the coefficients $g_{\perp,Z}$ were tuned between $2\pi \times (210, 6)$ Hz and $2\pi \times (75, 177)$ Hz for molecules on adjacent lattice sites in the plane perpendicular to $|\mathbf{E}|$ (solid red trace in Fig. 5.6a).

For a range of Floquet-engineered XXZ Hamiltonians implemented with pinned molecules, we measured the Ramsey contrast decay and analyzed the data as discussed in Sec. 5.1. Raw contrast decay curves for the XY Hamiltonian, the electric-field-tuned XXX Hamiltonian, and a Floquet-engineered XXX Hamiltonian with initial densities of about 1.6×10^7 cm^{-2} are shown in Fig. 5.6b and the contrast decay rate Γ is plotted as a function of density for each condition in Fig. 5.6c. Following optimization of the Floquet pulse sequence (Sec. 5.5.1), the Floquet XXX Hamiltonian shows slightly shorter coherence time and slightly higher density-dependent contrast decay than the electric-field tuned Hamiltonian, possibly because of a slower rate of dynamical decoupling pulses or higher-order terms not fully symmetrized by the Floquet engineering. We equate the XXZ Hamiltonians realized by electric fields and Floquet engineering by determining the value of $|\mathbf{E}|$ that yields the same ratio of to as a set of Floquet timings (Fig. 5.6a). As the overall strength of the interaction decreases for higher electric fields but remains constant for the Floquet sequences, we rescale the Floquet data's κ by the ratio of under $|\mathbf{E}|$ to its value under the Floquet Hamiltonians. We plot κ as a function of χ for both datasets (Fig. 5.6d), as well as the MACE simulation (Sec. 5.2). There is good agreement between their dynamics, suggesting that Floquet engineering is realizing the desired spin models.

To investigate the limitations of Floquet engineering, we applied the same pulse sequence to itinerant molecules confined in a 1D optical lattice (Fig. 5.6e), for which motion and collisions complicate the Hamiltonian (Sec. 5.3). In the spin-exchange regime in which the Floquet engineering only slightly modifies the Hamiltonian, we observe excellent agreement between the electric field-tuned and Floquet-engineered dynamics. However, in the Heisenberg and Ising regimes, the Floquet-engineered model shows a higher rate of density-dependent contrast decay than the electric field-controlled version. We expect this to occur as the contrast decay in an itinerant system is dominated by short-range collisions between molecules. The collisions take place over durations comparable to the Floquet pulse spacing and have scattering properties set by the electric field. Nevertheless, reasonable agreement is observed between the Floquet and electric-field tuned models, indicating that control is possible over itinerant systems.

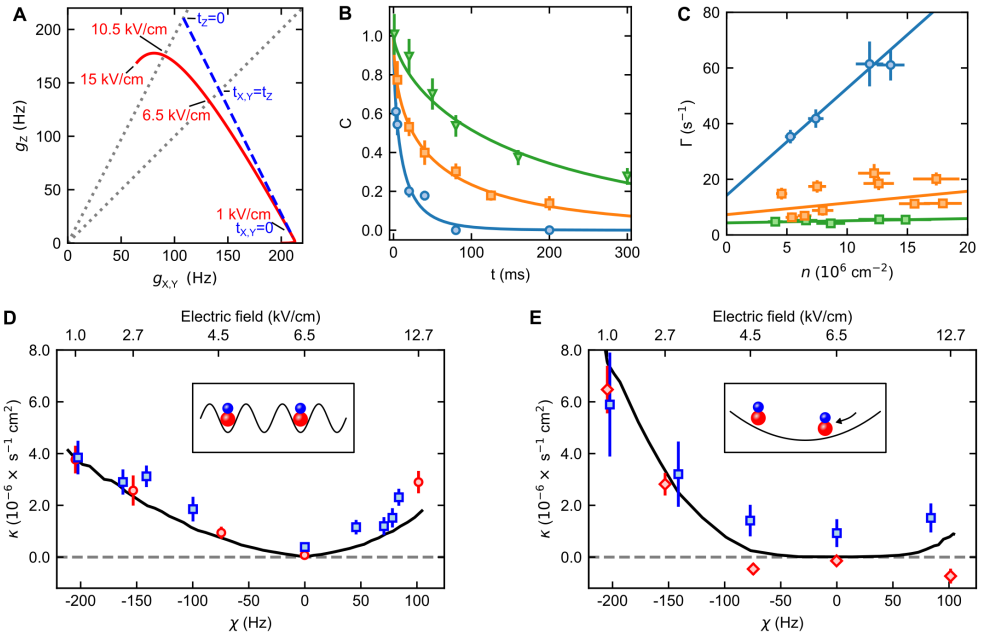

Figure 5.6: **Benchmarking XXZ spin dynamics.** **a**, XXZ Hamiltonians can be prepared with electric fields (red solid line) and Floquet engineering (blue dashed line). The dashed diagonal lines show the subspaces of coefficients with equal ratio $g_\perp/g_Z$ corresponding to the most Ising Hamiltonian that can be prepared with Floquet engineering (left) and the Heisenberg XXX model (right). **b**, Ramsey contrast as a function of time for a spin-exchange model (blue circles), a Floquet-engineered XXX model (orange squares) and an XXX model realized with electric fields (green triangles) with initial densities of about 1.6×10^7 cm^{-2}. The lines are fits to a stretched exponential. The error bars on the data are 1 s.d. from bootstrapping. **c**, The fitted contrast decay rate plotted as a function of 2D density for a spin-exchange model (blue circles), a Floquet-engineered XXX model (orange squares) and an XXX model realized with electric fields (green triangles). The Γ error bars are 1 s.e. from stretched exponential fits and the n error bars are 1 s.e. from the initial density of an exponential fit. **d**, The density-normalized contrast decay rate κ plotted as a function of $\chi = g_Z - g_\perp$ and (effective, in the case of the Floquet data) electric field for simulations (black line), electric field data (red circles) and Floquet data (blue squares) for molecules pinned in a deep 3D lattice (schematic in inset). The error bars are 1 s.e. from a linear fit. **e**, Same as **D**, but for itinerant molecules in a 1D vertical lattice. From [123]; the electric field-tuned data and simulations in this figure are from [121].

5.5.1 Optimizing Floquet pulse sequences

To optimize the pulse spacing for the Floquet XXZ experiments, we measured the contrast decay rate for an XXX Hamiltonian (selected to eliminate interaction-driven contrast decay) with pinned molecules, realized with a variety of pulse spacings between 25 and 400 μs (Fig. 5.7). If the pulse spacing is too long, interactions between the molecules will not be well symmetrized and dephasing from inhomogeneous single-particle noise will not be effectively cancelled. If the pulse spacing is too short, pulse errors can accumulate more quickly and more molecules will be driven into other hyperfine states, causing increased loss. We therefore used a pulse spacing of 100 μs for the Floquet XXZ and XYZ Hamiltonians, which was the longest spacing that shows near-optimal contrast decay rates. For the KDD pulse sequence for the d.c. electric field experiments, we used 50 μs pulse spacing, as the molecules are more sensitive to fluctuating electric fields as the dipole moment increases at larger fields, so faster dynamical decoupling than used at zero field improves contrast.

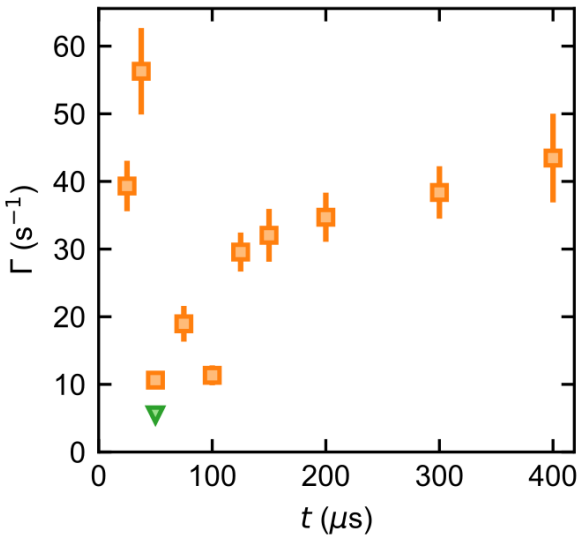

Figure 5.7: **Optimizing Floquet pulse timing.** The fitted contrast decay rate Γ is plotted as a function of pulse spacing t for molecules with initial densities around $1.8(5) \times 10^7$ cm^{-2} in a 3D lattice with parameters set to produce the XXX model. The green triangle is the electric field-tuned data with a KDD pulse sequence and the orange squares are the Floquet data with a DROID-R2D2 pulse sequence. The error bars on the plot are 1 s.e. from stretched exponential fits. From [123].

Fig. 5.8 shows the single-particle contrast decay rate Γ_0 (extracted from the intercept of the fit function $\Gamma(n) = \Gamma_0 + \kappa n$) as a function of χ controlled by electric field (red circles) or Floquet timing (blue squares). For pinned molecules (Fig. 5.8a), Γ_0 depends weakly on χ for both Floquet and electric field data. However, for itinerant molecules (Fig. 5.8b), Γ_0 shows opposite trends for the two datasets. As the electric field is increased, Γ_0 increases, possibly because molecules with larger induced dipole moments at larger electric fields experience larger phase shifts as they move through residual electric field gradients. For the Floquet data, Γ_0 increases as the Hamiltonian is tuned farther from the Heisenberg point $t_x = t_y = t_z$. This occurs because some of the spin-echo pulses in the DROID-R2D2 sequence occur at longer intervals (up to 298 μs in the most spin-exchange-dominated case) such that noise from motion in electric field or optical potential gradients is less

effectively cancelled. The coherence time could be improved with a different pulse sequence with shorter maximum intervals between spin-echo pulses.

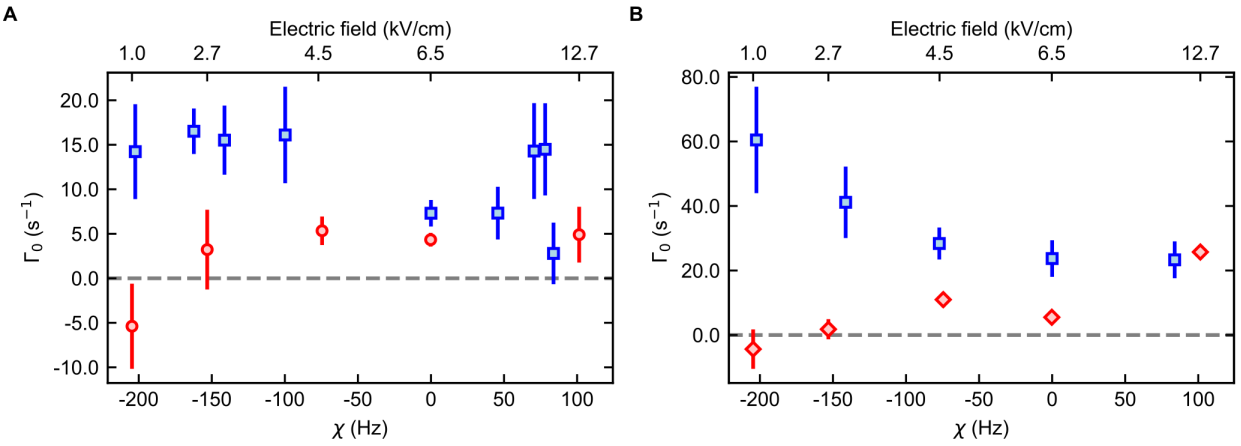

Figure 5.8: **Single-particle contrast decay rates.** The single-particle contrast decay rate Γ_0 is plotted as a function of χ and electric field for electric field data (red circles and top axis) and Floquet data (blue squares) for **A** molecules pinned in a deep 3D lattice and **B** itinerant molecules in a 1D lattice. The error bars are 1 s.e. from a linear fit. From [123].

5.6 Outlook

Although we have systematically characterized the relaxation dynamics of the t-J-V-W's model, including the fully itinerant and pinned extremes, in the low filling regime, many directions remain for future work. In roughly increasing order of difficulty, some future experiments could include:

- Studying the dynamics in an isolated two-dimensional layer may yield qualitatively different results, since the anisotropy of the dipolar interactions allows tuning between all interactions taking on the same sign, and attractive and repulsive interactions in orthogonal directions. In this geometry, long-lived synchronization of the spins [198, 199] or spin squeezing enhanced by motion [209, 194] may be observed in Ramsey spectroscopy

experiments.

- Exploring the relaxation dynamics of Floquet-engineered XYZ Hamiltonians [123]. In this case, the length of the Bloch vector would need to be measured along all three directions, as the Bloch vector's dynamics are no longer constrained to its initial $X - Y$ plane.

- Preparation of homogeneous systems through box traps [215, 216] or compensation of the external potential [22] would allow full one or two-dimensional tunneling, and support more precise measurements without the averaging over different chemical potentials in a harmonic trap.

- With local (although not necessarily site-resolved) state preparation and measurement, transport properties of the system could be explored. The relaxation of the system could be measured after preparing a localized excitation [217, 192] or modulation in density [218] or spin texture [219]. Additionally, measuring correlations with quantum gas microscopy may give insight into the local behavior of the system [147, 192, 194].

- Preparing systems at lower temperatures and higher fillings should allow exploration of ordered phases, including enhanced superfluid phases [211], and quantum simulation of cuprate superconductors [210]. Some methods for reaching lower temperatures are discussed in Ch. 6.

Chapter 6

Towards a deeply degenerate 2D Fermi gas

"I'm too hot (hot damn)

Call the police and the fireman"

Uptown Funk – Bruno Mars

6.1 Introduction

Often, the primary challenge in studying new many-body phenomena with ultracold atoms is preparing sufficiently low-entropy states to observe the phenomenon of interest. With fermionic atoms, evaporative cooling to degeneracy [8] enabled observations of the BCS-BEC crossover [52] and, later, enhanced cooling relying on redistribution of entropy between the system and a reservoir [220] enabled observation of antiferromagnetic [22] and pseudogap [70] phases of the Fermi-Hubbard model. Current efforts on improving cooling [14] are pushing experiments into theoretically intractable regimes, and may shed light on the origins of high-temperature superconductivity in cuprates [17].

Both fermionic [85, 99, 87] and bosonic [221, 222] polar molecules have been cooled to degeneracy, but the community has just begun to explore the rich physics of quantum gases of polar molecules. For instance, pairing and unconventional superfluid phases are expected to emerge in bulk monolayer [223, 224], bilayer [136, 225], and optical lattice [76] systems. Low temperatures, however, are required – p wave superfluidity in microwave-shielded NaK molecules is predicted to require $T/T_F \lessapprox 0.14$ in [226], where T_F is the Fermi temperature. Fermi surface deformation

[227] and emergence of dipolar solids [75] have been observed with magnetic atoms, but the strong, tunable interactions between polar molecules promise benefits for their study.

Besides enabling observation of new phases, degenerate molecules exhibit rich dynamics. Dipolar interactions modify the motional modes of a quasi-2D Fermi gas [228]. Above a critical filling fraction in an optical lattice, pseudospins encoded in rotational levels exhibit a synchronization phase transition [198, 199] and can scalably generate squeezed states [197, 196] for application to precision metrology and fundamental physics [33, 29]. Degenerate polar molecules in a bulk gas [165] or in a lattice with tunneling [209] should lead to enhanced squeezing, as was recently observed in magnetic atoms [194].

In order to explore some of these phenomena, we decided to build on our earlier work producing [85, 86] and cooling [99, 229] molecular quantum gases to prepare a single-layer 2D gas at even lower entropy. Because of the anisotropic nature of dipolar interactions, which average to zero in a bulk 3D system, observation of many of these collective behaviors requires a 2D system. While we had previously demonstrated selection of isolated 2D layers using microwave spectroscopy [105], we now aim to compress atoms into a single layer, enabling higher numbers and lower T/T_F after evaporative cooling. Although this effort in still ongoing, in this chapter, I discuss strategies for preparing a low-entropy molecular gas (Sec. 6.2), a new accordion lattice we implemented for compressing atoms into quasi-2D (Sec. 6.3), and preliminary work on preparing large, cold molecular gases using the new lattice (Sec. 6.4). As potential future directions to improve production and evaporation, I conclude with discussion of evaporative cooling in the accordion lattice (Sec. 6.5.1) and production of molecules in a box trap (Sec. 6.5.2).

6.2 Designing a production sequence

We consider two approaches to creating low-entropy gases, association from overlapped insulators in a 3D optical lattice (Sec. 6.2.1), and production from a bulk 2D mixture (Sec. 6.2.2). The 3D lattice can be adiabatically loaded or unloaded [230], allowing conversion between itinerant and lattice systems. After the molecules are produced, they can be further cooled by evaporation (Sec.

6.2.3).

6.2.1 Production from overlapped insulators

One possible procedure for producing a low-entropy sample of molecules is creating a Rb $N = 1$ Mott insulator (MI) overlapped with a K band insulator in a 3D optical lattice, then associating the doublons on each site into molecules. In principle, the association of Feshbach molecules [104] and transfer to the molecular ground state [113] can be very efficient, so the primary limit on molecular entropy is defects in the atomic insulators. This method was explored experimentally in [103, 104], yielding a peak filling of 25% ground state KRb molecules, and with overlapped Rb and Cs MIs in [231], yielding a peak filling of 30% bosonic Feshbach molecules, and theoretically in [232, 233]. Although we chose not to pursue this approach on the second generation KRb experiment, in this section, I discuss the thermodynamics of preparing atomic insulators in an optical lattice, and why we ultimately decided to make molecules from overlapped bulk gases.

6.2.1.1 Fermionic band insulator

Band insulators of fermionic spin mixtures [68, 234, 235] and spin-polarized fermions [103, 236, 237] have been generated in multiple experiments. Here, we estimate the experimental parameters with which we can produce a highly filled, spin-polarized band insulator of K, enabling production of low-entropy molecules in a 3D optical lattice.

We model a deep optical lattice as a set of independent harmonic oscillators with identical trap frequencies $\omega_{x,y,z}$ and site-dependent potentials V_i. Ignoring the zero-point energy common to all sites, a particle in the eigenstate (n_x, n_y, n_z) of a harmonic oscillator has energy $E_{\mathbf{n}} = \hbar \sum_{j\in\{x,y,z\}} \omega_j n_j$. Because spin-polarized fermions interact weakly, the single particle eigenstates and energies are a good approximation. The grand potential for each level is

$$\Omega_{i,\mathbf{n}} = -k_B T \ln\left(1 + \exp\left(\frac{\mu - V_i - E_{\mathbf{n}}}{k_B T}\right)\right) \tag{6.1}$$

For global chemical potential μ, the level will therefore be occupied with one particle with probability

$$P_{i,\mathbf{n}} = -\frac{\partial \Omega}{\partial \mu} = \frac{\exp\left(\frac{\mu - V_i - E_{\mathbf{n}}}{k_B T}\right)}{1 + \exp\left(\frac{\mu - V_i - E_{\mathbf{n}}}{k_B T}\right)} \tag{6.2}$$

To form a molecule on a lattice site with high probability, it is desirable to have $P_{i,0} \approx 1$ and $P_{i,|\mathbf{n}>0|} \approx 0$. $P_{i,0}$ approaches one for $\mu - V_i \gg k_B T$, reaching 90% at $\mu - V_i \approx 2.2 k_B T$. Assuming $\omega_x = \omega_y = \omega_z = \omega$, the lowest energy excited state is threefold degenerate with one motional excitation in any direction (occupation of higher states will be exponentially suppressed). The probability that all three of these levels are unoccupied is

$$(1 - P_{i,1})^3 = \left(1 + \exp\left(\frac{\mu - V_i - \hbar\omega}{k_B T}\right)\right)^{-3} \tag{6.3}$$

This approaches one for $\mu - V_i \ll k_B T + \hbar\omega$. The probability that both conditions are satisfied is plotted as a function of $\mu - V_i$ and T for a lattice with $\omega = 2\pi \times 15$ kHz in Fig. 6.1. For sufficiently low temperatures, here below roughly 100 nK, the probability is greater than 90% for a wide range of $\mu - V_i$.

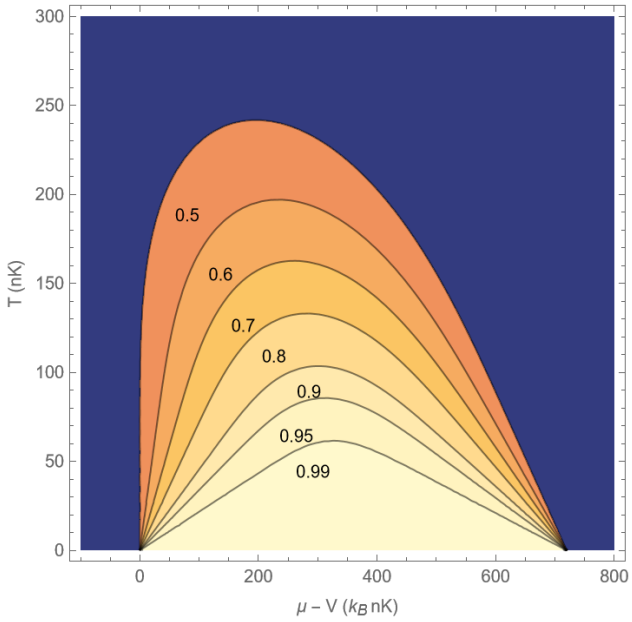

Figure 6.1: The probability of a lattice site containing one K atom in the ground state and no atoms in the first excited motional state is plotted as a function of $\mu - V$ and T for $\omega = 2\pi \times 15$ kHz.

6.2.1.2 Bosonic $N = 1$ Mott insulator

As the depth of an optical lattice is increased, bosons undergo a phase transition from a superfluid with Poissonian number fluctuations on a site to a MI phase with suppressed fluctuations [238][1] . If molecules are to be produced in a lattice, this insulating phase is desirable, since only sites containing a single atom of each species are efficiently converted into molecules. Here, I discuss the requirements for realizing the $N = 1$ MI phase for ^{87}Rb.

The interaction energy for bosons in the ground state of a lattice site is [239]

$$U = \frac{4\pi\hbar^2 a_s}{m} \int |\psi(r)|^4 \, \mathrm{d}r = \frac{4\pi\hbar^2 a_s}{2m} \left(\frac{m\bar{\omega}}{2\pi\hbar}\right)^{3/2} \tag{6.4}$$

For ^{87}Rb ($a_s \approx 100a_0$) in an isotropic lattice with $\bar{\omega} = 2\pi \times 15$ kHz (23 E_r), $U/k_B \approx 17$ nK. We assume effects of tunneling are negligible, which is a reasonable approximation for a deep

[1] The first experiment we tried after installing our 3D lattice (Ch. 2) was replicating the superfluid-MI phase transition discussed in this paper.

lattice, and incorporate the harmonic oscillator zero-point energy into the chemical potential μ. For the ground state of a single lattice site, the grand potential is

$$\Omega = -k_B T \ln\left(\sum_N \exp\left(\frac{\mu N - E}{k_B T}\right)\right) = -k_B T \ln\left(\sum_N \exp\left(\frac{N(\mu - U(N-1)/2)}{k_B T}\right)\right) \tag{6.5}$$

since each atom can interact with the other $N-1$ atoms on the site. From the grand potential, the mean atom number can be derived as

$$\langle N \rangle = -\frac{\partial \Omega}{\partial \mu} = \sum_N N P(N) \text{ where } P(N) = \exp\left(\frac{\Omega + \mu N - E}{k_B T}\right) = \exp\left(\frac{\Omega + \mu N - UN(N-1)/2}{k_B T}\right) \tag{6.6}$$

where $P(N)$ is the probability of finding N atoms on the site. In the limit where UN^2 is small compared to μ and $k_B T$, $P(N)$ approaches a geometric distribution [240] $(1-p)^N p$ with $p = 1 - \exp\left(\frac{\mu}{k_B T}\right)$. The geometric distribution has mean $(1-p)/p$ and mode 0. Thus, without interactions, the probability of finding exactly one boson on the site is maximized to 1/4 for $\mu = -\ln(2) k_B T$.

As U is increased, the fluctuations are suppressed because the energy becomes nonlinear in the particle number. The mode of the distribution is the value of N for which the argument of the exponent is maximized or $N = \frac{1}{2} + \frac{\mu}{U}$. Matching the $P(N)$ to a normal distribution and equating the quadratic terms in the exponent gives a standard deviation of $\sqrt{\frac{k_B T}{U}}$. Therefore, $k_B T$ substantially less than U (Fig. 6.2) and a particular value of μ (Fig. 6.3) are required to obtain, with high probability, a single boson per lattice site.

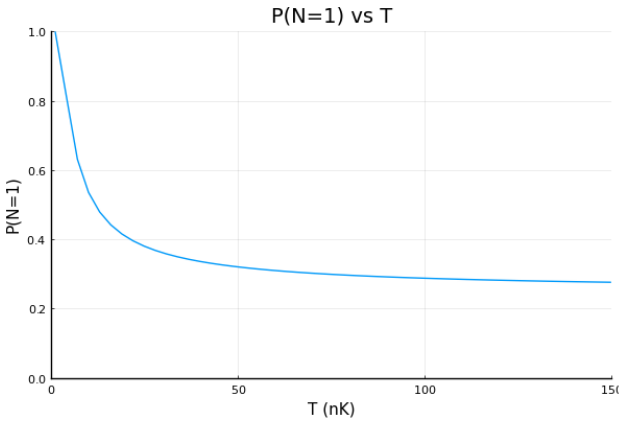

Figure 6.2: The probability of a lattice site containing exactly one Rb atom is plotted as a function of temperature for an $\omega = 2\pi \times 15$ kHz optical lattice, assuming optimized chemical potential μ.

These conditions have been achieved in a Rb atomic gas [241], but require temperatures of a few nanokelvins, which is substantially colder than we have reached in our K-Rb mixture (approximately 40 nK in our crossed dipole trap or 120 nK in our accordion lattice). Even if a sufficiently low temperature were achieved via improved evaporative cooling or adiabatic decompression, to produce a large $N = 1$ region, the chemical potential must be flat across a large area, which is not possible in our current Gaussian beam optical traps for more than a few thousand lattice sites[2] . To avoid these issues, we decided to produce molecules from bulk 2D Bose and Fermi gases instead.

[2] If too much Rb is present, an $N > 1$ region forms at the center of the trap, yielding donut-shaped molecule distributions, which we have observed experimentally.

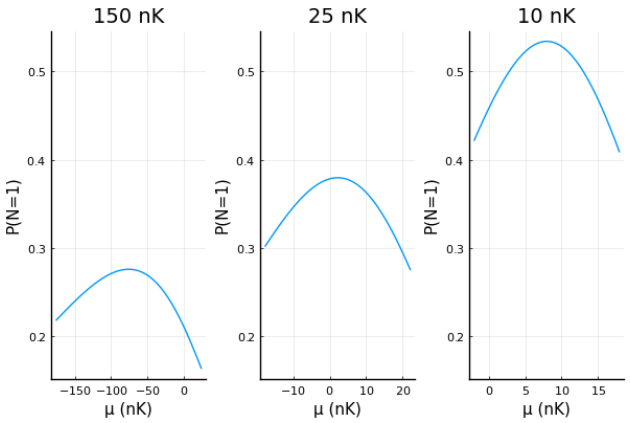

Figure 6.3: The probability of a lattice site containing exactly one Rb atom is plotted as a function of chemical potential for an $\omega = 2\pi \times 15$ kHz optical lattice for three different temperatures.

6.2.2 Production from bulk 2D gases

To produce molecules at high phase space density in a bulk gas, it seems reasonable that both atomic precursors should be cold, dense, and well-overlapped. This intuition is formalized in the stochastic phase space sampling (SPSS) model [242], which states that a molecule forms if atoms are sufficiently close in phase space[3] . Experimentally, this model seemed to describe observations in [95], in which KRb molecules were made from a majority-Rb mixture. The association efficiency was observed to decrease when Rb condensed, reducing the overlap between the mixtures. The model also provided a reasonable description for molecule formation in a majority K mixture [245], although the association efficiency was lower than predicted, although maximized, for deeply degenerate K. In that work, the Rb was thermal, but in [85], a BEC of Rb immersed in a larger K Fermi gas, allowed production of a 3D molecular gas with T/T_F of 0.3. A similar approach allowed production of a 2D Fermi gas with T/T_F as low as 1.5 in [99], which was the highest initial phase space density achieved in 2D until the work discussed in this chapter.

In this section, I discuss considerations for efficient molecule production in quasi-2D (the vertical trap frequency $\omega_y \gg k_B T/\hbar$), including the density profiles and thermodynamics of Bose

[3] More detailed models have also been proposed for association of homonuclear [243] and heteronuclear gases [244].

and Fermi gases. Although I do not discuss it extensively, another viable approach to producing 2D molecular gases may be producing the molecules in 3D, then compressing them and loading them into a 2D layer, using d.c. electric fields [246, 229] or microwaves [247] to shield inelastic collisions.

6.2.2.1 Quasi-2D Bose and Fermi gases at zero temperature

While in the experiment, the finite temperature of the atomic gases affects the association efficiency and temperature of the resulting molecules, understanding their zero-temperature behavior can already elucidate considerations for molecule production. Because the atoms are typically deeply degenerate in our production sequence, their spatial distribution is well-approximated by the zero-temperature distribution, allowing the effect of trap geometry to be studied. We first consider atoms confined by a harmonic potential $V(\mathbf{r}) = \frac{m}{2}(\omega_x^2 x^2 + \omega_y^2 y^2 + \omega_z^2 z^2)$ with trap frequencies $\omega_{x,y,z}^{\mathrm{K,Rb}}$, with $\omega_y \gg \omega_{x,z}$. We use $\omega_r = \sqrt{\omega_x \omega_z}$ to denote the average radial trap frequency.

The spin-polarized potassium atoms interact weakly, since s-wave collisions are forbidden by fermionic statistics [248]. Ignoring K-Rb interactions, we therefore can consider K as a non-interacting Fermi gas, in which the N_K atoms fill the lowest N_K single-particle states. The energy levels are $E(n_x, n_y, n_z) = \hbar(n_x\omega_x + n_y\omega_y + n_z\omega_z)$. As particles are added to the trap, they initially populate only the $n_y = 0$ states, but when $E_F = \hbar\omega_r\sqrt{2N_K} = \hbar\omega_y$, the higher n_y states begin to be populated [84] as well (Fig. 6.4). Because it is desirable to form molecules in the ground band, the higher band atoms are not directly useful for molecule formation. Loading more atoms is still beneficial, as the ground band population continues to increase. Assuming a harmonic trap, we therefore want as high a ratio ω_y/ω_r as possible to maximize the number of K atoms that can be efficiently loaded into the ground band $n_y = 0$.

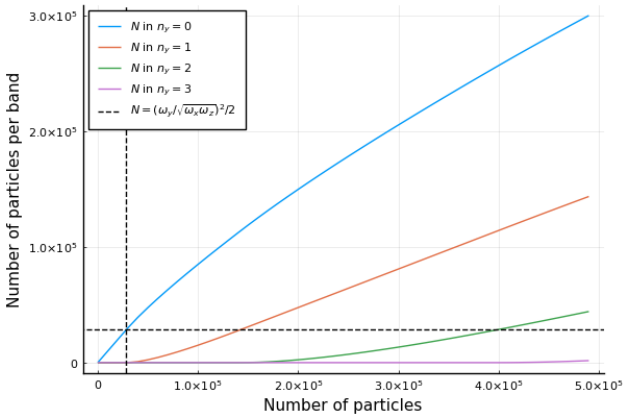

Figure 6.4: As a function of total K population, the number of atoms in each n_y level at $T = 0$ is plotted for typical accordion lattice trap frequencies of $\omega^K_{x,y,z} = 2\pi \times (21, 4239, 15)$ Hz.

We can compute the spatial distribution of the atoms in the ground band under the Thomas-Fermi approximation. Repeating the calculation in [249] in 2D, we find that, for local Fermi wavenumber satisfying $E_F = \frac{\hbar^2 k_F(\mathbf{r})^2}{2m_\mathrm{K}} + V(\mathbf{r})$ and 2D density $n(\mathbf{r}) = \frac{1}{(2\pi)^2}\int_{|\mathbf{k}|<k_F(\mathbf{r})} \mathrm{d}^2k = \frac{k_F(\mathbf{r})^2}{4\pi}$, the density in a harmonic trap is

$$n_\mathrm{K}(\mathbf{r}) = \frac{m_\mathrm{K}}{2\pi\hbar^2}\max\left(0, \hbar\omega_r^\mathbf{K}\sqrt{2N_K^0} - \frac{1}{2}m_\mathrm{K}(\mathbf{r}\omega_r^\mathbf{K})^2\right) \tag{6.7}$$

where N_K^0 is the number of potassium atoms in the $n_y = 0$ state and, for simplicity, we consider a trap isotropic in the x-z plane. Solving for the value of r at which $n = 0$ gives Thomas-Fermi radius

$$r^\mathrm{K}_\mathrm{T-F} = \sqrt{\frac{\sqrt{8N_K}\hbar}{m\omega_r^\mathrm{K}}} \tag{6.8}$$

Treating the bosonic atoms as non-interacting is a poor approximation, as their repulsive interactions make the condensate much larger than the single-particle ground state of the trap. Under the Thomas-Fermi approximation, which is valid for large particle numbers, the density of a BEC is $n(\mathbf{r}) = \frac{\mu - V(r)}{g}$ where, in 3D, the coupling constant $g = \frac{4\pi\hbar^2 a}{m_\mathrm{Rb}}$. In quasi-2D, when the harmonic oscillator length $l \gg$ scattering length a, the condensate can be treated as a 3D

condensate, with the ground state harmonic oscillator wavefunction in the tightly confined direction [250]. For Rb, with $a \approx 100a_0$, this is easily satisfied for our kHz-scale lattice trap frequencies, yielding a coupling constant $g = \frac{2\sqrt{2\pi}\hbar^2}{m_{\mathrm{Rb}}}\frac{a}{l}$. By integrating the density up to the Thomas-Fermi radius $r_{\mathrm{TF}}^{\mathrm{Rb}} = \sqrt{\frac{2\mu}{m_{\mathrm{Rb}}(\omega_r^{\mathrm{Rb}})^2}} = \sqrt[8]{\frac{128}{\pi}}\sqrt{\frac{\hbar}{m_{\mathrm{Rb}}\omega_r^{\mathrm{Rb}}}}\sqrt{\frac{N_{\mathrm{Rb}}a}{l}}$, a relationship between the total number and chemical potential can be found. In terms of the number, the 2D BEC density is

$$n_{\mathrm{Rb}}(\mathbf{r}) = \frac{m_{\mathrm{Rb}}\omega_r^{\mathrm{Rb}}}{\hbar}\sqrt{\frac{l}{2\pi a}}\max\left(0, \sqrt{\frac{N_{\mathrm{Rb}}}{\sqrt{2\pi}}} - \frac{m_{\mathrm{Rb}}\omega_r^{\mathrm{Rb}}\mathbf{r}^2}{4\hbar}\sqrt{\frac{l}{a}}\right) \tag{6.9}$$

To understand the gases' overlap in the mixture, we can compare these distributions. For simplicity, we neglect interactions between K and Rb, which can be tuned between attractive and repulsive using a Feshbach resonance[251]. An example of typical conditions in the accordion lattice is shown in Fig. 6.5 — the peak Rb density is several times higher than the peak K density, and its Thomas-Fermi radius is several times smaller. Both Thomas-Fermi radii have the same scaling $r \propto 1/\sqrt{\omega_r}$, such that changing the horizontal harmonic confinement trap frequency does not improve overlap.

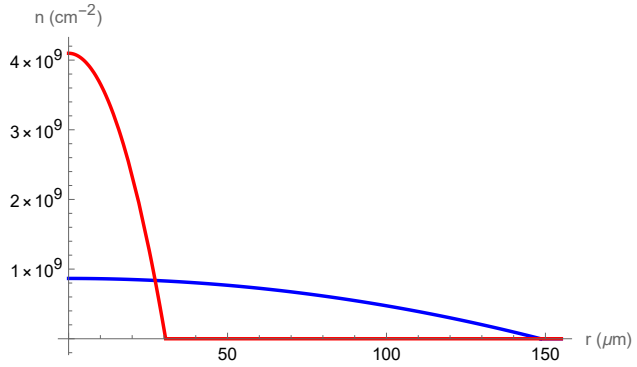

Figure 6.5: The Rb BEC (red) and $n_y = 0$ K (blue) $T = 0$ density distribution plotted for typical accordion lattice trap frequencies of $\omega_{x,y,z}^K = 2\pi \times (21, 4239, 15)$ Hz for 3×10^5 ground band K and 6×10^4 condensed Rb atoms. The figure assumes an isotropic trap in the $x - z$ plane with the geometric mean horizontal trap frequency.

A simple estimate of the maximum number of molecules that can be produced, assuming

perfect association between overlapping atoms, can be found by integrating $\min(n_{\mathrm{K}}, n_{\mathrm{Rb}}) \approx n_{\mathrm{K}}$ from $r = 0$ to $r = r_{\mathrm{TF}}^{\mathrm{Rb}}$. For the conditions in Fig. 6.5, this estimate suggests that around 2.5×10^4 ground band molecules can be produced. The observed molecule production (Sec. 6.4.2) is reasonably well described by the simple model.

6.2.2.2 Effect of trap potential

If the shape of the trap potential is changed, such as in a 3D trap where the different mass-to-polarizability ratios causes K and Rb to sit at different heights, the degree of overlap is modified. In [82], light between 780 and 810 nm (in the vicinity of the D_1 and D_2 transitions for K and Rb) was used to create species-selective traps in an effort to improve the overlap. Unfortunately, the relatively near-detuned light led to increased heating of the atoms and rapid loss of the Feshbach and ground-state molecules. On the KRb apparatus, there is a residual horizontal magnetic field gradient of approximately 0.85 G/cm from imperfections in the coil geometry that causes a relative displacement of the potentials for the different species. This also reduces the association efficiency, since the Rb BEC is displaced from the area with peak K density. By compensating for the magnetic field gradient with either additional coils [252] or an optical potential, the degree of overlap can be improved. In addition, switching from a harmonic to a box potential will significantly improve the overlap (Sec. 6.5.2).

6.2.3 Evaporative cooling

Molecules are produced at a higher entropy per particle than the precursor gases, both because of inefficiencies during association and because the molecules may not immediately occupy a thermal distribution [86]. Even assuming that the molecular gas is at the same temperature as the precursor, 2D T/T_F is increased by a factor of $\sqrt{N_{\mathrm{K}}/N_{\mathrm{KRb}}} \approx 2.5$, for typical numbers of 5×10^4 KRb and 3×10^5 K. In order to reach deep degeneracy, evaporative cooling [5], in which the molecules are allowed to thermalize while the hottest are removed, is likely necessary.

Any method of evaporation can be described by its efficiency, $S_{\mathrm{evap}} = \frac{\partial \log(N)}{\partial \log(T)}$. Assuming

constant S_{evap}[4] and initial number N_0 and temperature T_0, the temperature evolves as

$$T(N) = \left(\frac{N}{N_0}\right)^{\frac{1}{S_{\text{evap}}}} T_0 \tag{6.10}$$

For a two-dimensional Fermi gas in a harmonic trap, $T/T_F = \frac{k_B T}{\hbar\omega_r\sqrt{2N}}$, such that under evaporation, T/T_F becomes

$$\frac{T}{T_F} = \sqrt{\frac{1}{2N}}\frac{k_B T_0}{\hbar\omega_r}\left(\frac{N}{N_0}\right)^{\frac{1}{S_{\text{evap}}}} = \left(\frac{N}{N_0}\right)^{\frac{1}{S_{\text{evap}}}-\frac{1}{2}} \frac{T_0}{T_{F0}} \tag{6.11}$$

Here, we can see that T/T_F decreases if $S_{\text{evap}} < 2$ in 2D ($S_{\text{evap}} < 3$ would yield efficient evaporation in 3D). Efficient evaporative cooling relies on a high ratio of elastic collisions, which redistribute energy between molecules in the sample, to losses due to inelastic collisions or other processes.

6.2.3.1 Collisional shielding and evaporation

The KRb + KRb $\rightarrow$ K_2 + Rb_2 reaction is exothermic [254], and pairs of molecules are rapidly lost when they approach to short range[5] . The loss, which follows the differential equation $\frac{\partial n}{\partial t} = -\beta n^2$, is characterized by the coefficient β. To extend the lifetime of the gas enough to perform efficient evaporative cooling, it is therefore necessary to prevent the molecules from closely approaching each other while maintaining a high rate of elastic collisions. This can be accomplished by engineering long-range dipolar interactions to create a repulsive interaction potential. If the barrier is high compared to the typical collision energies of the gas, tunneling through the potential, thus reactive loss, will be greatly suppressed.

Identical fermions, such as KRb molecules in the same internal state, can only collide with odd relative angular momentum $L = 1, 3, \ldots$. In ultracold systems, collisions predominantly occur

[4] This is a reasonable approximation outside deep degeneracy, but eventually breaks down due to Pauli blocking [253] or technical heating.

[5] Even molecules for which reactions are endothermic, like NaK, undergo relatively fast two-body loss. The mechanism is not fully understood, and may vary molecule-to-molecule, but photoexcitation of long-lived reaction complexes is known to contribute [255].

in the lowest available channel, $L = 1$[6] . This contributes a centrifugal repulsion to the interaction potential [256] (Fig. 6.6), which also includes dipolar and van der Waals interactions

$$V(\mathbf{r}) = \frac{\hbar^2 L(L+1)}{2\mu r^2} - \frac{C_6}{r^6} + V_{\mathrm{dd}}(r) \tag{6.12}$$

where $\mu = m/2$ is the reduced mass. In the absence of dipolar interactions (for instance at zero electric field), KRb molecules with $C_6 = 112 k_B$ K nm^6, have a potential barrier of height $V_b = 24\,\mu$K. The probability of tunneling through the barrier given collision energy E_c scales as $(E_c/V_b)^{L+1/2}$ [256], such that inelastic collisions are significantly suppressed for $k_B T \ll V_b$.

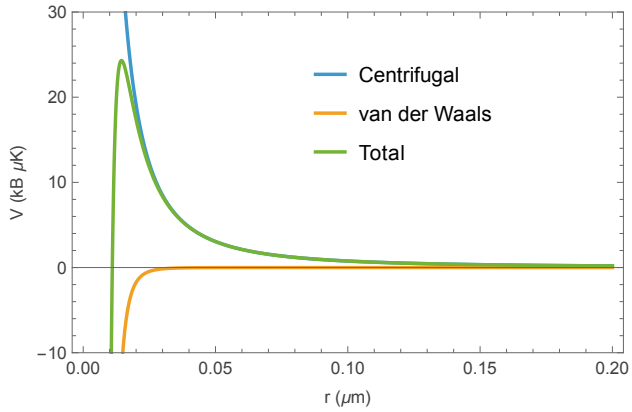

Figure 6.6: The centrifugal, van der Waals, and total potentials are plotted as a function of separation for KRb molecules colliding in the $L = 1$ channel, showing a $24\,\mu$K centrifugal barrier.

However, for head-to-tail collisions between polarized molecules, the dipolar attraction lowers the centrifugal barrier, leading to rapid loss. A variety of methods have been applied to suppressing inelastic collisions while enabling elastic dipolar collisions, as needed for efficient evaporative cooling. Microwave shielding [247], in which a microwave drive induces oscillating dipole moments which, on average, lead to repulsion, was first demonstrated using CaF molecules in optical tweezers [257]. It has since been applied in a multiple experiments [258, 259], enabling evaporative cooling of both Fermi [260] and Bose [221, 222] gases to degeneracy. A related method using optical

[6] This barrier is absent for bosons, which can collide in the $L = 0$ channel. Hence, preparing collisionally stable gases of bosonic molecules is more challenging.

frequencies to connect rotational levels has been proposed but not yet demonstrated [261, 262]. Our group has demonstrated two methods for shielding using d.c. electric fields, discussed in the following paragraphs.

In [246, 229], we demonstrated shielding using an electric field-tuned Förster resonance at which the energy of $|1\rangle$ can be made equal to the average energy of $|0\rangle$ and $|2\rangle$ (Fig. 6.7a). Around the resonance, the dipolar interactions couple a pair of molecules in $|1\rangle$ (with the properly anti-symmetrized state denoted $|11\rangle$) to a state where one molecule is in $|0\rangle$ and the other is in $|2\rangle$ (denoted $|20\rangle$) with matrix element $\langle 11|V_{\rm dd}(r)|02\rangle \propto 1/r^3$, leading to an avoided crossing (Fig. 6.7b). In second order perturbation theory, valid away from the resonance, the energy shift due to the interaction is $V(r) \approx \frac{|\langle 11|V_{\rm dd}(r)|20\rangle|^2}{E_{11}-E_{20}} \propto \frac{r^{-6}}{E_{11}-E_{20}}$. If the molecules are initially prepared in $|1\rangle$ and the electric field is set above (below) the resonance, the p-wave barrier is enhanced (suppressed) by the dipolar interactions (Fig. 6.7c)[7] .

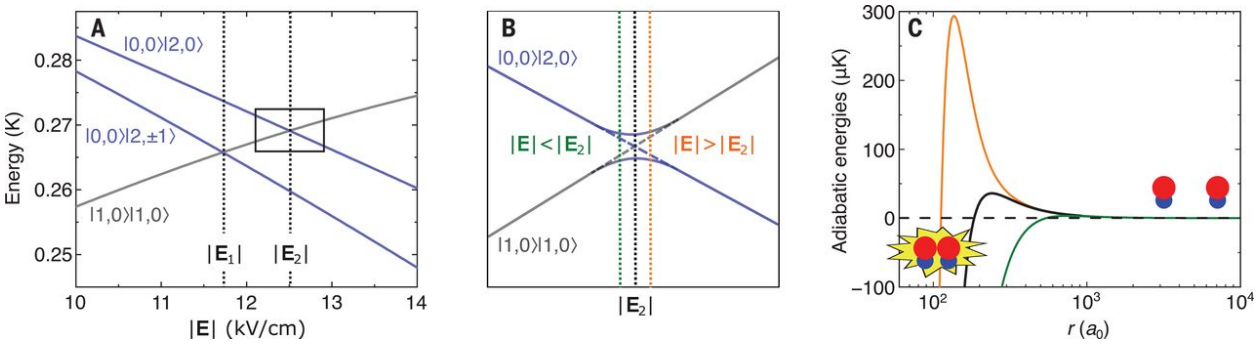

Figure 6.7: (a) The energy of pairs of molecules in $|0,0\rangle\,|2,0\rangle$, $|0,0\rangle\,|2,\pm1\rangle$, and $|1,0\rangle\,|1,0\rangle$ are plotted as a function of electric field. (b) In the vicinity of the Förster resonance, dipolar interactions lead to an avoided crossing. (c) The adiabatic energy of pairs of molecules in $|1,0\rangle\,|1,0\rangle$ colliding in $m_L = \pm1$ are plotted as a function of distance are plotted at electric fields below (12.504 kV/cm; green) and above (12.67 kV/cm; orange) the resonance. The energy without resonant interactions is plotted in black. From [246].

[7] This is a fairly minimal and schematic description of the physics - refer to [246, 229, 84, 83] for more details

Because the energy shift is independent of the sign of the dipolar interactions, the potential barrier is enhanced for both attractive head-to-tail ($m_L = 0$) and repulsive side-to-side ($m_L = \pm 1$) interactions. The shielding is therefore effective even in three dimensions, where β is reduced by an order of magnitude at the optimal field of 12.72 kV/cm [229]. There, $|1\rangle$ has a relatively small induced dipole moment of -0.08 D. Through cross-dimensional thermalization measurements, we were able to characterize elastic dipolar collisions, allowing us to assign an elastic to inelastic collision ratio of $\gamma = 12(1)$ [229]. By reducing the depth of the optical dipole trap containing the molecules, we were able to evaporatively cool the molecules with $S_{\text{evap}} = 1.84(9)$. For other molecules with larger dipole moments, a much larger γ and lower S_{evap} should be possible.

The other method, discussed theoretically in [205, 263, 264], first demonstrated in [265] and improved on in [99], relies on tightly confining the molecules in a layer of an optical lattice in addition to polarizing the molecules using an electric field. This leads to two distinct mechanisms which suppress collisions. For high lattice trap frequencies ω_y, the harmonic oscillator length $a_{\text{ho}} = \sqrt{2\hbar/(m\omega)}$ can be made much smaller than the dipole length $a_D = \frac{m}{2\hbar^2}\frac{d^2}{4\pi\epsilon_0}$. As a result, in the 2D regime, the molecules are only allowed to collide side-to-side, leading to a barrier that monotonically increases with dipole moment [205]. For experimentally accessible trap frequencies of up to $2\pi \times 20$ kHz, the molecules are in the quasi-2D regime, meaning that the harmonic oscillator length $a_{\text{ho}} \gtrapprox 90$ nm is comparable to the dipolar length $a_D < 116$ nm (where we take $d \approx 0.35$ D at 15 kV/cm). In quasi-2D, the collisions are effectively in 3D, but, for identical fermions in the $n_y = 0$ harmonic oscillator level, must occur in the $m_L = \pm 1$ (side-to-side) channel. As d increased to 0.15 D, the height of the barrier increases due to repulsive dipolar interactions, but, for higher d is reduced due to mixing of higher L channels.

When the lattice is deep enough ($\hbar\omega_y > k_B T$) that the ground band is predominantly populated and a dipole moment of $d \approx 0.2$ D is induced by an electric field of 5 kV/cm, β is suppressed by a factor of 5 relative to the zero-field value [99]. The elastic collision rate, which scales as d^4 [205], was measured by cross-dimensional thermalization. The elastic-to-inelastic collision ratio was estimated as $\gamma = \Gamma_{\text{el}}/\Gamma_{\text{in}} = 200(60)$, where the elastic collision rate is $\Gamma_{\text{el}} = \alpha\Gamma_{\text{th}}$, where $\alpha = 8$ [264]

is the number of collisions needed to thermalize, and Γ_{th} and $\Gamma_{\text{in}} = n_0\beta$ are the measured thermalization and inelastic collision rates. By introducing electric field curvature to spill molecules out of the trap, evaporative cooling with a much higher efficiency $S_{\text{evap}} = 1.06(15)$ was demonstrated [99].

Given its high efficiency and compatibility with our desired initial condition of ground-band 2D molecules, the confined evaporation approach seems promising for achieving deep degeneracy. Estimates of final T/T_F, calculated using Eq. 6.11, are plotted as a function of initial N_0 and T for $N = 1000$ (for which the molecule distribution and dynamics should be easily resolvable using our absorption imaging) and $S_{\text{evap}} = 1.09$ [99] in Fig. 6.8, assuming a horizontal trap frequency of $2\pi \times 30$ Hz.

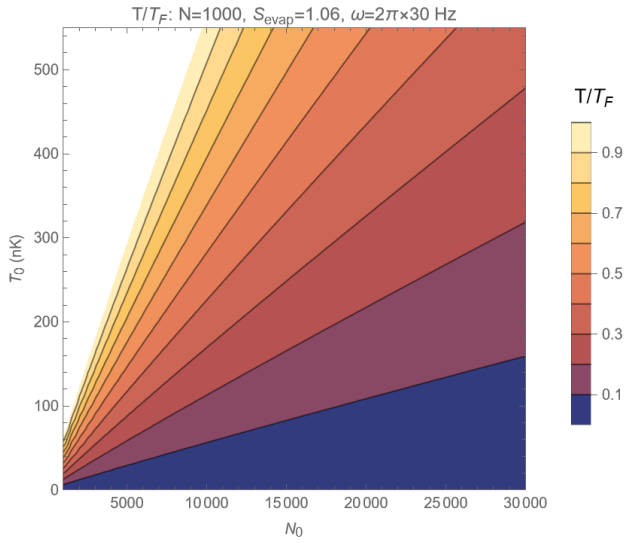

Figure 6.8: The 2D T/T_F in a harmonic trap with $\omega = 2\pi \times 30$ Hz after evaporative cooling to $N = 1000$ with an efficiency of $S_{\text{evap}} = 1.09$ is plotted as a function of initial number N_0 and temperature T_0.

6.2.3.2 Limits on evaporative cooling

A variety of phenomena complicate efficient evaporative cooling to deep degeneracy. For sufficiently high densities and elastic cross-sections, the gas enters the hydrodynamic regime, in

which the mean free path of the molecules is shorter than the dimension of the sample. This reduces the efficiency of evaporative cooling, as only molecules excited to high energies near the edge of the trap will be able to escape without further collisions. As a result, the thermalization rate will be limited to roughly the trap frequency, while inelastic loss rates continue to scale with increasing density [266]. The mean free path is $\ell = 1/(\sqrt{2}n\sigma_{\mathrm{el}})$[8] , where the elastic cross-section is $\sigma_{\mathrm{el}} = (32\pi/15)a_D^2$ at low collision energies [268, 269]. The characteristic size of a harmonically-trapped gas is given by $\sqrt{\langle r^2\rangle} = \sqrt{\frac{k_B T}{m\omega_r^2}}$ for a classical gas or the Thomas-Fermi radius (Eq. 6.8) for a deeply degenerate Fermi gas. When the ratio $\sqrt{\langle r^2\rangle}/\ell \gtrapprox 1$, the gas is in the hydrodynamic regime. For efficient evaporation, the trap frequency ω_r can be reduced. The temperature T scales linearly with ω_r, assuming adiabatic decompression, so $\sqrt{\langle r^2\rangle}/\ell \propto \sqrt{\omega_r}$, allowing the molecules to be brought out of the hydrodynamic regime.

Another effect that limits evaporation efficiency in a degenerate is Pauli blocking. Because collisions can only scatter fermions into unoccupied states, the rate of elastic collisions tends to zero as T/T_F is decreased, and fewer holes are present in the Fermi sea. However, inelastic collisions can proceed unimpeded, as the reaction products are scattered into free space. As a result, as the gas is cooled below the Fermi temperature, the evaporative cooling efficiency is decreased [253]. Technical heating, such as loss from light scattering or collisions with background gas atoms, will also knock holes in the Fermi sea, eventually limiting the coldest achievable temperatures [270].

6.3 Accordion lattice design and construction

To prepare a 2D gas, we need to compress the atoms from the crossed optical dipole trap to a geometry where $\hbar\omega_y \gg k_B T$. Our vertical lattice easily meets that requirement, but the cloud subdivided into roughly 19 layers [117] if the lattice is directly loaded from the xODT. This limits the number of atoms, thus molecules, prepared in any single layer, and requires layer selection [105] to prepare an isolated layer. In 2020, the group built a large spacing lattice (LSL) [99, 84], to

[8] The factor of $\sqrt{2}$ occurs because both particles involved in a collision are moving with uncorrelated velocity, increasing the rate of collisions relative to stationary particles [267].

provide an intermediate trap allowing compression from the xODT to fewer vertical lattice layers. The LSL, with 8 μm spacing, was able to load all the Rb and about half the K to a single layer, and compress the atoms such that the Rb was loaded into around 5 vertical lattice layers. Loading atoms into the vertical lattice from the LSL before producing and evaporatively cooling molecules yielded a 2D degenerate Fermi gas of molecules at $T \approx 0.6\ T_F$ [99].

In order to reach higher phase space densities and produce isolated 2D systems, we wanted to load all the atoms into a single vertical lattice layer. To do so, we developed a replacement for the LSL, the accordion lattice. In this section, I discuss the optical design and characterization of the accordion lattice. In Sec. 6.4, I discuss its performance in compressing atoms toward a quasi-2D geometry, and the subsequent production of molecules.

We consider the interference of two Gaussian beams, each with power P and waist $w_{x,y}$, with wavelength λ at half-angle θ from the $+z$ axis in the $y-z$ plane. As discussed in Sec. 3.3.1, the interference fringes are spaced in the y direction by $a = \frac{\lambda}{2\sin(\theta)}$. Assuming the region of intersection between the beams is short compared to their Rayleigh range, a particle of mass m and polarizability α at the center of the beams experiences trap frequencies

$$\omega_{x,y,z} = 4\sqrt{\frac{-\alpha P}{\pi m w_x w_y}}\left\{\frac{1}{w_x}, \sqrt{\frac{1}{w_y^2} - \frac{\lambda^2}{4a^2 w_y^2} + \frac{\pi^2}{2a^2}}, \frac{\lambda}{2a w_y}\right\}. \tag{6.13}$$

Several desiderata let us determine optimal parameters for the accordion lattice design. Because we already had an operational laser system with sufficient spare power at 1064 nm, and know that both atoms and molecules have low scattering rates [100] and sufficient polarizability [84] at that wavelength, we set $\lambda = 1064$ nm. To load all the atoms into a single layer, we need a to be larger than the size of the atom distribution in the xODT. The characteristic vertical size of the K Fermi gas, which is larger than the Rb BEC, is the Thomas-Fermi radius [271] $R_y = a_{\mathrm{ho}}(48N)^{1/6}\frac{\omega_{\mathrm{ho}}}{\omega_y}$ where the harmonic oscillator length is $a_{\mathrm{ho}} = \sqrt{\frac{\hbar}{m\omega_{\mathrm{ho}}}}$ and $\omega_{\mathrm{ho}} = \sqrt[3]{\omega_x\omega_y\omega_z}$. For $N = 4\times10^5$ K in the xODT with $\omega_{\mathrm{xODT}} = 2\pi\times(40, 270, 40)$ Hz, $R_y = 8.4\,\mu$m. This means that $a_{\max}$ must be at least $2R_y = 8.4\,\mu$m, so $\theta_{\min}$ must be at most 1.8°. Because Rb has a higher mass and lower

polarizability than K, gravity makes the equilibrium position of the Rb atoms a few microns lower than that of the K atoms in the xODT. This means a slightly larger $a_{\max}$ is needed to load both species in the same layer. In practice, we find that both species are reliably loaded into the same layer at $a = 14\,\mu$m.

Other factors make a smaller a desirable. A high vertical trap frequency is required to compress the atomic gas enough that only a single vertical lattice layer is loaded (or to generate a quasi-2D molecular gas directly in the accordion lattice). Assuming that the lattice is able to reach the quasi-2D regime $\hbar\omega_y > k_B T$, the distribution of the ground state in the vertical direction is Gaussian with $\sigma_y = \sqrt{\frac{\hbar}{2m\omega_y}}$. To load a large fraction of the atoms into a single layer of the $a_{\mathrm{VLatt}} = 540\,$nm vertical lattice, $4\sigma_y \lessapprox a_{\mathrm{VLatt}}$. For a given P and $w_{x,y}$, ω_y scales as $1/a$ and σ_y as $\sqrt{1/a}$ in the realistic limit that $w_y \gg a, \lambda$. Therefore, for a given beam waist, a smaller $a_{\min}$ results in less power being needed to load a single vertical lattice layer.

In our apparatus, θ is limited to roughly 16° by the windows on the cell, corresponding to $a_{\min} = 1.9\,\mu$m. A further constraint comes from the numerical aperture of the final focusing lens. We selected a 75 mm diameter, $f = 150$ mm asphere to replace a 50 mm diameter, $f = 150$ mm achromat used for the previous LSL. This lens's clear radius of 34.5 mm allows for $a_{\min}$ up to $2.4\,\mu$m. In practice, the size of the beams reduces their maximum spacing on the lens, giving $a_{\min} \approx 2.8\,\mu$m.

The size of the beams $w_{x,y}$ should be as large as possible, subject to power limitations. This maximizes the capacity of fermions in the ground band (Sec. 6.2.2.1) and suppresses three-body loss by reducing density. Perhaps more importantly, larger beams reduce adiabatic heating as the atoms are compressed. The molecules generally inherit their temperature from the atoms [86], and lower temperatures enhance the efficiency of evaporative cooling (Sec. 6.2.3). We picked $w_x \approx 250$ μm, which allows several kilohertz trap frequencies with hundreds of milliwatts of power. A larger size would improve performance and would be a worthwhile upgrade in the future (Sec. 6.5.1).

Finally, we would like roughly equal confinement along the x and z directions at the minimum lattice spacing to enable efficient loading into the round vertical lattice. This is achieved for

$\frac{w_y}{w_x} = \frac{2a_{\mathrm{min}}}{\lambda} = 5.26$. We use a 4:1 telescope constructed from $f = -25$ mm and $f = 100$ mm cylindrical lenses to increase the vertical size of the lattice beams, so they focus to a smaller waist at the position of the atoms. We measure waists $w_{x,y} = 253$ and $68\,\mu$m, respectively, resulting in a ratio $\frac{\omega_x}{\omega_z} = 1.4$ at $a = a_{\mathrm{min}}$. As a is increased, ω_x remains constant while ω_z increases. If necessary, the roundness of the trap can be maintained by using one of the xODT beams to provide extra confinement in the z direction.

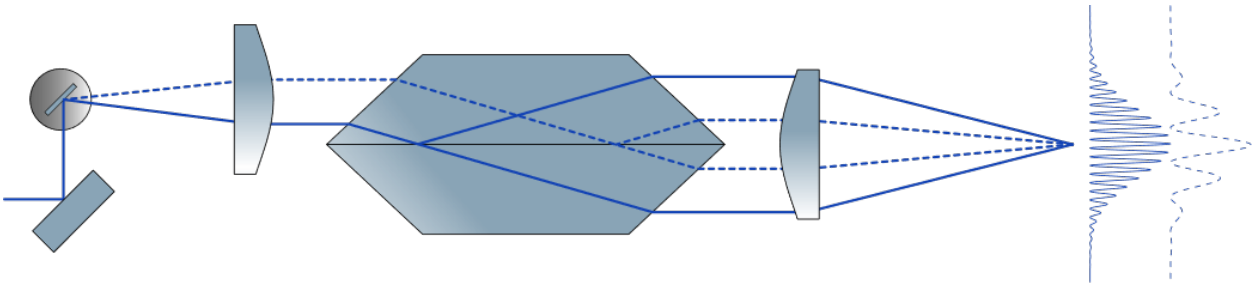

Figure 6.9: The key elements of our accordion lattice, including a mirror mounted to a galvanometer, a beamsplitter made from a pair of dove prisms, and a focusing lens are shown schematically. Beam paths and resulting lattices are drawn for large and small spacing configurations.

With the geometry of the beams established, we can consider the design of a system that enables the lattice spacing to be tuned between a_{min} and a_{max}. It is important that the phase of the lattice is stable, both shot-to-shot and as a is varied, and well-controlled to provide repeatable positioning of the lattice layers and avoid heating from shaking the atoms during loading and compression. To maximize robustness to temperature changes, drifts of alignment, and mechanical vibration, we wished to use common optics for both beams and, further, match their optical path lengths such that the relative phase is insensitive to common-mode drifts [272, 118]. This requirement was not met by the beamsplitter used for the previous LSL, which consisted of two stacked polarizing beamsplitter cubes (similar to the system described in [273]). Instead, we opted to use a beamsplitter constructed from a pair of dove prisms glued together with a beamsplitter coating at the interface (Fig. 6.9). This approach, based on designs from the erbium experiment in Markus

Greiner's group, matches the optical path lengths and, being a monolithic assembly, provides excellent long-term stability. We followed their procedures described in [272] to interferometrically align and glue the prisms[9] . After gluing, we found that $r = 62\%$ of the light was reflected at the interface, such that the contrast of the fringes is $2\sqrt{r(1-r)} = 0.97$ [272].

To control a, we need to vary the separation of the beams after the beamsplitter by adjusting the height of the incoming beam. The angle of the beam must be kept constant to prevent changes in the pointing of the lattice. In the Greiner group, this was accomplished by rotating a large periscope with a galvanometer. With this approach, the angle can be well-controlled if the periscope mirrors are parallel, which they achieved with interferometric alignment. Because we were unable to source a galvanometer with sufficient torque to quickly rotate a periscope of the required size, we instead opted to translate the beam using a mirror rotated by a smaller galvanometer[10] at the focus of a lens. To avoid shifts in the angle of the beam as it is translated, it is important to use a diffraction-limited aspheric lens. As the galvo was scanned over its range, the beam angle varied by 0.004° when the diffraction-limited Thorlabs AL50100H lens was used, but 0.02° with a CNC-polished Thorlabs AL50100 lens. For the same reason, we needed to use diffraction-limited aspheres for the telescope after the beamsplitter and the final focusing lens and carefully optimize their position and angle.

Errors in alignment of the galvanometer mirror can also shift the position of the beam away from the focal plane of the lens, changing the angle of the output beam as the mirror is rotated. We included an adjustable mirror before the galvanometer mirror so that the incoming beam can be aligned to the galvanometer's axis of rotation. However, we found that the axial position of the intersection of the lattice beams varied by roughly $20\,\mu$m as the angle of the galvanometer was tuned, even when the pointing was optimized. We realized that the mirror's surface was offset by 0.475 mm from the galvanometer's axis of rotation, which we confirmed could cause the observed shift using a ray-tracing model implemented with [274] (Fig. 6.10a). To fix this, we designed a new

[9] Thorlabs PS993 with custom anti-reflective coatings on the end faces and beamsplitter coatings at the interface from Optical Filter Source glued with Norland NOA61 optical adhesive

[10] Thorlabs GVS001

mirror mount for the galvanometer that held the mirror surface coplanar with the axis of rotation (Fig. 6.10b).

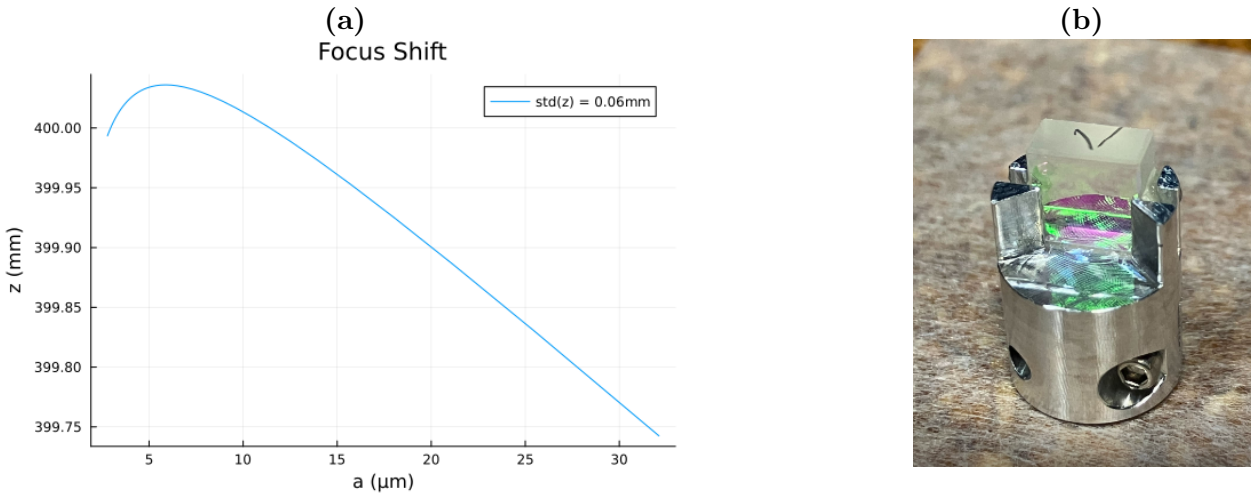

Figure 6.10: (a) A ray-tracing simulation shows the axial shift of the accordion lattice focus as the spacing galvanometer is tuned due to a 0.475 mm offset between the galvanometer mirror surface and axis of rotation. (b) A custom mount for attaching an Edmund Optics #37-558 5 mm square mirror to a Thorlabs GVS001 galvanometer, with the mirror surface coplanar with the axis of rotation.

To characterize the performance of the lattice, we installed a camera and lens to image the plane where the atoms would be. By fitting images of the lattice (Fig. 6.11), we could measure its spacing and phase as the spacing galvanometer is scanned. Over the full range of a needed for the experiment, the phase of the center fringe is stable within π radians, with a highly repeatable profile scan-to-scan. We are therefore able to use feedforward to further improve the phase stability. To enable adjustment of the relative phase of the beams, we insert a galvanometer-mounted glass plate with an anti-reflective coating in the upper beam (and an identical fixed plate in the lower beam). As the galvanometer rotates the plate[11] , which is angled around 10°, the phase of the fringes changes by 10.65 rad/°. By setting the phase galvanometer appropriately for each spacing,

[11] a narrow strip cut from Thorlabs WG41010R-C on a GVS001 galvo

we are able to cancel the phase shifts, keeping the lattice's phase steady within 0.2 radians (Fig. 6.12). We also measured the long-term stability of the lattice phase, finding drifts of less than 0.2 radians over a day, outside the temperature controlled optics table.

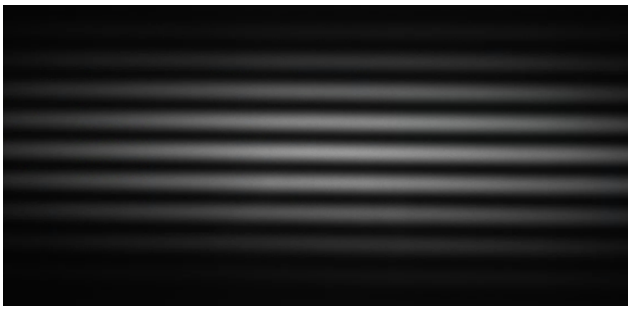

Figure 6.11: The fringes of the accordion lattice, here at a relatively large spacing, are imaged onto a camera.

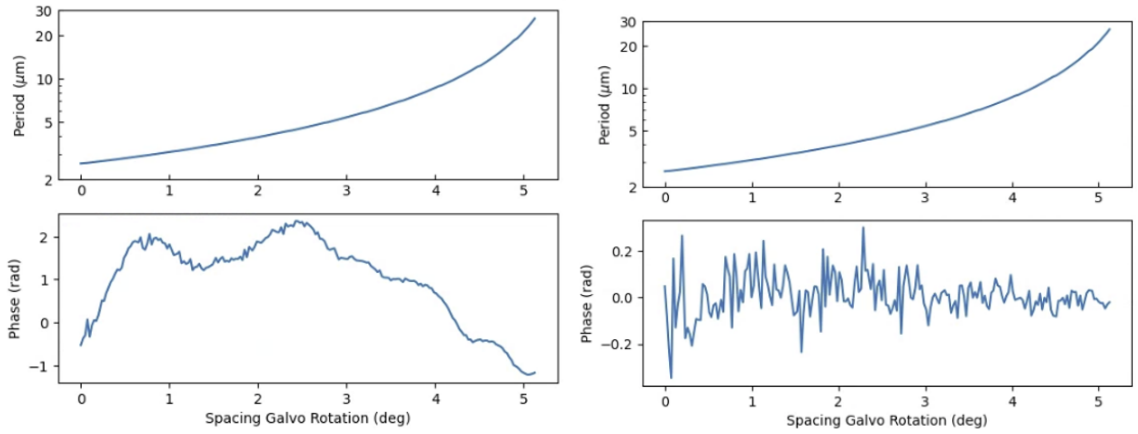

Figure 6.12: The phase and spacing of the accordion lattice, measured using a camera, are plotted versus the angle of the spacing adjustment galvanometer, without (left) and with (right) phase feedforward.

The accordion lattice beams are combined with the plug light, one of the xODT beams, and the axial imaging path using a D-shaped mirror before being focused onto the atoms. To avoid horizontal fringes on the accordion lattice, it was critical to ensure that multiple reflections from

the various optics were blocked. The layout of the accordion lattice optics is shown in Fig. 6.13.

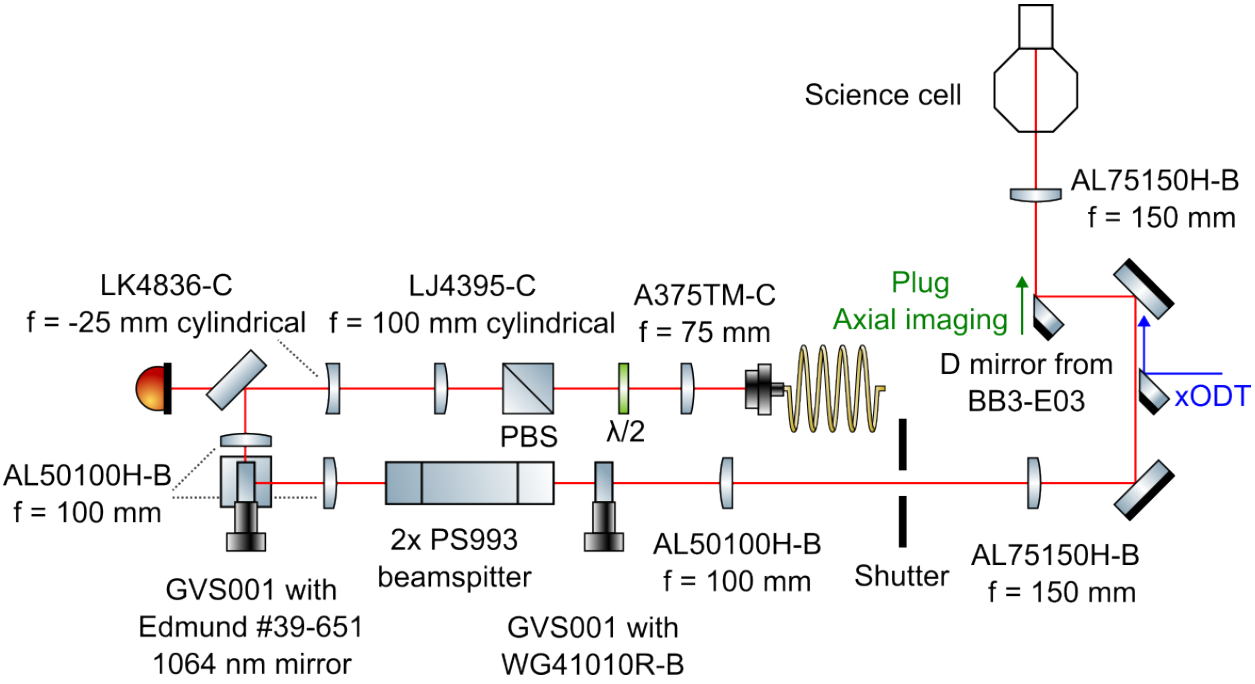

Figure 6.13: The layout of the accordion lattice optics on optical table is shown schematically. A side view, showing the operation of the spacing adjustment galvo and the beamsplitter, is shown in Fig. 6.9. The optics symbols are adapted from [106].

6.4 Accordion lattice experiments

In this section, I discuss preliminary experiments in the accordion lattice. In Sec. 6.4.1, I demonstrate that we can effectively load and compress atoms. In Sec. 6.4.2, I discuss producing molecules directly in the accordion lattice, where we were able to create degenerate Fermi gases approaching the quasi-2D regime. Finally, in Sec. 6.4.3, I discuss loading the atoms from the accordion lattice to the vertical lattice and producing molecules there.

6.4.1 Loading and compressing atoms

We load atoms into the accordion lattice after evaporation in the optical dipole trap by ramping the accordion lattice power to 400 mW, corresponding to $\omega_y = 2\pi \times 870$ Hz for Rb. With a 14 μm spacing, we are able to load all the atoms into a single layer. We then compress the accordion lattice in stages to 2.8 μm spacing while ramping off the xODT. We optimized the duration of each stage to minimize heating and number loss, finding a total duration of approximately 6 seconds works well. After compression, $\omega_{x,y,z} \approx 2\pi \times (22, 4300, 15)$ Hz for Rb.

During initial testing, we found that the horizontal magnetic field gradient (Sec. 6.2.2.2) was strong enough to pull K atoms out of the trap, causing significant loss during compression. We added a 1064 nm beam offset from the center of the accordion lattice to cancel the force with an optical potential gradient, keeping the atoms centered in the lattice. This compensating potential will be described in more detail in Annie Carroll's forthcoming thesis. After the beam was added, the optimized compression sequence caused little loss of atoms, yielding approximately 5×10^5 K and 5×10^4 Rb at 200 nK (Fig. 6.14), slightly hotter than what would be expected from purely adiabatic compression.

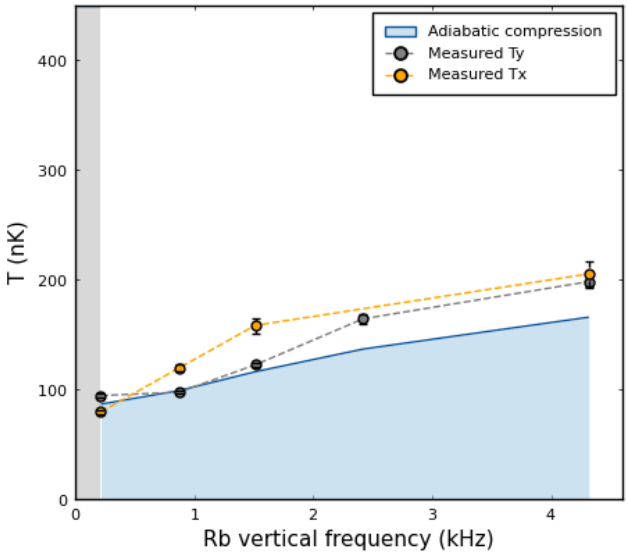

Figure 6.14: The temperature of the K-Rb mixture, as measured by a Gaussian fit to the non-condensed component of the Rb after time-of-flight expansion [48], is plotted as a function of the vertical trap frequency as the accordion lattice is compressed. The blue line indicates the expected minimum temperature given adiabatic compression, calculated for a noninteracting Bose-Fermi mixture.

We also tried evaporatively cooling the atoms in the accordion lattice in order to counteract the temperature increase during compression. Colder atoms would allow production of initially colder molecules with more favorable inelastic collision rates (Sec. 6.2.3.1) and higher ground band population. Unfortunately, evaporation by reducing the accordion lattice power after compression was not particularly efficient, with $S_{\mathrm{evap}} \approx 2$ for K. Alternative evaporation protocols, such as shaping the trap potential to improve thermalization rates or applying a vertical magnetic field gradient to spill hotter atoms [275] may yield more favorable results.

6.4.2 Molecules in the accordion lattice

After preparing the atomic mixture in the accordion lattice, we ramp the magnetic field across the Feshbach resonance to produce KRb* Feshbach molecules. We found that the resulting molecule number depends sensitively on the ramp rate, with up to 5.3×10^4 produced at a ramp

rate of 5 G/ms. This is faster than the optimal rate in the xODT in [86], likely because the higher density in the accordion lattice reduces the Feshbach molecule lifetime. Almost all the Rb was associated, with only a few thousand thermal atoms remaining. Based on time-of-flight expansion of the Feshbach molecules, with the wings of the cloud fit to a Gaussian profile [49], we estimated a temperature of approximately 310 nK.

The trap frequencies for KRb* are $\omega_{x,y,z} = 2\pi \times (27.6, 5200, 26)$ Hz, such that $\hbar\omega_y/k_B = 250$ nK. Since T exceeds the level spacing, the molecules are not quasi-2D – assuming a Boltzmann distribution predicts that around 55% are in the $n_y = 0$ level. For 5.3×10^4 molecules, the 3D Fermi temperature is 508 nK, so the Feshbach molecules are at $T/T_F^{3D} \approx 0.7$. A Gaussian fit to the wings of the gas (Fig. 6.15) after release from the lattice overestimates the central density [85, 49], further suggesting that the gas is Fermi degenerate.

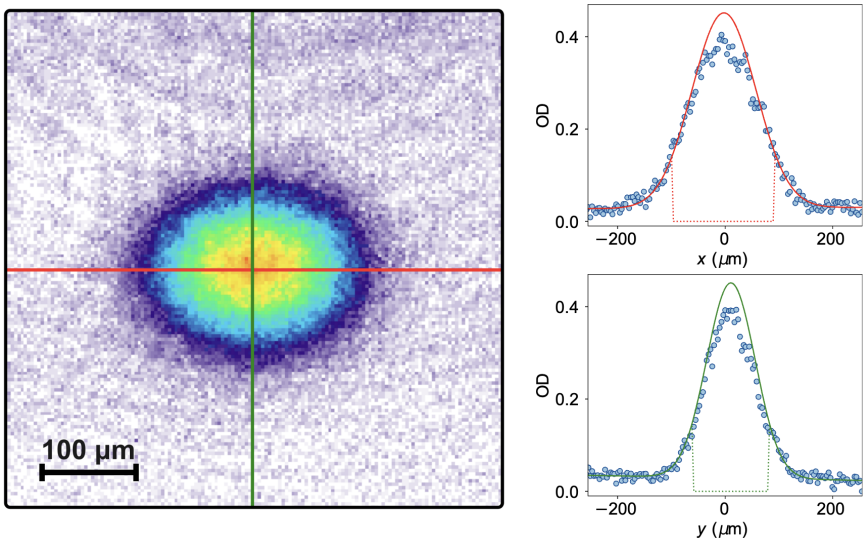

Figure 6.15: An absorption image of the Feshbach molecules after time-of-flight expansion is shown, along with the profiles of the gas along the horizontal (red; above) and vertical (green; below) axes. A Gaussian fit (solid lines) excluding a 1.5 σ central region overestimates the central density, suggesting the gas is degenerate.

If the KRb* in this condition are transferred to the ground state, evaporation using resonant

shielding (Sec. 6.2.3.1) may be a viable path to producing a degenerate quasi-2D gas, as a quasi-2D initial condition is not required. Per Eq. 6.11, a 2D T/T_F of 0.68(23) could be achieved for 1000 remaining molecules, assuming 90% STIRAP efficiency and $S_{\text{evap}} = 1.84(9)$ [229]. If the elastic-to-inelastic collision ratio improves as the gas is cooled, or the evaporation is switched to the more efficient confined-geometry approach once a quasi-2D condition is attained, deeper degeneracy could be reached.

6.4.3 Molecules in the vertical lattice

We have also explored loading atoms into the vertical lattice from the compressed accordion lattice. After ramping the accordion lattice power to 1200 mW, reaching a vertical trap frequency of 7.5 kHz for Rb, we loaded the atoms into a 60 E_r vertical lattice and produced approximately 4000 ground state molecules in the combined trap. Using gradient spectroscopy[12] (Sec. 3.2.3), we found that the molecules primarily occupied one layer, with some population in a second (Fig. 6.16). Using Kapitza-Dirac diffraction of a BEC [277], we measured a 0.32(12) degree tilt between the **k**-vectors of the lattices. This tilt, combined with the spatial extent of the Rb BEC, leads to atoms in the second layer. By compressing the atoms using the xODT, we were able to load a single layer at the cost of increased temperature.

We observed that the phase of the accordion lattice drifts relative to the phase of the vertical lattice on a timescale of roughly an hour, leading to changes in which vertical lattice layer was loaded. As a result of this drift, which likely originates from thermal expansion changing the accordion lattice pointing or the vertical lattice position, the accordion lattice phase will need to be stabilized. Given the slow rate of drift, low-bandwidth feedback control based on periodically imaging the atoms' layer distribution should be sufficient.

Work on optimizing loading and evaporative cooling in a single vertical lattice layer is ongoing and will be described in Annie Carroll's thesis.

[12] We subsequently set up a simpler sequence for layer-resolved imaging, allowing measurement of the layer distribution with a single experimental shot. There, we magnify the layers by evolving for a quarter period in the accordion lattice potential and imaging after time-of-flight, as in [99, 276].

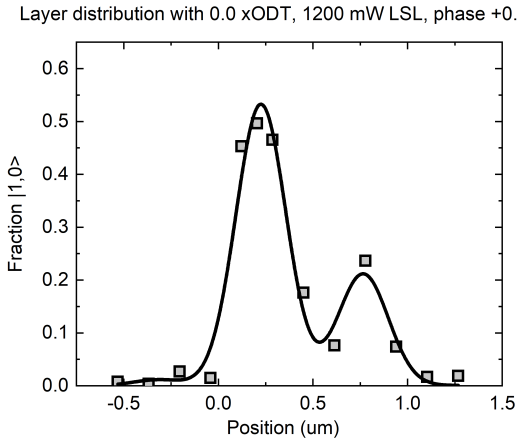

Figure 6.16: The population distribution of molecules in the vertical lattice following loading from the compressed accordion lattice is measured using layer-resolved gradient spectroscopy (Sec. 3.2.3).

6.5 Outlook

Combining the best molecule number and phase space density we have produced in the accordion lattice with evaporative cooling at the efficiency demonstrated in [99] would allow production of deeply degenerate quasi-2D Fermi gases. Currently, these conditions are difficult to simultaneously achieve. This section presents some possible modifications to the apparatus and experimental sequence that could improve molecule production and cooling, helping realize a long-standing goal of the ultracold molecule community.

6.5.1 Evaporating molecules in the accordion lattice

It would be appealing to directly evaporate the molecules in the accordion lattice rather than loading the atoms and producing molecules in the vertical lattice. Controlling the relative phase of the lattices sufficiently well to load a single layer every shot is challenging, transferring between traps causes heating, and distortion from the ITO-coated electrodes causes defects in the vertical lattice potential. In addition, the accordion lattice polarization could be tuned to the magic angle (Sec. 3.3.2.1) for arbitrary electric field directions, facilitating spin physics experiments. It is

difficult to attain sufficiently low initial temperatures and high vertical trap frequencies to produce quasi-2D molecules in the current accordion lattice geometry. However, increasing the beam sizes or adding a compensating potential to reduce the horizontal trap frequencies (Sec. 6.5.2) could allow for efficient evaporation directly in the accordion lattice.

Currently, the ratio of horizontal ω_r to vertical trap frequency ω_y in the compressed accordion lattice is approximately 240:1. If the same ω_y is maintained but beams comprising the lattice are scaled by a factor s, ω_r scales by $1/s$ and the required optical power scales as s^2. Now, around 5 W of power are required to match the $\omega_y = 2\pi \times 17$ kHz trap frequency used for evaporation in [99]. The photonic crystal fibers we use to deliver light to the accordion lattice can handle roughly 20 W of optical power [278], so the beams could be scaled up by a factor of 2 (although other components along the optical path may need to be upgraded to handle the increased power). The resulting ratio $\omega_y/\omega_r \approx 120$ is similar to that of the combined vertical lattice and xODT potential in [99].

One potential concern for evaporative cooling in the accordion lattice is a reduction in molecule lifetime due to an increased light intensity I. KRb has a one-body lifetime $\tau = 1/(\alpha_{\text{im}} I)$ where $\alpha_{\text{im}} = 2\pi \times 2.052(9) \times 10^{-12} \frac{\text{MHz}}{\text{W/cm}^2}$ for KRb at 1064 nm [100] and I is the intensity of the light. For a trap frequency ω, the peak intensity of an optical lattice is $I = \frac{m\omega^2 a^2}{2\pi^2 \alpha}$, so the lifetime scales as $1/a^2$. As a result, scattering rates in the compressed 2.8 μm LSL are 27 times higher than in the vertical lattice at the same vertical trap frequency. While this scattering is unimportant for some experimental sequences, for instance if the atoms are to be loaded into another lattice before molecule production, it can limit others, such as evaporative cooling of molecules directly in the accordion lattice. For $\omega_y = 2\pi \times 17$ kHz, the molecule lifetime would be 3 s in the $a = 2.8\,\mu$m accordion lattice versus 80 s in the $a = 540$ nm vertical lattice.

Fortunately, it may not be necessary to use such a high trap frequency for efficient evaporative cooling, such that a longer lifetime is possible – the lattice need only be deep enough that almost all the molecules occupy the ground band (Sec. 6.2.3.1). However, this is a somewhat challenging condition to satisfy. The initial temperature, which scales as $T \propto (\omega_y \omega_r^2)^{1/3}$ for adiabatic

compression, could be reduced from 310 nK (Sec. 6.4.2) to 195 nK by increasing the size of the accordion lattice beams by a factor of 2 at $\omega_y = 2\pi \times 5200$ kHz. This would give a ground band fraction of 72 %, assuming a Boltzmann distribution, which is likely insufficient for efficient cooling. As such, producing molecules at lower temperature, through improved evaporative cooling of the atomic precursors (Sec. 6.4.1), pre-cooling of the molecules using resonant shielding (Sec. 6.2.3.1) or further adiabatic decompression in an appropriately shaped trap potential (Sec. 6.5.2) is likely required to produce a ground-band sample in the accordion lattice. Ongoing efforts in the lab are exploring these directions.

6.5.2 Molecule production in a box trap

One promising direction for improving molecule production and evaporation is improving control of the optical potentials. In particular, confining the atomic and molecular gases in a region of uniform potential with sharp walls, known as a box trap [279], offers multiple advantages. Unlike in a harmonic potential (Sec. 6.2.2.1), bosons and fermions both take on uniform density distributions in a uniform potential. The improved overlap will increase the rate of thermalization between the Bose and Fermi gases, enhance association efficiency[13] and result in Feshbach molecules already occupying an equilibrium spatial distribution after association. The molecule production process can be further optimized by varying the size of the box trap to tune the density and temperature of the atomic precursors to maximize association efficiency and minimize three-body loss.

A box potential can also improve evaporative cooling, as it allows the density of the gas to be tuned independently of the depth of the trap, which has been shown to enhance cooling efficiency with atoms [281]. By expanding the box, the temperature of the gas can be reduced, which enhances the elastic to inelastic collision ratio (Sec. 6.2.3), and the density reduced, preventing the onset of hydrodynamics which limit cooling efficiency (Sec. 6.2.3.2). Further, inelastic collisions in a uniform

[13] In preliminary work [280], the MPQ group was able to increase NaK* number by 80% by producing molecules in a 3D box potential.

potential reduce the average energy of the remaining gas, as opposed to 2D (3D) harmonic traps where the average energy is constant (increased) [264]. Finally, a uniform molecule distribution is advantageous for future many-body physics experiments, as dynamics or phases can be explored in a homogenous system, rather than averaged over regions of different density in a harmonic trap.

The different mass-to-polarizability ratios of K and Rb at 1064 nm complicates construction of a three-dimensional box trap, as both species must be simultaneously levitated. This can be accomplished using a magnetic field gradient or a near-detuned trapping wavelength such that the ratios match. Both approaches complicate molecule production, since KRb has negligible magnetic dipole moment, and large imaginary polarizability near the K and Rb D lines [152]. A two-dimensional box, however, can use a one-dimensional lattice to tightly confine both species in the vertical direction [215]. In this case, only the horizontal potential needs to be homogenized.

One option for producing a 2D box is to compensate the lattice's harmonic potential with a shaped beam from the vertical direction [282, 22], as discussed in [82] for the KRb experiment. Given the large feature size, a digital micromirror device (DMD) in an image plane would allow projection of a tunable potential with sufficient resolution and intensity granularity [283]. If light around 1064 nm[14] was used with the DMD, the lattice potential could be simultaneously compensated for all species and low imaginary polarizability would support long molecule lifetimes. In addition to providing uniform trap potentials, a DMD would allow local initialization of rotational states, as recently demonstrated with RbCs molecules in [192]. However, aspects of the design of the KRb apparatus make vertical projection of high-quality potentials challenging. The light would have to pass through the ITO coating on the electrodes, which would lead to distortion and limit the possible intensity. More critically, a dichroic mounted between the objective and cell, used to create the vertical lattice (Sec. 2.2.1), would block light projected through the objective or reflect light incident from the top. If the accordion lattice was used as the primary vertical confining

[14] Spectrally-broad light generated with a superluminescent diode (SLD) [284, 22] would be beneficial for this application, as the short coherence length suppresses interference fringes. We tested seeding a Nufern fiber amplifier with an Innolume SLD1064020PM300MFLXX SLD, and found that the amplifier did not distort the SLD's spectrum and showed similar intensity noise to our standard Mephisto seed.

potential (Sec. 6.5.1), the dichroic could be removed.

An alternative would be to compensate the lattice potential using shaped beams from the side and axial directions. The beams could be used to create a flat region with tunable size (Fig. 6.17). This approach would further allow making adjustable optical traps which could improve the efficiency of loading and evaporative cooling atoms [281, 285, 286]. The beams could be shaped using either acousto-optical deflectors (AODs) [287] or DMDs. As compared to DMDs, AODs would offer improved power efficiency and support operation at higher power, which would be important if the shaped beam replaced the current optical dipole traps, but have the potential to cause extra heating due to beating between different parallel tones or the scanning of a beam used to create a painted potential. The painting approach is more common in the quantum gas literature [281, 285, 286] and could be controlled with the same AWG system used for RF synthesis (Sec. 2.2.3). However, modulation of the trap at kilohertz or tens of kilohertz frequencies would cause heating in optical lattices. Frequency domain multiplexing causes megahertz-scale beating between adjacent beams [287], which is much higher than lattice trap frequencies, so should cause less heating. The waveform for driving the AODs can be generated with the same DDS electronics used by optical tweezer experiments, such as the "Gigamoog" synthesizer from the Kaufman group [118].

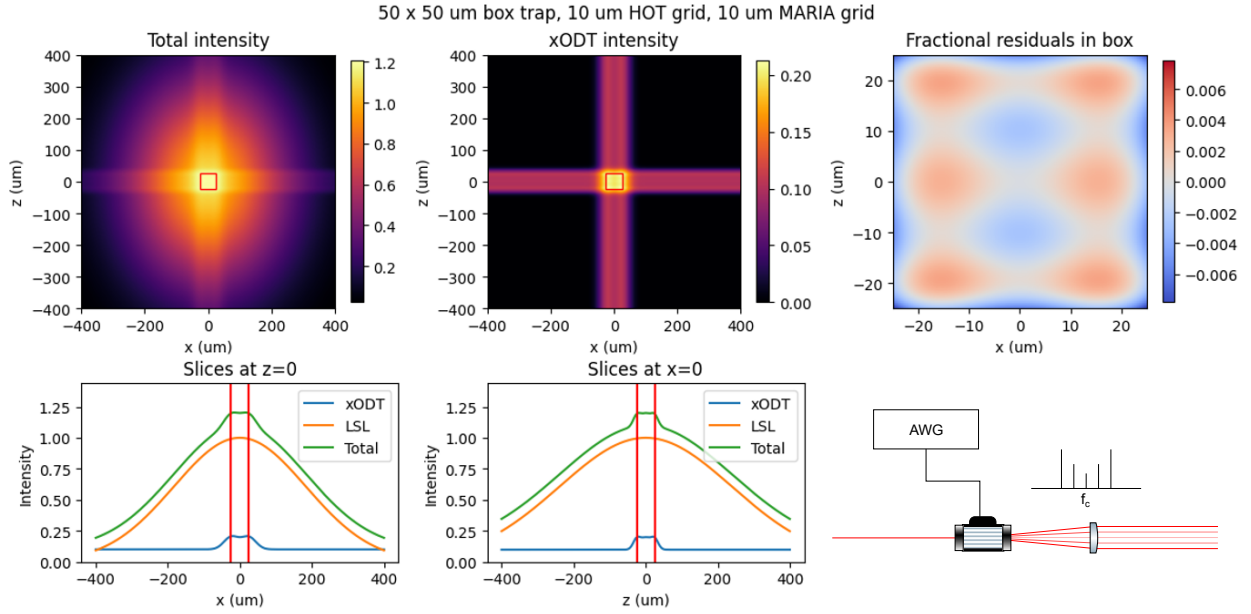

Figure 6.17: A scheme for compensating for the lattice potential to create a flat region. Here, the simulated potentials are shown for the accordion lattice and 20 μm-waist beams spaced every 10 μm with powers optimized to create a homogenous 50 μm square region in the center of the accordion lattice potential. The beams are shaped by applying multiple tones to an AOD, resulting in light diffracted at different angles (bottom right). By optimizing the power in each tone, the potential can be flattened to a high degree of homogeneity (top right).

Chapter 7

Towards spin-squeezing for enhanced quantum sensing

"Things are going to slide, slide in all directions
Won't be nothing
Nothing you can measure anymore"

The Future – Leonard Cohen

This thesis describes development and application of methods for controlling interactions and motion of polar molecules, spectroscopic exploration of the dynamics of interacting molecules, and progress towards producing low-entropy systems which would enable observation of even richer physics. Although potential future directions are discussed throughout, I conclude by presenting prospects and preliminary work for generating spin-squeezed states. Observation of squeezing relies on many of the tools developed in this thesis and is broadly relevant for both many-body physics and precision measurements applications.

A system of spins satisfies the uncertainty relation $\mathrm{Var}(S_i)\mathrm{Var}(S_j) \geq |\langle S_K \rangle|^2/4$ for any orthogonal directions i, j, k on the Bloch sphere [288]. For unentangled spins (Fig. 7.1a), the variance is distributed equally between the two directions such that $\mathrm{Var}(S_i) = \mathrm{Var}(S_j)$. Evolution under many nonlinear Hamiltonians, including OAT (Fig. 7.1b) and TAT (Fig. 7.1) can generate spin-squeezing, in which an entangled state is created where the variance in one quadrature is reduced at the expense of increased variance in the orthogonal direction. Given that we have observed both OAT and TAT at the mean-field level (Ch. 4), observing squeezing directly would be an exciting next step.

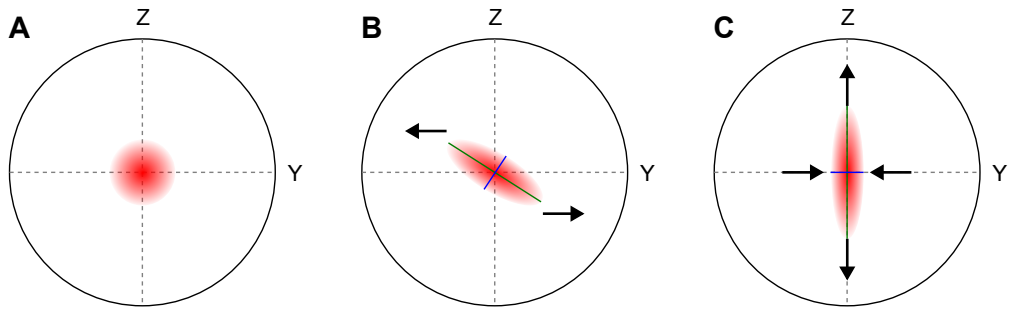

Figure 7.1: Cartoons of the quasiprobability distributions for a coherent spin state (a) and squeezed states generated by OAT (b) and TAT (c) are shown on the Bloch sphere. For the squeezed states, the blue (green) lines show the squeezed (antisqueezed) quadratures and the arrows indicate the direction the coherent state is deformed under the squeezing dynamics.

7.1 Generating a spin-squeezed state

In a quantum sensor, a signal is mapped onto the quantum state of a system consisting of spins. The spins are then read out by a projective measurement. Due to the probabilistic nature of the measurement, the variance of a sensor comprising N unentangled spins scales as $1/N$. These fluctuations are known as quantum projection noise (QPN; Sec. 7.1.1) and can limit the performance of the sensor. Appropriately selected entangled states can overcome this limit and reach variance scaling as efficiently as $1/N^2$, which is known as the Heisenberg limit.

One such class of entangled states which are relatively robust and can be prepared with experimentally accessible Hamiltonians are spin-squeezed states, first proposed in [169]. The original proposal discusses all-to-all Hamiltonians, but further theoretical work suggests that finite-range interactions [196, 197, 191] can also scalably generate squeezing. Itinerance, accessible with molecules, enhances the effective range of interactions, and is predicted [165, 209] to improve squeezing. Both the OAT and TAT Hamiltonians explored in Ch. 4 generate spin-squeezed states from initial product states.

Spin squeezing was first demonstrated in systems with all-to-all interactions [288], including optical cavities [289] and spinor BECs [290]. More recently, squeezing has been observed with a va-

riety of platforms with finite-range interactions, such as Rydberg atoms [195, 291, 292], NV centers [293], magnetic atoms [194], atoms in optical lattices [294], and trapped ions [295]. [194], which presents squeezing of spins comprising hyperfine levels of magnetic erbium atoms, is particularly interesting, as it experimentally demonstrates enhanced squeezing with itinerant atoms.

Producing spin-squeezed states with polar molecules could enhance the sensitivity of precision measurement experiments, such as measurement of the eEDM, for which molecules are the leading platform [33]. While KRb is not particularly sensitive to these fundamental physics effects, a demonstration of squeezing using KRb could inform future experiments with other species, for which the many-body physics should be essentially the same. In addition, squeezing serves as a probe for many-body physics – scalable squeezing is intimately connected with magnetic order [197].

7.1.1 Quantum projection noise

Before we discuss squeezing, we consider the noise in measurements of unentangled particles. Probability concepts referenced here are discussed in [240]. We consider the scenario where N spin-1/2 particles are prepared in the initial state where each is independently measured as spin-up with probability p and spin-down with probability $q = 1 - p$. We define the asymmetry $\mathcal{A} = \frac{N_\downarrow - N_\uparrow}{N_\uparrow + N_\downarrow}$ [35].

By linearity of expectation, $\langle \mathcal{A} \rangle = \frac{\langle N_\downarrow \rangle - \langle N_\uparrow \rangle}{N} = \frac{Np - Nq}{N} = 2p - 1$. The expectation value $\langle \mathcal{A}^2 \rangle$ is, by law of the unconscious statistician (LOTUS),

$$\langle \mathcal{A}^2 \rangle = \sum_{k=0}^{N} \left(\frac{k - (N-k)}{N} \right)^2 \left(\binom{N}{k} p^k q^{N-k} \right) = \langle \mathcal{A} \rangle^2 + \frac{4pq}{N} \tag{7.1}$$

The variance of $\mathcal{A}$ is therefore $\mathrm{Var}(\mathcal{A}) = \langle \mathcal{A}^2 \rangle - \langle \mathcal{A} \rangle^2 = \frac{4pq}{N}$. For $p = q = 1/2$, $\mathrm{Var}(\mathcal{A}) = 1/N$.

This noise limits the phase sensitivity of a Ramsey interferometer – the standard deviation of a phase measurement with N unentangled spins is $\sigma(\phi) = \sigma(\mathcal{A}) \frac{\partial \phi}{\partial \mathcal{A}} = 1/\sqrt{N}$. This is known as the standard quantum limit.

7.1.2 Squeezing by one-axis twisting

A spin-squeezed state can be generated if the particles initially prepared in $|X\rangle^{\otimes N}$ are allowed to evolve for time t under the all-to-all Hamiltonian $H = \chi S_z^2$. After evolution, the state is rotated about $\hat{X}$ by an angle θ in order to analyze its noise in different quadratures. The orientation of the spins can be then measured in the Z basis. As calculated analytically [169], the measurement has expected value $\langle S_z \rangle = 0$ and variance

$$\xi^2 = 1 + \frac{N-1}{4}\left(A - \sqrt{A^2 + B^2}\cos(2(\theta + \delta))\right) \text{ with}$$
$$A = 1 - \cos^{N-2}(2\chi t)$$
$$B = 4\cos^{N-2}(\chi t)\sin(\chi t)$$
$$\delta = \frac{1}{2}\arctan\left(\frac{B}{A}\right)$$

times the initial value, $\langle S_z^2 \rangle = \frac{N}{4}$. For $\theta = -\delta$, the normalized variance $\mathrm{Var}(\mathcal{A})$ is reduced by a factor of $\xi^2 = 1 + \frac{N-1}{4}\left(A - \sqrt{A^2 + B^2}\right)$. At the optimal time, the minimum variance scales as $N^{1/3}$, indicating the scalability of the squeezing process [169]. The minimum and maximum variances are plotted as a function of time for $N = 1000$ in Fig. 7.2.

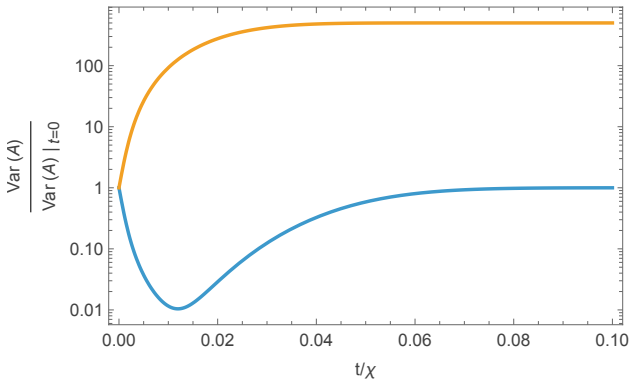

Figure 7.2: The relative variance of $\mathrm{Var}(\mathcal{A})$ in the maximally squeezed (blue) and antisqueezed (orange) quadratures is plotted as a function of time for all-to-all OAT with rate χ and $N = 1000$.

All-to-all interactions represent an idealized model for OAT – in physical realizations, finite-range interactions [196, 197] and decoherence [296, 297] reduce the amount of squeezing that can be generated. For sufficient interaction range (including $1/r^3$ in 2D for spin-exchange Hamiltonians) and low enough noise, the squeezing is scalable with system size.

7.1.3 Measuring spin squeezing

In principle, generating a spin-squeezed state is straightforward, since the native dipolar interactions between itinerant molecules result in one-axis twisting (Sec. 4.2). However, quantifying the amount of squeezing generated requires an accurate measurement of S_z and a good understanding of the noise on the measurement. On the KRb experiment, we detect the molecules by state-resolved STIRAP dissociation followed by absorption imaging of the Feshbach molecules (see Sec. 2.1.4). We analyze the noise generated by this process in Sec. 7.1.3.1 and 7.1.3.2. Further, imperfections during the generation of squeezing, both due to technical noise and molecular collisions, can reduce squeezing and increase noise. We discuss these and methods for overcoming them in Sec. 7.1.4

7.1.3.1 STIRAP and dissociation

The STIRAP and dissociation of the molecules introduces two noise processes: loss due to finite efficiency and depletion of molecules shelved in $|1\rangle$. Each of the N_0 molecules in $|0\rangle$ is independently transferred with probability P_{STIRAP} and photodissociated with probability $P_{\mathrm{dissociation}}$. Similarly, each of the N_1 molecules in $|1\rangle$ undergoes the same process, with an additional probability P_{shelving} denoting the probability of surviving the $|0\rangle$ STIRAP and imaging. The numbers of molecules imaged are therefore given by independent binomial distributions

$$\tilde{N}_0 \sim B(N_0, P_0)$$

$$\tilde{N}_1 \sim B(N_1, P_1)$$

where $P_0 = P_{\text{STIRAP}} P_{\text{dissociation}}$, $P_1 = P_{\text{shelving}} P_{\text{STIRAP}} P_{\text{dissociation}}$, and the tildes denote measured values. Under linear propagation of uncertainty,

$$\begin{aligned} \text{Var}(\tilde{\mathcal{A}}) &\approx \left(\frac{\partial \tilde{\mathcal{A}}}{\partial \tilde{N}_1}\right)^2 \text{Var}(\tilde{N}_1) + \left(\frac{\partial \tilde{\mathcal{A}}}{\partial \tilde{N}_0}\right)^2 \text{Var}(\tilde{N}_0) \\ &= \frac{4\left\langle \tilde{N}_0 \right\rangle^2}{\left\langle \tilde{N} \right\rangle^4} \left(\left\langle \tilde{N}_1 \right\rangle (1 - P_1) \right) + \frac{4\left\langle \tilde{N}_1 \right\rangle^2}{\left\langle \tilde{N} \right\rangle^4} \left(\left\langle \tilde{N}_0 \right\rangle (1 - P_0) \right) \end{aligned} \tag{7.2}$$

This variance follows the same $1/N$ scaling as QPN. Taking realistic probabilities $P_{\text{STIRAP}} = 0.92$ (Sec. 2.2.2), $P_{\text{dissociation}} = 0.87$ (Sec. 2.1.4), $P_{\text{shelving}} = 0.9$ (Sec. 2.1.4), and $N_0 = N_1 = N/2$, $\text{Var}(\tilde{\mathcal{A}}) = 0.32/N$, or roughly 1/3 of QPN. As such, our current STIRAP and dissociation efficiency will not prevent the initial observation of squeezed states, but may limit the sensitivity of future measurements if highly squeezed states can be generated.

7.1.3.2 Absorption imaging

Absorption imaging and its noise has been discussed in detail in prior works such as [298, 299, 300, 83]. In this section, I give an overview of how atom number can be measured using absorption imaging and describe the noise that absorption imaging introduces, largely following [298].

In absorption imaging, resonant probe light with initial intensity I_0 is shined onto the atoms in the $\hat{x}$ direction. An atom at position x scatters the probe light with cross-section $\sigma(x) = \sigma_0/(1 + I(x)/I_{\text{sat}})$ where $I(x)$ is the light's intensity at position x. For the D_2-line of ^{40}K driven with circularly polarized light, the low-intensity cross-section $I_{\text{sat}} = \frac{\hbar\omega^3\Gamma}{12\pi c^2} = 1.75$ mW/cm^2 and $\sigma_0 = \frac{3\lambda^2}{2\pi} = 0.29$ μm^2 [91, 90]. The change in intensity as a result of scattering from the atoms is

$$\frac{\mathrm{d}I}{\mathrm{d}x} = -(1 - \Omega) n(x) \sigma(x) I \tag{7.3}$$

where Ω is the fraction of the fluorescence imaged onto the camera. For our side imaging path, $\Omega \approx 0.05$. Integrating over x and solving for the column density n in terms of $T = I(\infty)/I(0)$ gives

$$n = \frac{1}{\sigma_0(1-\Omega)}(-\ln(T) + s_0(1-T)) \tag{7.4}$$

The total number of atoms N_{img} imaged is simply the sum of na over all pixels in a region of interest, where $a = Ma_{\text{px}}$ is the area of the image plane mapped onto each pixel, with M being the imaging system's magnification. For our side imaging system, $a = (1.718\,\mu\text{m})^2$.

To measure T, we take three images, one with the atoms ("shadow"), one with only the probe light ("light"), and one with no light incident on the camera ("dark"), where the dark frame captures counts due to background light or dark currents. The transmission is calculated as $T = \frac{C_{\text{shadow}} - C_{\text{dark}}}{C_{\text{light}} - C_{\text{dark}}}$.

A variety of sources can contribute to errors in estimating T and thus N_{img}. Although other random processes, like readout noise of the camera, can contribute [83], the dominant statistical error is photon shot noise on the light and shadow frames. Photons hit a pixel with rate Γ_ν for a time t_{exp}. Each photon is converted to a photoelectron with probability set by the camera's quantum efficiency η. When the pixel is read out, each photoelectron is deterministically converted into g counts. For our Andor iXon 888 camera with standard operating settings, $g = 0.29$ and $\eta = 0.85$. The resulting number of counts recorded is distributed as $c = gN_\nu$ where the photoelectron number follows a Poisson distribution $N_\nu \sim \text{Pois}(\eta\Gamma_\nu t_{\text{exp}})$. The mean and variance of C are $\langle C\rangle = g\eta\Gamma_\nu t_{\text{exp}}$ and $\langle C^2\rangle^2 - \langle C\rangle^2 = g\langle C\rangle$ respectively. Plugging this into Eq. 7.4 gives the variance of the measured column density as

$$\left\langle n^2\right\rangle - \langle n\rangle^2 = \frac{g}{C_{\text{sat}}^2\sigma_0^2(1-\Omega)^2}\left(C_{\text{shadow}} + C_{\text{light}} + 4C_{\text{sat}} + \frac{C_{\text{sat}}^2}{C_{\text{light}}} + \frac{C_{\text{sat}}^2}{C_{\text{shadow}}}\right) \tag{7.5}$$

where C_{sat} is the number of counts corresponding to $I = \alpha I_{\text{sat}}$, where the empirically calibrated parameter $\alpha > 1$ captures a reduction in the absorption cross-section due to imperfect polarization [301]. For our experimental parameters, with $C_{\text{sat}} = 2955$, the standard deviation of N is plotted as a function of light intensity in Fig. 7.3. We can see that the noise is minimized for $I \approx I_{\text{sat}}$ and that the noise increases gradually with column density, such that the signal-to-noise is maximized

at high density.

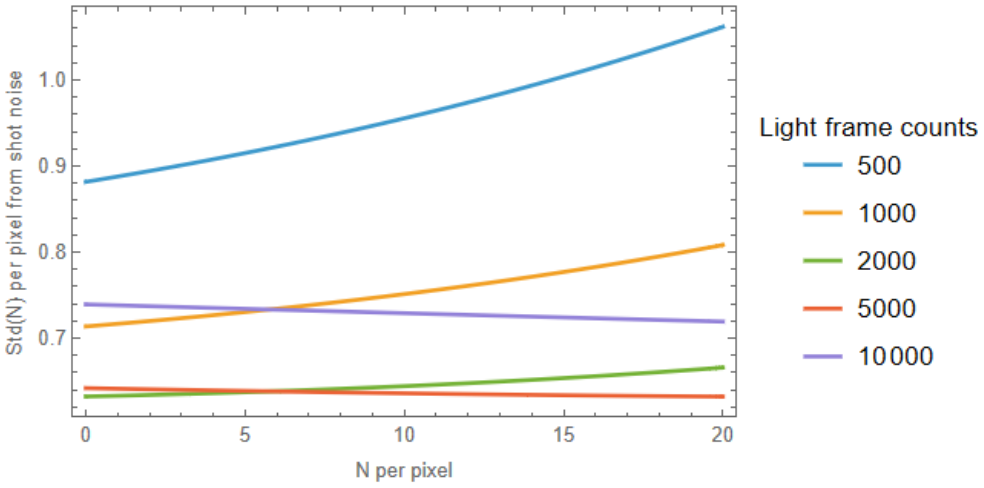

Figure 7.3: The standard deviation of atom number per pixel due to photon shot noise is plotted as a function of number per pixel and light intensity, with parameters for imaging K on the KRb apparatus' side imaging system.

The shot noise on each pixel is independent, so the variances in N add. Taking a typical number variance per pixel of $(0.63 \text{ atoms})^2$ and a typical extent of the atomic cloud over 3000 pixels, the standard deviation of the total number of atoms in each image is roughly 35. For $N \lessapprox 2450$, the resulting variance exceeds that of QPN, but for larger numbers or smaller image regions, QPN dominates over noise from absorption imaging. The shot noise per pixel can also be reduced by a factor of up to $\sqrt{2}$ if the light frame is taken at higher photon number or synthesized based on the shadow frame [302, 303], eliminating its contribution to the shot noise.

In addition to the statistical errors, a variety of systematic errors can lead to inaccurate atom counting, including differences in light distribution between the shadow and light frames, imperfect calibration of experimental parameters such as I_{sat} [301] and laser polarization, atomic motion and Doppler shifts during the images, finite laser linewidth, multiple scattering, and imaging thin clouds with sizes comparable to the imaging system's resolution. The latter two effects can be reduced by

turning off the trap and allowing the gas to expand before imaging, although at the cost of increasing the number of pixels to which shot noise contributes. In future experiments, single particle-resolved fluorescence imaging [147, 192, 47] will reduce statistical and eliminate most systematic errors. Fortunately, for squeezing, the systematic errors can be largely compensated using differential measurements – the variance of a squeezed state will vary as a function of rotation angle θ, while an unentangled state will have constant variance.

7.1.3.3 Measuring quantum projection noise

To validate the performance of our imaging system, we attempt measurement of QPN with molecules. We first produced approximately 12000 molecules in a single layer of the accordion lattice (Sec. 6.4.2) at $|\mathbf{E}| = 0$. We then reduced the molecule number by shelving some fraction f in $|1\rangle$ and removing the molecules in $|0\rangle$ using the STIRAP down leg (Sec. 5.1). By applying a $\pi/2$ pulse, we prepared each molecule in an equal superposition of $|0\rangle$ and $|1\rangle$. To image the molecules, we ramped off the accordion lattice in 500 μs before dissociating and imaging the molecules in $|0\rangle$[1] . After a further 2 ms of expansion, a π pulse transfers the molecules in $|1\rangle$ to $|0\rangle$ before dissociation and imaging. A sample image of the molecules in each frame is shown in Fig. 7.4.

We recorded 50 images each for 7 values of f between 0.1 and 1 and computed the variance of $\mathcal{A}$ for each f, corresponding to different average molecule numbers. We found that $\mathrm{Var}(\mathcal{A})$ saturates at around 10^{-3} for large f, much larger than the expected value of $1/N \gtrapprox 10^{-4}$ (Fig. 7.5a).

To understand the origin of the excess noise, we analyzed the data dividing the cloud into two sub-ensembles of approximately equal size (Fig. 7.4), inspired by [294, 304]. Each ensemble is taken as half of the cloud, with the center and 3σ extent determined by a Gaussian fit. A six-pixel region is excluded in the center to ensure that the finite imaging resolution does not lead to correlations between the regions. We find that $\mathcal{A}$ is strongly correlated between the two ensembles, with correlation coefficient as high as 0.93 for $f = 1$. This suggests that technical noise, originating

[1] A longer time-of-flight is likely optimal for avoiding resolution and high optical density effects in future measurements.

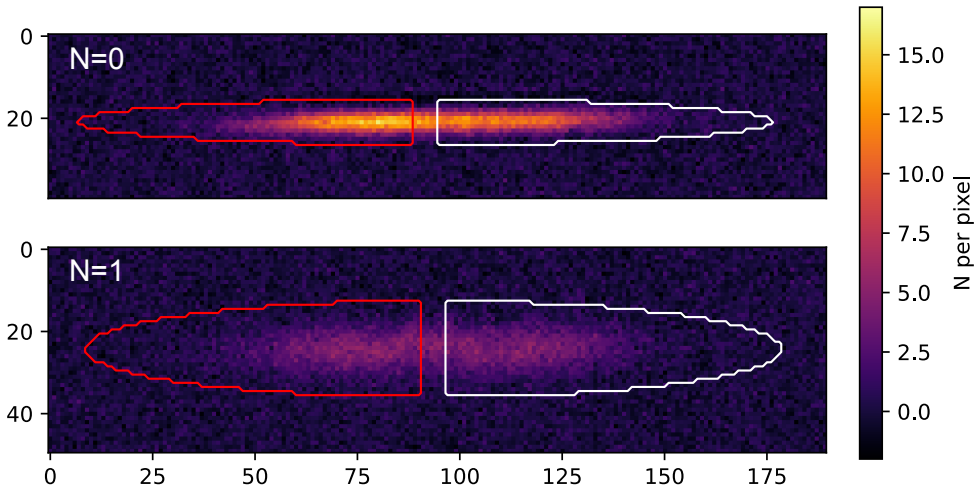

Figure 7.4: A sample image of molecules in $|0\rangle$ and $|1\rangle$ is shown, along with the two regions selected for analysis in a differential measurement.

from either shot-to-shot variation in the pulse area or the probability of dissociating and detecting molecules, is responsible for the excessive variance. We measured similar variances for pulse areas of $\pi/2, 3\pi/2, \ldots$, suggesting that variation of the Rabi frequency is not the dominant issue.

To reject the correlated noise, we can compute $\mathrm{Var}(\mathcal{A}_1 - \mathcal{A}_2)$ instead of $\mathrm{Var}(\mathcal{A})$. To understand why this works, we consider the scenario where, instead of each molecule being in state $|1\rangle$ with constant probability $p = 1/2$, p for each shot is drawn from a probability distribution $P(x)$. For the whole ensemble, by the law of total variance [240],

$$\mathrm{Var}(\mathcal{A}) = \langle \mathrm{Var}(\mathcal{A}|P) \rangle + \mathrm{Var}(\langle \mathcal{A}|P \rangle) = \frac{4\langle pq \rangle}{N} + 4\mathrm{Var}(p) \tag{7.6}$$

where the last term is evaluated by LOTUS,

$$\mathrm{Var}(\langle \mathcal{A}|P \rangle) = \int_0^1 (2p-1)^2 P(p)\,\mathrm{d}p - \langle A|P \rangle^2 = 1 - 4\langle p \rangle + 4\langle p^2 \rangle - (2\langle p \rangle - 1)^2 = 4\mathrm{Var}(p) \tag{7.7}$$

noting that $\langle pq \rangle = \langle p \rangle - \langle p \rangle^2 + \mathrm{Var}(p)$. The variance for the differential measurement is $\mathrm{Var}(\mathcal{A}_1 - \mathcal{A}_2) = \langle \mathrm{Var}((\mathcal{A}_1 - \mathcal{A}_2)|P) \rangle + \mathrm{Var}(\langle (\mathcal{A}_1 - \mathcal{A}_2)|P \rangle)$. By symmetry between the ensembles, the second term is zero, so this equals $\frac{16\langle pq \rangle}{N}$. Because it lacks the additive $\mathrm{Var}(p)$ term, $\mathrm{Var}(\mathcal{A}_1 - \mathcal{A}_2)$ is much

less sensitive to fluctuations in p than $\mathrm{Var}(\mathcal{A})$. If quantum projection noise is the dominant source of variance, then $\mathrm{Var}(\mathcal{A}_1 - \mathcal{A}_2)$ equals $4/N$ for $\theta = \pi/2$, since the variances of the two uncorrelated sub-ensembles add and the variance of each is $2/N$.

$\mathrm{Var}(\mathcal{A}_1 - \mathcal{A}_2)$ is plotted as a function of N in Fig. 7.5a. We see a clear increase with N, suggesting that we are indeed sensitive to QPN. However, the variance is lower than the expected value of $4/N$ (dashed black line) – the data is better fit with the curve $\mathrm{Var}(\mathcal{A}_1 - \mathcal{A}_2) = 2.5(33)/N$ (solid red line). This suggests that the number is underestimated by a factor of 1.6(2), allowing calibration of the imaging system using QPN. As a check on the calibration, we measure $\mathrm{Var}(\mathcal{A}_1 - \mathcal{A}_2)$ for $f = 1$ for different p, implemented by varying the area of the initial pulse. Once again, the result (Fig. 7.5b) is below the expected $\frac{16\langle pq \rangle}{N}$, suggesting the number is underestimated.

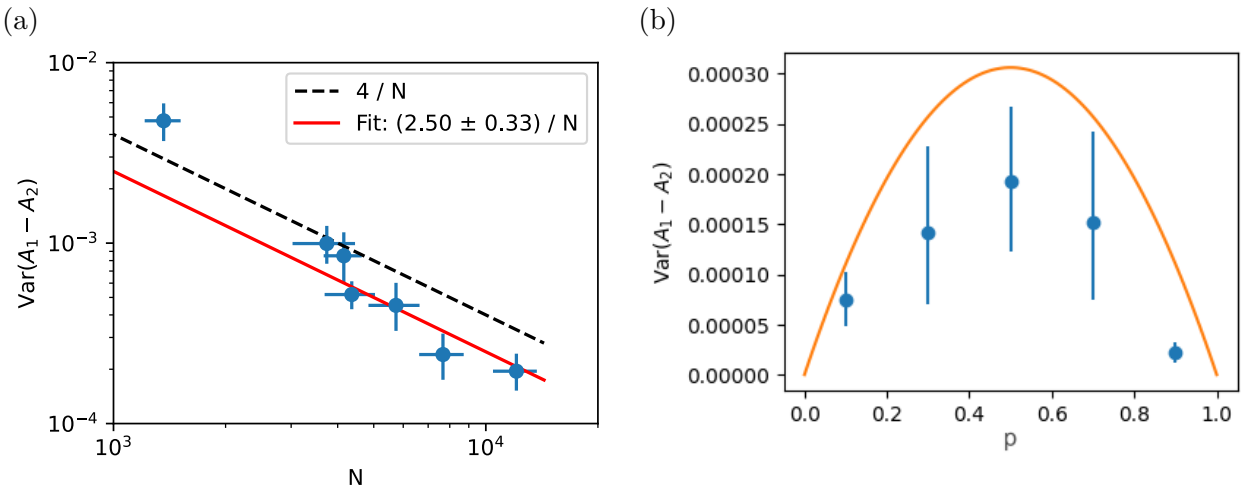

Figure 7.5: (a) $\mathrm{Var}(\mathcal{A}_1 - \mathcal{A}_2)$ is plotted as a function of molecule number after a $\theta = \pi/2$ pulse. The uncertainty in variance is from bootstrapping and the uncertainty in N is the standard deviation of the number in each dataset. The dashed black line is the expected variance of $4/N$ and the solid red line is a fit to the form c/N. (b) $\mathrm{Var}(\mathcal{A}_1 - \mathcal{A}_2)$ is plotted as a function of p for $N = 16(2) \times 10^3$ molecules. The orange line is the expected variance of $16pq/N$.

7.1.4 Towards squeezing with molecules

Given that we could observe quantum projection noise, we attempted to generate and detect spin-squeezed states, following the proposal [165]. After producing approximately 15000 molecules at $|\mathbf{E}| = 0$ and applying a $\pi/2$ pulse about the $\hat{X}$ axis to prepare a superposition, we allowed the molecules to evolve for 1 ms while applying an XY8 dynamical decoupling sequence. We then applied an analysis pulse with variable area θ about the $\hat{Y}$ axis before imaging the molecules. For each θ, we estimated the variance $\mathrm{Var}(\mathcal{A}_1 - \mathcal{A}_2)$ as above.

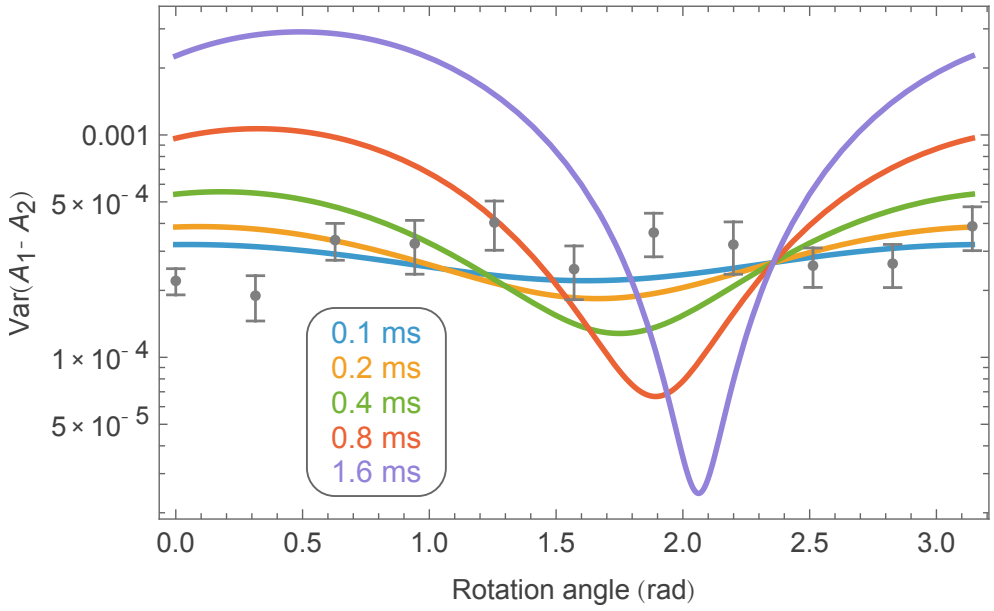

Figure 7.6: $\mathrm{Var}(\mathcal{A}_1 - \mathcal{A}_2)$ for $N \approx 15000$ is plotted as a function of analysis pulse angle θ after evolution for 1 ms under an XY Hamiltonian with XY8 dynamical decoupling. The uncertainties are 1 s.e. derived from bootstrapping. The expected variances for squeezed states generated under all-to-all interactions with $\chi_0 = 2\pi \times -0.02$ Hz, as measured in [117], are plotted as colored lines for different evolution times. In the absence of squeezing, $\mathrm{Var}(\mathcal{A}_1 - \mathcal{A}_2) \approx 2.7 \times 10^{-4}$, consistent with the measured data.

Unfortunately, we saw no strong dependence on θ (points in Fig. 7.6), as opposed to what would be expected with a squeezed state generated by all-to-all interactions with the measured χ

(Sec. 4.2), shown as solid lines for different times in the figure. This apparent lack of squeezing suggests that all-to-all OAT is not a good model for the system at the experimental condition of $T/T_F \approx 1$, because of a shorter effective interaction range or collisional dephasing (Sec. 5.3), which limits the Ramsey coherence time to ≈ 7 ms. Although it is possible that technical noise could mask squeezing by adding to the variance, the additional noise in antisqueezed quadratures should still be visible, suggesting that technical noise is not the dominant limitation.

Multiple directions exist for improving the setup such that squeezing might be visible. A deeply degenerate gas (Ch. 6) is predicted to better approximate all-to-all interactions and generate squeezing more efficiently [165]. In addition, changing the interaction Hamiltonian from an XY model at $|\mathbf{E}| = 0$ to an XXZ model at $|\mathbf{E}| \approx 4.6$ kV/cm reduces χ by a factor of approximately 2 (Sec. 4.2.1) but suppresses the interaction-induced dephasing rate κ to nearly zero (Fig. 5.2). The improved ratio of coherent dynamics to dephasing should allow for much more efficient generation of squeezing [165, 297]. Squeezing at nonzero electric fields is complicated by dephasing between the spins and the microwave oscillator due to electric field noise [105], so improvements in the electric field filters, as discussed in Sec. 2.1.5, would likely be necessary. Another approach to entanglement-enhanced sensing with relaxed detection requirements is amplification of a perturbation to a squeezed state by reversing the squeezing Hamiltonian [178]. This approach, which has been demonstrated in cavity QED systems [179] and NV centers [180], could be implemented by switching the rotational states comprising the spin (Sec. 4.2.2).

Chapter 8

Conclusion

"I just wanted you to know
That this is me trying"

This Is Me Trying – Taylor Swift

A quantum simulator based on ultracold polar molecules offers great opportunities for exploring the many-body physics of systems combining itinerance with strong or long-range interactions [31, 173]. Inspired by ultracold atom experiments [210, 21], key technical requirements for such a simulator are

(1) Initialization of molecules in a desired internal state

(2) High-fidelity, state-resolved detection

(3) Control of intermolecular interactions

(4) Control of molecular motion

(5) Preparation of low-entropy ensembles

Requirements (1) and (2) have largely been fulfilled. Because of the coherent nature of production from ultracold atoms, associated molecules such as KRb are prepared in a single hyperfine state [53] and can be coherently transferred to other internal states using microwaves [97]. Through optical pumping and feedback [47], laser-cooled molecules can also be initialized in a desired state. Associated molecules have been detected with high fidelity through efficient STIRAP dissociation

[113] and quantum gas microscopy [147, 192] of their constituent atoms and laser-cooled molecules through direct fluorescence imaging [45, 47].

The work described in this thesis represents significant progress towards requirements (3) and (4). Through application of d.c. electric fields (Sec. 2.1.5), we induced large lab-frame dipole moments, realizing continuously tunable XXZ spin models (Sec. 4.2) and controlling collisions between molecules (Sec. 6.2.3.1). By driving rotational transitions with microwave pulse sequences, we engineered less symmetric XYZ models (Sec. 4.3) inaccessible with d.c. electric fields. Using Ramsey spectroscopy, we were able to measure the spin dynamics of a quasi-2D ensemble of itinerant molecules at the mean-field level (Ch. 4), confirming the efficacy of our control and demonstrating for the first time, along with [187], two-axis twisting dynamics [169]. Complementary efforts by the MPQ [305, 306, 307], Columbia [308, 309], CUHK [222], and Princeton [147, 310] groups demonstrate tuning of interactions through microwave dressing or Floquet engineering. By adding additional optical lattices to regulate in-plane motion (Sec. 2.2.1), we realized t-J-V-W Hamiltonians (Sec. 5.4.1), highly tunable generalizations of Fermi-Hubbard models expected to exhibit interesting phases [76].

Even with non-degenerate gases and global measurements, these models exhibit rich many-body physics. We used Ramsey spectroscopy to explore the dephasing of an initially polarized superposition state resulting from the interplay between motion and dipolar interactions (Ch. 5). Building on our group's previous work [101, 102] studying molecules with spin-exchange interactions pinned in a deep optical lattice, we demonstrated that interaction-driven dephasing could be modified or even halted by tuning the parameters of XXZ spin models (Sec. 5.2). By studying the same process with itinerant quasi-2D systems (Sec. 5.3), we developed a microscopic understanding of how collisions between molecules in superposition states can lead to dephasing. In both pinned and itinerant systems, we were able to compare the dynamics realized by electric-field tuned and Floquet-engineered Hamiltonians (Sec. 5.5). Interpolating by the pinned and itinerant regimes by allowing limited motion with intermediate depth transverse optical lattices, we explored the spin dynamics of t-J-V-W Hamiltonians, supporting the development of new theoretical methods to

explain unexpected trends (Sec. 5.4.2).

Requirement (5) remains an outstanding challenge for polar molecules, particularly in optical lattices. Significant progress has been made in directly producing or evaporatively cooling molecules into degenerate Fermi [85, 99, 87, 260] and Bose [259, 222] gases, and preparing small ordered arrays of molecules in optical tweezers [311, 312, 47]. However, the highest reported filling in a 3D optical lattice remains approximately 30% [103, 104, 231]. Building on previous work from our group [99, 83] and the atomic quantum gas community [272], we built an accordion lattice (Sec. 6.3) for compressing atoms into two-dimensional layers, enabling production of large numbers of molecules in a geometry compatible with efficient evaporative cooling. In Ch. 6, I present initial experimental results and discuss possible next steps that should enable production of deeply degenerate 2D bulk and lattice gases of fermionic molecules. Advances in microwave shielding [313] and toward production of new, highly-dipolar molecular species [314] offer promising alternative approaches towards producing colder systems.

The next few years will be an exciting time for ultracold molecule experiments. As lower-entropy ensembles are produced and combined with existing methods for control and detection, long-awaited experiments on preparing ordered phases [173, 172, 31] or controlled collective dynamics [228, 198, 199, 165] should become possible. Observation of droplets in an interacting BEC is one recent development in that direction [309]. Another application, the generation of spin-squeezed states for precision measurement [33], is discussed in Ch. 7.

Bibliography

[1] I. I. Rabi, J. R. Zacharias, S. Millman, and P. Kusch, Physical Review **53**, 318 (1938).

[2] A. Kastler, Science **158**, 214 (1967).

[3] T. H. Maiman, Nature **187**, 493 (1960).

[4] The Nobel Prize in Physics 1997 - Advanced information.

[5] W. Ketterle and N. J. V. Druten, in Advances In Atomic, Molecular, and Optical Physics, Vol. 37, edited by B. Bederson and H. Walther (Academic Press, 1996) pp. 181–236.

[6] M. H. Anderson, J. R. Ensher, M. R. Matthews, C. E. Wieman, and E. A. Cornell, Science **269**, 198 (1995).

[7] W. Ketterle, Reviews of Modern Physics **74**, 1131 (2002).

[8] B. DeMarco and D. S. Jin, Science **285**, 1703 (1999).

[9] W. S. Bakr, J. I. Gillen, A. Peng, S. Fölling, and M. Greiner, Nature **462**, 74 (2009).

[10] J. F. Sherson, C. Weitenberg, M. Endres, M. Cheneau, I. Bloch, and S. Kuhr, Nature **467**, 68 (2010).

[11] A. M. Kaufman and K.-K. Ni, Nature Physics **17**, 1324 (2021).

[12] H. Mabuchi and A. C. Doherty, Science **298**, 1372 (2002).

[13] H. J. Manetsch, G. Nomura, E. Bataille, X. Lv, K. H. Leung, and M. Endres, Nature 10.1038/s41586-025-09641-4 (2025).

[14] M. Xu, L. H. Kendrick, A. Kale, Y. Gang, C. Feng, S. Zhang, A. W. Young, M. Lebrat, and M. Greiner, Nature **642**, 1 (2025).

[15] B. L. Augenbraun, L. Anderegg, C. Hallas, Z. D. Lasner, N. B. Vilas, and J. M. Doyle, in Advances In Atomic, Molecular, and Optical Physics, Vol. 72, edited by L. F. DiMauro, H. Perrin, and S. F. Yelin (Academic Press, 2023) pp. 89–182.

[16] S. M. Girvin and K. Yang, Modern Condensed Matter Physics (Cambridge University Press, 2019).

[17] P. A. Lee, N. Nagaosa, and X.-G. Wen, Reviews of Modern Physics **78**, 17 (2006).

[18] H. L. Stormer, D. C. Tsui, and A. C. Gossard, Reviews of Modern Physics **71**, S298 (1999).

[19] I. M. Georgescu, S. Ashhab, and F. Nori, Reviews of Modern Physics **86**, 153 (2014).

[20] E. Altman, K. R. Brown, G. Carleo, L. D. Carr, E. Demler, C. Chin, B. DeMarco, S. E. Economou, M. A. Eriksson, K.-M. C. Fu, M. Greiner, K. R. Hazzard, R. G. Hulet, A. J. Kollár, B. L. Lev, M. D. Lukin, R. Ma, X. Mi, S. Misra, C. Monroe, K. Murch, Z. Nazario, K.-K. Ni, A. C. Potter, P. Roushan, M. Saffman, M. Schleier-Smith, I. Siddiqi, R. Simmonds, M. Singh, I. Spielman, K. Temme, D. S. Weiss, J. Vučković, V. Vuletić, J. Ye, and M. Zwierlein, PRX Quantum **2**, 017003 (2021).

[21] F. Schäfer, T. Fukuhara, S. Sugawa, Y. Takasu, and Y. Takahashi, Nature Reviews Physics **2**, 411 (2020).

[22] A. Mazurenko, C. S. Chiu, G. Ji, M. F. Parsons, M. Kanász-Nagy, R. Schmidt, F. Grusdt, E. Demler, D. Greif, and M. Greiner, Nature **545**, 462 (2017).

[23] U.-J. Wiese, Annalen der Physik **525**, 777 (2013).

[24] C. W. Bauer, Z. Davoudi, A. B. Balantekin, T. Bhattacharya, M. Carena, W. A. de Jong, P. Draper, A. El-Khadra, N. Gemelke, M. Hanada, D. Kharzeev, H. Lamm, Y.-Y. Li, J. Liu, M. Lukin, Y. Meurice, C. Monroe, B. Nachman, G. Pagano, J. Preskill, E. Rinaldi, A. Roggero, D. I. Santiago, M. J. Savage, I. Siddiqi, G. Siopsis, D. Van Zanten, N. Wiebe, Y. Yamauchi, K. Yeter-Aydeniz, and S. Zorzetti, PRX Quantum **4**, 027001 (2023).

[25] A. D. Ludlow, M. M. Boyd, J. Ye, E. Peik, and P. O. Schmidt, Reviews of Modern Physics **87**, 637 (2015).

[26] R. Geiger, A. Landragin, S. Merlet, and F. Pereira Dos Santos, AVS Quantum Science **2**, 024702 (2020).

[27] D. Budker and M. Romalis, Nature Physics **3**, 227 (2007).

[28] C. T. Fancher, D. R. Scherer, M. C. S. John, and B. L. S. Marlow, IEEE Transactions on Quantum Engineering **2**, 1 (2021).

[29] M. S. Safronova, D. Budker, D. DeMille, D. F. J. Kimball, A. Derevianko, and C. W. Clark, Reviews of Modern Physics **90**, 025008 (2018).

[30] T. Langen, G. Valtolina, D. Wang, and J. Ye, Nature Physics **20**, 702 (2024).

[31] S. L. Cornish, M. R. Tarbutt, and K. R. A. Hazzard, Nature Physics **20**, 730 (2024).

[32] A. Browaeys and T. Lahaye, Nature Physics **16**, 132 (2020).

[33] D. DeMille, N. R. Hutzler, A. M. Rey, and T. Zelevinsky, Nature Physics **20**, 741 (2024).

[34] ACME Collaboration, Nature **562**, 355 (2018).

[35] T. S. Roussy, L. Caldwell, T. Wright, W. B. Cairncross, Y. Shagam, K. B. Ng, N. Schlossberger, S. Y. Park, A. Wang, J. Ye, and E. A. Cornell, Science **381**, 46 (2023).

[36] L. Anderegg, N. B. Vilas, C. Hallas, P. Robichaud, A. Jadbabaie, J. M. Doyle, and N. R. Hutzler, Science **382**, 665 (2023).

[37] N. J. Fitch and M. R. Tarbutt, in Advances In Atomic, Molecular, and Optical Physics, Vol. 70, edited by L. F. Dimauro, H. Perrin, and S. F. Yelin (Academic Press, 2021) pp. 157–262.

[38] J. F. Barry, D. J. McCarron, E. B. Norrgard, M. H. Steinecker, and D. DeMille, Nature **512**, 286 (2014).

[39] L. Anderegg, B. L. Augenbraun, E. Chae, B. Hemmerling, N. R. Hutzler, A. Ravi, A. Collopy, J. Ye, W. Ketterle, and J. M. Doyle, Physical Review Letters **119**, 103201 (2017).

[40] N. B. Vilas, C. Hallas, L. Anderegg, P. Robichaud, A. Winnicki, D. Mitra, and J. M. Doyle, Nature **606**, 70 (2022).

[41] A. L. Collopy, S. Ding, Y. Wu, I. A. Finneran, L. Anderegg, B. L. Augenbraun, J. M. Doyle, and J. Ye, Physical Review Letters **121**, 213201 (2018).

[42] J. E. Padilla-Castillo, J. Cai, P. Agarwal, P. Kukreja, R. Thomas, B. G. Sartakov, S. Truppe, G. Meijer, and S. C. Wright, Magneto-optical trapping of aluminum monofluoride (2025), arXiv:2506.02266 [physics] .

[43] N. R. Hutzler, H.-I. Lu, and J. M. Doyle, Chemical Reviews **112**, 4803 (2012).

[44] M. D. Di Rosa, The European Physical Journal D - Atomic, Molecular, Optical and Plasma Physics **31**, 395 (2004).

[45] L. Anderegg, L. W. Cheuk, Y. Bao, S. Burchesky, W. Ketterle, K.-K. Ni, and J. M. Doyle, Science **365**, 1156 (2019).

[46] J. J. Burau, K. Mehling, M. D. Frye, M. Chen, P. Aggarwal, J. M. Hutson, and J. Ye, Physical Review A **110**, L041306 (2024).

[47] C. M. Holland, Y. Lu, S. J. Li, C. L. Welsh, and L. W. Cheuk, Physical Review X **15**, 031018 (2025).

[48] W. Ketterle, D. S. Durfee, and D. M. Stamper-Kurn, in Bose-Einstein Condensation in Atomic Gases (IOS Press, 1999) pp. 67–176.

[49] W. Ketterle and M. W. Zwierlein, La Rivista del Nuovo Cimento **31**, 247 (2008).

[50] C. Chin, R. Grimm, P. Julienne, and E. Tiesinga, Reviews of Modern Physics **82**, 1225 (2010).

[51] S. Jochim, M. Bartenstein, A. Altmeyer, G. Hendl, S. Riedl, C. Chin, J. Hecker Denschlag, and R. Grimm, Science **302**, 2101 (2003).

[52] M. Greiner, C. A. Regal, and D. S. Jin, Nature **426**, 537 (2003).

[53] K.-K. Ni, S. Ospelkaus, M. H. G. de Miranda, A. Pe'er, B. Neyenhuis, J. J. Zirbel, S. Kotochigova, P. S. Julienne, D. S. Jin, and J. Ye, Science **322**, 231 (2008).

[54] J. W. Park, S. A. Will, and M. W. Zwierlein, Physical Review Letters **114**, 205302 (2015).

[55] T. Takekoshi, L. Reichsöllner, A. Schindewolf, J. M. Hutson, C. R. Le Sueur, O. Dulieu, F. Ferlaino, R. Grimm, and H.-C. Nägerl, Physical Review Letters **113**, 205301 (2014).

[56] M. Guo, B. Zhu, B. Lu, X. Ye, F. Wang, R. Vexiau, N. Bouloufa-Maafa, G. Quéméner, O. Dulieu, and D. Wang, Physical Review Letters **116**, 205303 (2016).

[57] T. M. Rvachov, H. Son, A. T. Sommer, S. Ebadi, J. J. Park, M. W. Zwierlein, W. Ketterle, and A. O. Jamison, Physical Review Letters **119**, 143001 (2017).

[58] A. Z. Lam, N. Bigagli, C. Warner, W. Yuan, S. Zhang, E. Tiemann, I. Stevenson, and S. Will, Physical Review Research **4**, L022019 (2022).

[59] K. P. Zamarski, C. Beulenkamp, Y. Zeng, M. Landini, and H.-C. Nägerl, Spectroscopy and ground-state transfer of ultracold bosonic $^{39}K^{133}Cs$ molecules (2025), arXiv:2505.21207 [cond-mat] .

[60] V. Barbé, Ultracold RbSr: Optical and Magnetic Spectroscopy, Feshbach Resonances and Molecular Structure, Ph.D. thesis, University of Amsterdam (2020).

[61] S. Finelli, A. Ciamei, B. Restivo, M. Schemmer, A. Cosco, M. Inguscio, A. Trenkwalder, K. Zaremba-Kopczyk, M. Gronowski, M. Tomza, and M. Zaccanti, PRX Quantum **5**, 020358 (2024).

[62] M. Xu, Quantum Phases in Fermi Hubbard Systems With Tunable Frustration, Ph.D. thesis, Harvard University (2024).

[63] Z. Meng, L. Wang, W. Han, F. Liu, K. Wen, C. Gao, P. Wang, C. Chin, and J. Zhang, Nature **615**, 231 (2023).

[64] M. Sbroscia, K. Viebahn, E. Carter, J.-C. Yu, A. Gaunt, and U. Schneider, Physical Review Letters **125**, 200604 (2020).

[65] M. Pasienski, D. McKay, M. White, and B. DeMarco, Nature Physics **6**, 677 (2010).

[66] Y. Guo, R. M. Kroeze, B. P. Marsh, S. Gopalakrishnan, J. Keeling, and B. L. Lev, Nature **599**, 211 (2021).

[67] E. Manousakis, Reviews of Modern Physics **63**, 1 (1991).

[68] R. Jördens, N. Strohmaier, K. Günter, H. Moritz, and T. Esslinger, Nature **455**, 204 (2008).

[69] D. Greif, T. Uehlinger, G. Jotzu, L. Tarruell, and T. Esslinger, Science **340**, 1307 (2013).

[70] T. Chalopin, P. Bojović, S. Wang, T. Franz, A. Sinha, Z. Wang, D. Bourgund, J. Obermeyer, F. Grusdt, A. Bohrdt, L. Pollet, A. Wietek, A. Georges, T. Hilker, and I. Bloch, Probing the magnetic origin of the pseudogap using a Fermi-Hubbard quantum simulator (2024), arXiv:2412.17801 [cond-mat] .

[71] L. H. Kendrick, A. Kale, Y. Gang, A. D. Deters, M. Lebrat, A. W. Young, and M. Greiner, Pseudogap in a Fermi-Hubbard quantum simulator (2025), arXiv:2509.18075 [cond-mat] .

[72] H. Xu, C.-M. Chung, M. Qin, U. Schollwöck, S. R. White, and S. Zhang, Science **384**, eadh7691 (2024).

[73] D. Bourgund, T. Chalopin, P. Bojović, H. Schlömer, S. Wang, T. Franz, S. Hirthe, A. Bohrdt, F. Grusdt, I. Bloch, and T. A. Hilker, Nature **637**, 57 (2025).

[74] S. Baier, M. J. Mark, D. Petter, K. Aikawa, L. Chomaz, Z. Cai, M. Baranov, P. Zoller, and F. Ferlaino, Science **352**, 201 (2016).

[75] L. Su, A. Douglas, M. Szurek, R. Groth, S. F. Ozturk, A. Krahn, A. H. Hébert, G. A. Phelps, S. Ebadi, S. Dickerson, F. Ferlaino, O. Marković, and M. Greiner, Nature **622**, 724 (2023).

[76] A. V. Gorshkov, S. R. Manmana, G. Chen, J. Ye, E. Demler, M. D. Lukin, and A. M. Rey, Physical Review Letters **107**, 115301 (2011).

[77] J. Zirbel, Ultracold Fermionic Feshbach Molecules, Ph.D. thesis, University of Colorado Boulder (2008).

[78] K.-K. Ni, A Quantum Gas of Polar Molecules, Ph.D. thesis, University of Colorado Boulder (2009).

[79] M. de Miranda, Control of Dipolar Collisions in the Quantum Regime, Ph.D. thesis, University of Colorado Boulder (2010).

[80] B. Neyenhuis, Ultracold Polar KRb Molecules in Optical Lattices, Ph.D. thesis, University of Colorado Boulder (2012).

[81] S. Moses, A Quantum Gas of Polar Molecules in an Optical Lattice, Ph.D. thesis, University of Colorado Boulder (2016).

[82] J. Covey, Enhanced Optical and Electric Manipulation of a Quantum Gas of KRb Molecules, Ph.D. thesis, University of Colorado Boulder (2017).

[83] W. Tobias, Degenerate Polar Molecules with Controlled Interactions and Reactivity, Ph.D. thesis, University of Colorado Boulder (2022).

[84] K. Matsuda, Tunable Dipolar Interactions and Collisional Shielding in a Quantum Gas of Polar Molecules, Ph.D. thesis, University of Colorado Boulder (2022).

[85] L. De Marco, G. Valtolina, K. Matsuda, W. G. Tobias, J. P. Covey, and J. Ye, Science **363**, 853 (2019).

[86] W. G. Tobias, K. Matsuda, G. Valtolina, L. De Marco, J.-R. Li, and J. Ye, Physical Review Letters **124**, 033401 (2020).

[87] M. Duda, X.-Y. Chen, A. Schindewolf, R. Bause, J. von Milczewski, R. Schmidt, I. Bloch, and X.-Y. Luo, Nature Physics **19**, 720 (2023).

[88] B. DeMarco, H. Rohner, and D. Jin, Review of Scientific Instruments **70**, 1967 (1999).

[89] M. Meucci, E. Mariotti, P. Bicchi, C. Marinelli, and L. Moi, Europhysics Letters **25**, 639 (1994).

[90] T. Tiecke, Properties of Potassium (2019).

[91] D. A. Steck, Rubidium 87 D line data (2001).

[92] Y. Kiefer, M. Hachmann, and A. Hemmerich, Physical Review A **109**, 023320 (2024).

[93] K. B. Davis, M. O. Mewes, M. R. Andrews, N. J. van Druten, D. S. Durfee, D. M. Kurn, and W. Ketterle, Physical Review Letters **75**, 3969 (1995).

[94] Y. Lu, C. M. Holland, and L. W. Cheuk, Physical Review Letters **128**, 213201 (2022).

[95] J. J. Zirbel, K.-K. Ni, S. Ospelkaus, T. L. Nicholson, M. L. Olsen, P. S. Julienne, C. E. Wieman, J. Ye, and D. S. Jin, Physical Review A **78**, 013416 (2008).

[96] J. J. Zirbel, K.-K. Ni, S. Ospelkaus, J. P. D'Incao, C. E. Wieman, J. Ye, and D. S. Jin, Physical Review Letters **100**, 143201 (2008).

[97] S. Ospelkaus, K.-K. Ni, G. Quéméner, B. Neyenhuis, D. Wang, M. H. G. de Miranda, J. L. Bohn, J. Ye, and D. S. Jin, Physical Review Letters **104**, 030402 (2010).

[98] J. P. Covey, L. D. Marco, Ó. L. Acevedo, A. M. Rey, and J. Ye, New Journal of Physics **20**, 043031 (2018).

[99] G. Valtolina, K. Matsuda, W. G. Tobias, J.-R. Li, L. De Marco, and J. Ye, Nature **588**, 239 (2020).

[100] A. Chotia, B. Neyenhuis, S. A. Moses, B. Yan, J. P. Covey, M. Foss-Feig, A. M. Rey, D. S. Jin, and J. Ye, Physical Review Letters **108**, 080405 (2012).

[101] B. Yan, S. A. Moses, B. Gadway, J. P. Covey, K. R. Hazzard, A. M. Rey, D. S. Jin, and J. Ye, Nature **501**, 521 (2013).

[102] K. R. A. Hazzard, B. Gadway, M. Foss-Feig, B. Yan, S. A. Moses, J. P. Covey, N. Y. Yao, M. D. Lukin, J. Ye, D. S. Jin, and A. M. Rey, Physical Review Letters **113**, 195302 (2014).

[103] S. A. Moses, J. P. Covey, M. T. Miecnikowski, B. Yan, B. Gadway, J. Ye, and D. S. Jin, Science **350**, 659 (2015).

[104] J. P. Covey, S. A. Moses, M. Gärttner, A. Safavi-Naini, M. T. Miecnikowski, Z. Fu, J. Schachenmayer, P. S. Julienne, A. M. Rey, D. S. Jin, and J. Ye, Nature Communications **7**, 11279 (2016).

[105] W. G. Tobias, K. Matsuda, J.-R. Li, C. Miller, A. N. Carroll, T. Bilitewski, A. M. Rey, and J. Ye, Science **375**, 1299 (2022).

[106] A. Vianello, Amv213/ComponentLibrary: Improved Inkscape vector graphics library for illustrations of optics experiments (2021).

[107] N. D. Oppong, Towards a Degenerate Fermi Gas of Strontium-87 in a 3D Optical Lattice, Master's thesis, ETH Zurich/ University of Colorado Boulder (2015).

[108] B. Neyenhuis, B. Yan, S. A. Moses, J. P. Covey, A. Chotia, A. Petrov, S. Kotochigova, J. Ye, and D. S. Jin, Physical Review Letters **109**, 230403 (2012).

[109] K. Bergmann, H. Theuer, and B. W. Shore, Reviews of Modern Physics **70**, 1003 (1998).

[110] N. V. Vitanov, A. A. Rangelov, B. W. Shore, and K. Bergmann, Reviews of Modern Physics **89**, 015006 (2017).

[111] E. D. Black, American Journal of Physics **69**, 79 (2001).

[112] L. P. Yatsenko, B. W. Shore, and K. Bergmann, Physical Review A **89**, 013831 (2014).

[113] B. P. Maddox, J. M. Mortlock, T. R. Hepworth, A. P. Raghuram, P. D. Gregory, A. Guttridge, and S. L. Cornish, Physical Review Letters **133**, 253202 (2024).

[114] L. Li, W. Huie, N. Chen, B. DeMarco, and J. P. Covey, Physical Review Applied **18**, 064005 (2022).

[115] Y.-X. Chao, Z.-X. Hua, X.-H. Liang, Z.-P. Yue, L. You, and M. K. Tey, Optica **11**, 945 (2024).

[116] Y.-X. Chao, Z.-X. Hua, X.-H. Liang, Z.-P. Yue, C. Jia, L. You, and M. K. Tey, Physical Review Applied **23**, L011005 (2025).

[117] J.-R. Li, K. Matsuda, C. Miller, A. N. Carroll, W. G. Tobias, J. S. Higgins, and J. Ye, Nature **614**, 70 (2023).

[118] A. Young, Programmable Arrays of Alkaline Earth Atoms: Qubits, Clocks, and the Bose-Hubbard Model, Ph.D. thesis, University of Colorado Boulder (2023).

[119] J. Choi, H. Zhou, H. S. Knowles, R. Landig, S. Choi, and M. D. Lukin, Physical Review X **10**, 031002 (2020).

[120] A. M. Souza, G. A. Álvarez, and D. Suter, Physical Review Letters **106**, 240501 (2011).

[121] A. N. Carroll, H. Hirzler, C. Miller, D. Wellnitz, S. R. Muleady, J. Lin, K. P. Zamarski, R. R. W. Wang, J. L. Bohn, A. M. Rey, and J. Ye, Science **388**, 381 (2025).

[122] E. Knill, D. Leibfried, R. Reichle, J. Britton, R. B. Blakestad, J. D. Jost, C. Langer, R. Ozeri, S. Seidelin, and D. J. Wineland, Physical Review A **77**, 012307 (2008).

[123] C. Miller, A. N. Carroll, J. Lin, H. Hirzler, H. Gao, H. Zhou, M. D. Lukin, and J. Ye, Nature **633**, 332 (2024).

[124] H. Zhou, H. Gao, N. T. Leitao, O. Makarova, I. Cong, A. M. Douglas, L. S. Martin, and M. D. Lukin, Physical Review X **14**, 031017 (2024).

[125] B. Sundar, B. Gadway, and K. R. A. Hazzard, Scientific Reports **8**, 3422 (2018).

[126] P. B. Wigley, P. J. Everitt, A. van den Hengel, J. W. Bastian, M. A. Sooriyabandara, G. D. McDonald, K. S. Hardman, C. D. Quinlivan, P. Manju, C. C. N. Kuhn, I. R. Petersen, A. N. Luiten, J. J. Hope, N. P. Robins, and M. R. Hush, Scientific Reports **6**, 25890 (2016).

[127] K. Matsuda, Kylematsuda/BialkaliSpectrum.jl (2023).

[128] R. N. Zare, Angular Momentum: Understanding Spatial Aspects in Chemistry and Physics (Wiley, 1988).

[129] C. J. Foot, Atomic Physics (Oxford University Press, Oxford ; New York, 2005).

[130] L. M. K. Vandersypen and I. L. Chuang, Reviews of Modern Physics **76**, 1037 (2005).

[131] E. L. Hahn, Physical Review **80**, 580 (1950).

[132] M. Bishof, X. Zhang, M. J. Martin, and J. Ye, Physical Review Letters **111**, 093604 (2013).

[133] M. J. Martin, Quantum Metrology and Many-Body Physics: Pushing the Frontier of the Optical Lattice Clock, Ph.D. thesis, University of Colorado Boulder (2013).

[134] T. Gullion, D. B. Baker, and M. S. Conradi, Journal of Magnetic Resonance (1969) **89**, 479 (1990).

[135] Y. Wu, S. Kolkowitz, S. Puri, and J. D. Thompson, Nature Communications **13**, 4657 (2022).

[136] M. A. Baranov, A. Micheli, S. Ronen, and P. Zoller, Physical Review A **83**, 043602 (2011).

[137] T. Bilitewski, G. A. Domínguez-Castro, D. Wellnitz, A. M. Rey, and L. Santos, Physical Review A **108**, 013313 (2023).

[138] T. Bilitewski and A. M. Rey, Physical Review Letters **131**, 053001 (2023).

[139] R. Grimm, M. Weidemüller, and Y. B. Ovchinnikov, in Advances In Atomic, Molecular, and Optical Physics, Vol. 42, edited by B. Bederson and H. Walther (Academic Press, 2000) pp. 95–170.

[140] M. Greiner, Ultracold quantum gases in three-dimensional optical lattice potentials, Ph.D. thesis, Ludwig-Maximilians-Universität München (2003).

[141] W. Kohn, Physical Review **115**, 809 (1959).

[142] W. Zwerger, Journal of Optics B: Quantum and Semiclassical Optics **5**, S9 (2003).

[143] R. Jáuregui, N. Poli, G. Roati, and G. Modugno, Physical Review A **64**, 033403 (2001).

[144] T. Rosenband, D. D. Grimes, and K.-K. Ni, Optics Express **26**, 19821 (2018).

[145] A. J. Park, L. R. B. Picard, G. E. Patenotte, J. T. Zhang, T. Rosenband, and K.-K. Ni, Physical Review Letters **131**, 183401 (2023).

[146] J. A. Blackmore, R. Sawant, P. D. Gregory, S. L. Bromley, J. Aldegunde, J. M. Hutson, and S. L. Cornish, Physical Review A **102**, 053316 (2020).

[147] L. Christakis, J. S. Rosenberg, R. Raj, S. Chi, A. Morningstar, D. A. Huse, Z. Z. Yan, and W. S. Bakr, Nature **614**, 64 (2023).

[148] S. Kotochigova and D. DeMille, Physical Review A **82**, 063421 (2010).

[149] F. Seeßelberg, X.-Y. Luo, M. Li, R. Bause, S. Kotochigova, I. Bloch, and C. Gohle, Physical Review Letters **121**, 253401 (2018).

[150] S. Burchesky, L. Anderegg, Y. Bao, S. S. Yu, E. Chae, W. Ketterle, K.-K. Ni, and J. M. Doyle, Physical Review Letters **127**, 123202 (2021).

[151] Q. Guan, S. L. Cornish, and S. Kotochigova, Physical Review A **103**, 043311 (2021).

[152] R. Vexiau, D. Borsalino, M. Lepers, A. Orbán, M. Aymar, O. Dulieu, and N. Bouloufa-Maafa, International Reviews in Physical Chemistry **36**, 709 (2017).

[153] R. Bause, M. Li, A. Schindewolf, X.-Y. Chen, M. Duda, S. Kotochigova, I. Bloch, and X.-Y. Luo, Physical Review Letters **125**, 023201 (2020).

[154] P. D. Gregory, L. M. Fernley, A. L. Tao, S. L. Bromley, J. Stepp, Z. Zhang, S. Kotochigova, K. R. A. Hazzard, and S. L. Cornish, Nature Physics **20**, 415 (2024).

[155] D. K. Ruttley, T. R. Hepworth, A. Guttridge, and S. L. Cornish, Nature **637**, 827 (2025).

[156] T. R. Hepworth, D. K. Ruttley, F. von Gierke, P. D. Gregory, A. Guttridge, and S. L. Cornish, Nature Communications **16**, 7131 (2025).

[157] J. Kobayashi, K. Aikawa, K. Oasa, and S. Inouye, Physical Review A **89**, 021401 (2014).

[158] P. N. Jepsen, J. Amato-Grill, I. Dimitrova, W. W. Ho, E. Demler, and W. Ketterle, Nature **588**, 403 (2020).

[159] M. A. Norcia, R. J. Lewis-Swan, J. R. K. Cline, B. Zhu, A. M. Rey, and J. K. Thompson, Science **361**, 259 (2018).

[160] K. Binder and A. P. Young, Reviews of Modern Physics **58**, 801 (1986).

[161] R. M. Kroeze, B. P. Marsh, D. Atri Schuller, H. S. Hunt, A. N. Bourzutschky, M. Winer, S. Gopalakrishnan, J. Keeling, and B. L. Lev, Science **389**, 1122 (2025).

[162] L. Chomaz, I. Ferrier-Barbut, F. Ferlaino, B. Laburthe-Tolra, B. L. Lev, and T. Pfau, Reports on Progress in Physics **86**, 026401 (2022).

[163] R. Schirhagl, K. Chang, M. Loretz, and C. L. Degen, Annual Review of Physical Chemistry **65**, 83 (2014).

[164] T. E. Lee, Physical Review A **94**, 040701 (2016).

[165] T. Bilitewski, L. De Marco, J.-R. Li, K. Matsuda, W. G. Tobias, G. Valtolina, J. Ye, and A. M. Rey, Physical Review Letters **126**, 113401 (2021).

[166] Y. Sagi, I. Almog, and N. Davidson, Physical Review Letters **105**, 093001 (2010).

[167] R. Stricker, M. Meth, L. Postler, C. Edmunds, C. Ferrie, R. Blatt, P. Schindler, T. Monz, R. Kueng, and M. Ringbauer, PRX Quantum **3**, 040310 (2022).

[168] M. J. Martin, M. Bishof, M. D. Swallows, X. Zhang, C. Benko, J. von-Stecher, A. V. Gorshkov, A. M. Rey, and J. Ye, Science **341**, 632 (2013).

[169] M. Kitagawa and M. Ueda, Physical Review A **47**, 5138 (1993).

[170] K. R. A. Hazzard, S. R. Manmana, M. Foss-Feig, and A. M. Rey, Physical Review Letters **110**, 075301 (2013).

[171] M. A. Baranov, M. S. Mar'enko, Val. S. Rychkov, and G. V. Shlyapnikov, Physical Review A **66**, 013606 (2002).

[172] L. D. Carr, D. DeMille, R. V. Krems, and J. Ye, New Journal of Physics **11**, 055049 (2009).

[173] M. A. Baranov, M. Dalmonte, G. Pupillo, and P. Zoller, Chemical Reviews **112**, 5012 (2012).

[174] V. Veljić, A. R. P. Lima, L. Chomaz, S. Baier, M. J. Mark, F. Ferlaino, A. Pelster, and A. Balaž, New Journal of Physics **20**, 093016 (2018).

[175] J. Eisert, M. Friesdorf, and C. Gogolin, Nature Physics **11**, 124 (2015).

[176] A. Goussev, R. A. Jalabert, H. M. Pastawski, and D. Wisniacki, Scholarpedia **7**, 11687 (2012), arXiv:1206.6348 [nlin] .

[177] J. Braumüller, A. H. Karamlou, Y. Yanay, B. Kannan, D. Kim, M. Kjaergaard, A. Melville, B. M. Niedzielski, Y. Sung, A. Vepsäläinen, R. Winik, J. L. Yoder, T. P. Orlando, S. Gustavsson, C. Tahan, and W. D. Oliver, Nature Physics **18**, 172 (2022).

[178] E. Davis, G. Bentsen, and M. Schleier-Smith, Physical Review Letters **116**, 053601 (2016).

[179] S. Colombo, E. Pedrozo-Peñafiel, A. F. Adiyatullin, Z. Li, E. Mendez, C. Shu, and V. Vuletić, Nature Physics **18**, 925 (2022).

[180] H. Gao, L. S. Martin, L. B. Hughes, N. T. Leitao, P. Put, H. Zhou, N. U. Koyluoglu, S. A. Meynell, A. C. B. Jayich, H. Park, and M. D. Lukin, Nature **646**, 68 (2025).

[181] S. Geier, A. Braemer, E. Braun, M. Müllenbach, T. Franz, M. Gärttner, G. Zürn, and M. Weidemüller, Physical Review Research **6**, 033197 (2024).

[182] S. Geier, N. Thaicharoen, C. Hainaut, T. Franz, A. Salzinger, A. Tebben, D. Grimshandl, G. Zürn, and M. Weidemüller, Science **374**, 1149 (2021).

[183] L. S. Martin, H. Zhou, N. T. Leitao, N. Maskara, O. Makarova, H. Gao, Q.-Z. Zhu, M. Park, M. Tyler, H. Park, S. Choi, and M. D. Lukin, Physical Review Letters **130**, 210403 (2023).

[184] U. Haeberlen and J. S. Waugh, Physical Review **175**, 453 (1968).

[185] M. Tyler, H. Zhou, L. S. Martin, N. Leitao, and M. D. Lukin, Physical Review A **108**, 062602 (2023).

[186] V. Giovannetti, S. Lloyd, and L. Maccone, Science **306**, 1330 (2004).

[187] C. Luo, H. Zhang, A. Chu, C. Maruko, A. M. Rey, and J. K. Thompson, Nature Physics , 1 (2025).

[188] Y. C. Liu, Z. F. Xu, G. R. Jin, and L. You, Physical Review Letters **107**, 013601 (2011).

[189] J. Hald, J. L. Sørensen, C. Schori, and E. S. Polzik, Physical Review Letters **83**, 1319 (1999).

[190] M. H. Muñoz-Arias, I. H. Deutsch, and P. M. Poggi, PRX Quantum **4**, 020314 (2023).

[191] N. U. Koyluoglu, S. V. Rajagopal, G. L. Moreau, J. A. Hines, O. Marković, and M. Schleier-Smith, Squeezing Towards the Heisenberg Limit with Locally Interacting Spins (2025), arXiv:2506.16973 [quant-ph] .

[192] J. M. Mortlock, A. P. Raghuram, B. P. Maddox, P. D. Gregory, and S. L. Cornish, Multi-state detection and spatial addressing in a microscope for ultracold molecules (2025), arXiv:2506.12329 [cond-mat] .

[193] A. Signoles, T. Franz, R. Ferracini Alves, M. Gärttner, S. Whitlock, G. Zürn, and M. Weidemüller, Physical Review X **11**, 011011 (2021).

[194] A. Douglas, V. Kaxiras, L. Su, M. Szurek, V. Singh, O. Marković, and M. Greiner, Phys. Rev. X 10.1103/shj7-9kb3 (2025).

[195] G. Bornet, G. Emperauger, C. Chen, B. Ye, M. Block, M. Bintz, J. A. Boyd, D. Barredo, T. Comparin, F. Mezzacapo, T. Roscilde, T. Lahaye, N. Y. Yao, and A. Browaeys, Nature **621**, 728 (2023).

[196] M. A. Perlin, C. Qu, and A. M. Rey, Physical Review Letters **125**, 223401 (2020).

[197] M. Block, B. Ye, B. Roberts, S. Chern, W. Wu, Z. Wang, L. Pollet, E. J. Davis, B. I. Halperin, and N. Y. Yao, Nature Physics **20**, 1575 (2024).

[198] M. P. Kwasigroch and N. R. Cooper, Physical Review A **90**, 021605 (2014).

[199] M. P. Kwasigroch and N. R. Cooper, Physical Review A **96**, 053610 (2017).

[200] C. M. Holland, Y. Lu, and L. W. Cheuk, Science **382**, 1143 (2023).

[201] Y. Bao, S. S. Yu, L. Anderegg, E. Chae, W. Ketterle, K.-K. Ni, and J. M. Doyle, Science **382**, 1138 (2023).

[202] L. R. B. Picard, A. J. Park, G. E. Patenotte, S. Gebretsadkan, D. Wellnitz, A. M. Rey, and K.-K. Ni, Nature **637**, 821 (2025).

[203] R. R. W. Wang and J. L. Bohn, Theory of itinerant collisional spin dynamics in nondegenerate molecular gases (2025), arXiv:2505.21896 [cond-mat] .

[204] C. Ticknor, Physical Review A **80**, 052702 (2009).

[205] G. Quéméner and J. L. Bohn, Physical Review A **83**, 012705 (2011).

[206] G. A. Bird, The Physics of Fluids **13**, 2676 (1970).

[207] K.-K. Ni, S. Ospelkaus, D. Wang, G. Quéméner, B. Neyenhuis, M. H. G. de Miranda, J. L. Bohn, J. Ye, and D. S. Jin, Nature **464**, 1324 (2010).

[208] B. DeMarco, S. B. Papp, and D. S. Jin, Physical Review Letters **86**, 5409 (2001).

[209] D. Wellnitz, M. Mamaev, T. Bilitewski, and A. M. Rey, Physical Review Research **6**, L012025 (2024).

[210] C. Gross and I. Bloch, Science **357**, 995 (2017).

[211] A. V. Gorshkov, S. R. Manmana, G. Chen, E. Demler, M. D. Lukin, and A. M. Rey, Physical Review A **84**, 033619 (2011).

[212] W.-M. Huang, C.-Y. Lai, C. Shi, and S.-W. Tsai, Physical Review B **88**, 054504 (2013).

[213] M. L. Wall, Carr, and L. D, New Journal of Physics **15**, 123005 (2013).

[214] H. Zhou, L. S. Martin, M. Tyler, O. Makarova, N. Leitao, H. Park, and M. D. Lukin, Physical Review Letters **131**, 220803 (2023).

[215] K. Hueck, N. Luick, L. Sobirey, J. Siegl, T. Lompe, and H. Moritz, Physical Review Letters **120**, 060402 (2018).

[216] Y.-X. Wang, H.-J. Shao, Y.-S. Zhu, D.-Z. Zhu, H.-N. Sun, S.-Y. Chen, X.-C. Yao, Y.-A. Chen, and J.-W. Pan, Physical Review Letters **134**, 043403 (2025).

[217] C. Zu, F. Machado, B. Ye, S. Choi, B. Kobrin, T. Mittiga, S. Hsieh, P. Bhattacharyya, M. Markham, D. Twitchen, A. Jarmola, D. Budker, C. R. Laumann, J. E. Moore, and N. Y. Yao, Nature **597**, 45 (2021).

[218] P. T. Brown, D. Mitra, E. Guardado-Sanchez, R. Nourafkan, A. Reymbaut, C.-D. Hébert, S. Bergeron, A.-M. S. Tremblay, J. Kokalj, D. A. Huse, P. Schauß, and W. S. Bakr, Science **363**, 379 (2019).

[219] M. A. Nichols, L. W. Cheuk, M. Okan, T. R. Hartke, E. Mendez, T. Senthil, E. Khatami, H. Zhang, and M. W. Zwierlein, Science **363**, 383 (2019).

[220] C. S. Chiu, G. Ji, A. Mazurenko, D. Greif, and M. Greiner, Physical Review Letters **120**, 243201 (2018).

[221] N. Bigagli, W. Yuan, S. Zhang, B. Bulatovic, T. Karman, I. Stevenson, and S. Will, Nature **631**, 289 (2024).

[222] Z. Shi, Z. Huang, F. Deng, W.-J. Jin, S. Yi, T. Shi, and D. Wang, Bose-Einstein condensate of ultracold sodium-rubidium molecules with tunable dipolar interactions (2025), arXiv:2508.20518 [cond-mat] .

[223] N. R. Cooper and G. V. Shlyapnikov, Physical Review Letters **103**, 155302 (2009).

[224] J. Levinsen, N. R. Cooper, and G. V. Shlyapnikov, Physical Review A **84**, 013603 (2011).

[225] A. Pikovski, M. Klawunn, G. V. Shlyapnikov, and L. Santos, Physical Review Letters **105**, 215302 (2010).

[226] F. Deng, X.-Y. Chen, X.-Y. Luo, W. Zhang, S. Yi, and T. Shi, Physical Review Letters **130**, 183001 (2023).

[227] K. Aikawa, S. Baier, A. Frisch, M. Mark, C. Ravensbergen, and F. Ferlaino, Science **345**, 1484 (2014).

[228] M. Babadi and E. Demler, Physical Review A **86**, 063638 (2012).

[229] J.-R. Li, W. G. Tobias, K. Matsuda, C. Miller, G. Valtolina, L. De Marco, R. R. W. Wang, L. Lassablière, G. Quéméner, J. L. Bohn, and J. Ye, Nature Physics **17**, 1144 (2021).

[230] P. B. Blakie and A. Bezett, Physical Review A **71**, 033616 (2005).

[231] L. Reichsöllner, A. Schindewolf, T. Takekoshi, R. Grimm, and H.-C. Nägerl, Physical Review Letters **118**, 073201 (2017).

[232] L. Pollet, C. Kollath, U. Schollwöck, and M. Troyer, Physical Review A **77**, 023608 (2008).

[233] A. Safavi-Naini, M. L. Wall, and A. M. Rey, Physical Review A **92**, 063416 (2015).

[234] U. Schneider, L. Hackermüller, S. Will, Th. Best, I. Bloch, T. A. Costi, R. W. Helmes, D. Rasch, and A. Rosch, Science **322**, 1520 (2008).

[235] D. Greif, M. F. Parsons, A. Mazurenko, C. S. Chiu, S. Blatt, F. Huber, G. Ji, and M. Greiner, Science **351**, 953 (2016).

[236] S. L. Campbell, R. B. Hutson, G. E. Marti, A. Goban, N. Darkwah Oppong, R. L. McNally, L. Sonderhouse, J. M. Robinson, W. Zhang, B. J. Bloom, and J. Ye, Science **358**, 90 (2017).

[237] W. R. Milner, L. Yan, R. B. Hutson, C. Sanner, and J. Ye, Physical Review A **107**, 063313 (2023).

[238] M. Greiner, O. Mandel, T. Esslinger, T. W. Hänsch, and I. Bloch, Nature **415**, 39 (2002).

[239] W. S. Bakr, Microscopic Studies of Quantum Phase Transitions in Optical Lattices, Ph.D. thesis, Harvard University (2011).

[240] J. K. Blitzstein and Jessica Hwang, Introduction to Probability, 2nd ed. (Chapman & Hall/CRC Press, 2019).

[241] W. S. Bakr, A. Peng, M. E. Tai, R. Ma, J. Simon, J. I. Gillen, S. Fölling, L. Pollet, and M. Greiner, Science **329**, 547 (2010).

[242] E. Hodby, S. T. Thompson, C. A. Regal, M. Greiner, A. C. Wilson, D. S. Jin, E. A. Cornell, and C. E. Wieman, Physical Review Letters **94**, 120402 (2005).

[243] J. E. Williams, N. Nygaard, and C. W. Clark, New Journal of Physics **8**, 150 (2006).

[244] S. Watabe and T. Nikuni, Physical Review A **77**, 013616 (2008).

[245] T. D. Cumby, R. A. Shewmon, M.-G. Hu, J. D. Perreault, and D. S. Jin, Physical Review A **87**, 012703 (2013).

[246] K. Matsuda, L. De Marco, J.-R. Li, W. G. Tobias, G. Valtolina, G. Quéméner, and J. Ye, Science **370**, 1324 (2020).

[247] T. Karman and J. M. Hutson, Physical Review Letters **121**, 163401 (2018).

[248] F. Ç. Top, Y. Margalit, and W. Ketterle, Physical Review A **104**, 043311 (2021).

[249] D. A. Butts and D. S. Rokhsar, Physical Review A **55**, 4346 (1997).

[250] D. S. Petrov, M. Holzmann, and G. V. Shlyapnikov, Physical Review Letters **84**, 2551 (2000).

[251] F. Ferlaino, C. D'Errico, G. Roati, M. Zaccanti, M. Inguscio, G. Modugno, and A. Simoni, Physical Review A **73**, 040702 (2006).

[252] K. H. Morgener, Microscopy of 2D Fermi Gases, Ph.D. thesis, Universität Hamburg (2014).

[253] R. R. W. Wang, S. Biswas, S. Eppelt, F. Deng, X.-Y. Luo, and J. L. Bohn, Physical Review A **110**, 043309 (2024).

[254] M.-G. Hu, Y. Liu, D. D. Grimes, Y.-W. Lin, A. H. Gheorghe, R. Vexiau, N. Bouloufa-Maafa, O. Dulieu, T. Rosenband, and K.-K. Ni, Science **366**, 1111 (2019).

[255] R. Bause, A. Christianen, A. Schindewolf, I. Bloch, and X.-Y. Luo, The Journal of Physical Chemistry A **127**, 729 (2023).

[256] G. Quéméner and J. L. Bohn, Physical Review A **81**, 022702 (2010).

[257] L. Anderegg, S. Burchesky, Y. Bao, S. S. Yu, T. Karman, E. Chae, K.-K. Ni, W. Ketterle, and J. M. Doyle, Science **373**, 779 (2021).

[258] J. Lin, G. Chen, M. Jin, Z. Shi, F. Deng, W. Zhang, G. Quéméner, T. Shi, S. Yi, and D. Wang, Physical Review X **13**, 031032 (2023).

[259] N. Bigagli, C. Warner, W. Yuan, S. Zhang, I. Stevenson, T. Karman, and S. Will, Nature Physics **19**, 1579 (2023).

[260] A. Schindewolf, R. Bause, X.-Y. Chen, M. Duda, T. Karman, I. Bloch, and X.-Y. Luo, Nature **607**, 677 (2022).

[261] T. Xie, M. Lepers, R. Vexiau, A. Orbán, O. Dulieu, and N. Bouloufa-Maafa, Physical Review Letters **125**, 153202 (2020).

[262] C. Karam, R. Vexiau, N. Bouloufa-Maafa, O. Dulieu, M. Lepers, M. M. z. A. Borgloh, S. Ospelkaus, and L. Karpa, Physical Review Research **5**, 033074 (2023).

[263] A. Micheli, Z. Idziaszek, G. Pupillo, M. A. Baranov, P. Zoller, and P. S. Julienne, Physical Review Letters **105**, 073202 (2010).

[264] B. Zhu, G. Quéméner, A. M. Rey, and M. J. Holland, Physical Review A **88**, 063405 (2013).

[265] M. H. G. de Miranda, A. Chotia, B. Neyenhuis, D. Wang, G. Quéméner, S. Ospelkaus, J. L. Bohn, J. Ye, and D. S. Jin, Nature Physics **7**, 502 (2011).

[266] Z.-Y. Ma, A. M. Thomas, C. J. Foot, and S. L. Cornish, Journal of Physics B: Atomic, Molecular and Optical Physics **36**, 3533 (2003).

[267] S. Chapman and T. G. Cowling, The Mathematical Theory of Non-uniform Gases (Cambridge University Press, 1990).

[268] J. L. Bohn, M. Cavagnero, and C. Ticknor, New Journal of Physics **11**, 055039 (2009).

[269] J. L. Bohn and D. S. Jin, Physical Review A **89**, 022702 (2014).

[270] E. Timmermans, Physical Review Letters **87**, 240403 (2001).

[271] S. Giorgini, L. P. Pitaevskii, and S. Stringari, Reviews of Modern Physics **80**, 1215 (2008).

[272] A. Hebert, A Dipolar Erbium Quantum Gas Microscope, Ph.D. thesis, Harvard University, Cambridge, MA (2021).

[273] R. Saint-Jalm, Exploring Two-Dimensional Physics with Bose Gases in Box Potentials, Ph.D. thesis, Université Paris Sciences et Lettres (2019).

[274] B. Guenter, Brianguenter/OpticSim.jl (2021).

[275] L. Corman, The Two-Dimensional Bose Gas in Box Potentials, Ph.D. thesis, Université Paris Sciences et Lettres (2016).

[276] L. Asteria, H. P. Zahn, M. N. Kosch, K. Sengstock, and C. Weitenberg, Nature **599**, 571 (2021).

[277] P. L. Gould, G. A. Ruff, and D. E. Pritchard, Physical Review Letters **56**, 827 (1986).

[278] M. Duda,
Production of ground-state $^{23}Na^{40}K$ molecules in the quantum-degenerate regime, Ph.D. thesis, Ludwig-Maximilians-Universität München (2022).

[279] N. Navon, R. P. Smith, and Z. Hadzibabic, Nature Physics **17**, 1334 (2021).

[280] S. Eppelt, S. Biswas, X.-Y. Chen, A. Schindewolf, T. Hilker, I. Bloch, and X.-Y. Luo, in APS Division of Atomic, Molecular and Optical Physics Meeting Abstracts (2024).

[281] R. Roy, A. Green, R. Bowler, and S. Gupta, Physical Review A **93**, 043403 (2016).

[282] J. F. Wienand, Quantum gas microscopy of fluctuating hydrodynamics in optical ladders, Ph.D. thesis, Ludwig-Maximilians-Universität München (2024).

[283] A. Mazurenko,
Probing Long Range Antiferromagnetism and Dynamics in the Fermi-Hubbard Model, Ph.D. thesis, Harvard University, Cambridge, MA (2017).

[284] S. P. Hubele,
Potential Shaping Using a DMD and High-Resolution Imaging of Cesium Atoms in Optical Lattices, Master's thesis, Ludwig-Maximilians-Universität München (2022).

[285] R. Roy, A. Green, R. Bowler, and S. Gupta, Physical Review Letters **118**, 055301 (2017).

[286] B. P. Marsh,
Quantum-Optical Neural Networks and Spin Glasses Made of Ultracold Atoms and Photons, Ph.D. thesis, Stanford University (2024).

[287] D. Trypogeorgos, T. Harte, A. Bonnin, and C. Foot, Optics Express **21**, 24837 (2013).

[288] J. Ma, X. Wang, C. P. Sun, and F. Nori, Physics Reports **509**, 89 (2011).

[289] I. D. Leroux, M. H. Schleier-Smith, and V. Vuletić, Physical Review Letters **104**, 073602 (2010).

[290] C. Gross, Journal of Physics B: Atomic, Molecular and Optical Physics **45**, 103001 (2012).

[291] W. J. Eckner, N. Darkwah Oppong, A. Cao, A. W. Young, W. R. Milner, J. M. Robinson, J. Ye, and A. M. Kaufman, Nature **621**, 734 (2023).

[292] J. A. Hines, S. V. Rajagopal, G. L. Moreau, M. D. Wahrman, N. A. Lewis, O. Marković, and M. Schleier-Smith, Physical Review Letters **131**, 063401 (2023).

[293] W. Wu, E. J. Davis, L. B. Hughes, B. Ye, Z. Wang, D. Kufel, T. Ono, S. A. Meynell, M. Block, C. Liu, H. Yang, A. C. Bleszynski Jayich, and N. Y. Yao, Nature **646**, 74 (2025).

[294] Y. K. Lee, M. Block, H. Lin, V. Fedoseev, P. J. D. Crowley, N. Y. Yao, and W. Ketterle, Physical Review Letters **135**, 023402 (2025).

[295] J. Franke, S. R. Muleady, R. Kaubruegger, F. Kranzl, R. Blatt, A. M. Rey, M. K. Joshi, and C. F. Roos, Nature **621**, 740 (2023).

[296] X. Wang, A. Miranowicz, Y.-x. Liu, C. P. Sun, and F. Nori, Physical Review A **81**, 022106 (2010).

[297] C.-G. Ji, Y.-C. Liu, and G.-R. Jin, Quantum Info. Comput. **13**, 266 (2013).

[298] M. Pappa, P. C. Condylis, G. O. Konstantinidis, V. Bolpasi, A. Lazoudis, O. Morizot, D. Sahagun, M. Baker, and W. von Klitzing, New Journal of Physics **13**, 115012 (2011).

[299] C. Groß,
Spin Squeezing and Non-Linear Atom Interferometry with Bose-Einstein Condensates,
Ph.D. thesis, Universität Heidelberg, Heidelberg, Germany (2010).

[300] C. Sanner, E. Su, A. Keshet, R. Gommers, Y.-i. Shin, W. Huang, and W. Ketterle, APS (2010).

[301] K. Hueck, N. Luick, L. Sobirey, J. Siegl, T. Lompe, H. Moritz, L. W. Clark, and C. Chin, Optics Express **25**, 8670 (2017).

[302] G. Ness, A. Vainbaum, C. Shkedrov, Y. Florshaim, and Y. Sagi, Physical Review Applied **14**, 014011 (2020).

[303] B. Song, C. He, Z. Ren, E. Zhao, J. Lee, and G.-B. Jo, Physical Review Applied **14**, 034006 (2020).

[304] J. M. Robinson, M. Miklos, Y. M. Tso, C. J. Kennedy, T. Bothwell, D. Kedar, J. K. Thompson, and J. Ye, Nature Physics **20**, 208 (2024).

[305] X.-Y. Chen, A. Schindewolf, S. Eppelt, R. Bause, M. Duda, S. Biswas, T. Karman, T. Hilker, I. Bloch, and X.-Y. Luo, Nature **614**, 59 (2023).

[306] X.-Y. Chen, S. Biswas, S. Eppelt, A. Schindewolf, F. Deng, T. Shi, S. Yi, T. A. Hilker, I. Bloch, and X.-Y. Luo, Nature **626**, 283 (2024).

[307] S. Biswas, S. Eppelt, W. Tian, C. Frank, I. Bloch, and X.-Y. Luo, in APS Division of Atomic, Molecular and Optical Physics Meeting Abstracts (2025).

[308] W. Yuan, S. Zhang, N. Bigagli, H. Kwak, C. Warner, T. Karman, I. Stevenson, and S. Will, Extreme Loss Suppression and Wide Tunability of Dipolar Interactions in an Ultracold Molecular Gas (2025), arXiv:2505.08773 [cond-mat] .

[309] S. Zhang, W. Yuan, N. Bigagli, H. Kwak, T. Karman, I. Stevenson, and S. Will, Observation of Self-Bound Droplets of Ultracold Dipolar Molecules (2025), arXiv:2507.15208 [cond-mat] .

[310] L. W. Cheuk, in APS Division of Atomic, Molecular and Optical Physics Meeting Abstracts (2025).

[311] D. K. Ruttley, A. Guttridge, T. R. Hepworth, and S. L. Cornish, PRX Quantum **5**, 020333 (2024).

[312] L. R. B. Picard, G. E. Patenotte, A. J. Park, S. F. Gebretsadkan, and K.-K. Ni, PRX Quantum **5**, 020344 (2024).

[313] T. Karman, N. Bigagli, W. Yuan, S. Zhang, I. Stevenson, and S. Will, PRX Quantum **6**, 020358 (2025).

[314] M. Vayninger, A. Xiang, N. D. Bhanushali, X. Chen, M. Verma, S. Yang, R. T. Kapur, D. DeMille, and Z. Z. Yan, A magneto-optical trap of silver and potassium atoms (2025), arXiv:2507.11434 [physics]